nature chemical engineering

Article

https://doi.org/10.1038/s44286-024-00153-y

In situ techniques for aqueous quinone-mediated electrochemical carbon capture and release

Received: 4 April 2024

Accepted: 1 November 2024

Published online: 16 December 2024

Check for updates

Kiana Amini[1,3], Thomas Cochard[1], Yan Jing[2,4], Jordan D. Sosa[1], Dawei Xi[1], Maia Alberts[1], Michael S. Emanuel[1], Emily F. Kerr[2,5], Roy G. Gordon[2] & Michael J. Aziz[1]

Here we elucidate the intricate interplay between the nucleophilicity swing and pH swing mechanisms in aqueous quinone-mediated carbon capture systems, showcasing the critical role of understanding this interplay in the material discovery cycle. This insight prompts the development of two in situ techniques. The first technique employs in situ reference electrodes and capitalizes on discernible voltage signature differences between quinones and quinone–CO_2 adducts, allowing for the quantification of the isolated contributions of the two mechanisms. The second method is developed based on our finding that the adduct form of the quinone exhibits a fluorescence emission from an incident light at wavelengths distinct from the fluorescence of the reduced form. Thus, we introduce a noninvasive, in situ approach using fluorescence microscopy, providing the capability to distinguish species with subsecond time resolution at single-digit micrometer resolution. This technique holds promise for studying quinone-based systems for carbon capture and beyond.

Effective carbon management is vital for addressing emissions from some of the toughest-to-abate sectors, including heavy industries such as steel production and cement manufacturing[1]. The conventional approach to capturing CO_2 from dilute sources involves amine scrubbing technology, where CO_2 is captured at 40 °C and released at 120 °C (refs. 2,3). In pursuit of more efficient alternatives, researchers have directed their focus toward the development of electrochemical technologies for this purpose. Electrochemical systems offer the advantage of isothermal operation, relying on an electrical gradient to drive a redox reaction that can directly or indirectly create an affinity in the system for CO_2 capture[4–10].

One of the most promising electrochemical carbon capture systems relies on quinone chemistry. Quinones exhibit two potential mechanisms of CO_2 capture. First, the nucleophilicity swing mechanism occurs, where the phenolate groups upon quinone reduction reversibly react with carbon dioxide via nucleophilic addition, which results in the formation of quinone–CO_2 adducts. This mechanism is observed with quinones dissolved in aprotic solvents[11–13] or immobilized on the electrodes[7,11,14,15]. However, in protic solvents, depending on the pK_a of the hydroquinones and the local pH, the electrochemical reduction of quinones can be proton coupled and create hydroxide ions, which capture CO_2 as carbonate or bicarbonate[16–18]. Thus, in an aqueous solvent, both pH swing and nucleophilicity swing mechanisms may contribute to CO_2 capture across a range of operational conditions. However, traditional methods of measuring the total amount of CO_2 captured or released allow for reporting only the combined contribution of these two mechanisms, while the relative contributions are unknown. We expect continued progress in developing aqueous quinone-based

[1]John A. Paulson School of Engineering and Applied Sciences, Harvard University, Cambridge, MA, USA. [2]Department of Chemistry and Chemical Biology, Harvard University, Cambridge, MA, USA. [3]Present address: Department of Materials Engineering, The University of British Columbia, Vancouver, British Columbia, Canada. [4]Present address: Department of Materials Science and Engineering, National University of Singapore, Singapore, Singapore. [5]Present address: Chemistry Department, St. John Fisher University, Rochester, NY, USA. e-mail: maziz@harvard.edu

technologies for carbon capture, attracted by the safety, economic viability and excellent ionic conductivity offered by water serving as a solvent. However, to pave the way for these innovations, it is essential to deepen our understanding of the underlying mechanisms and their relative contributions to overall process performance.

In this Article, we address the need to quantify the contributions of the nucleophilicity swing and pH swing mechanisms. The first two sections lay the foundation for this exploration. First, we provide a thermodynamic overview elucidating the interplay between these mechanisms, emphasizing how the dominance of one over the other influences critical performance metrics of the final engineered electrochemical cell and necessitates specific molecular engineering considerations in the context of the material discovery cycle. Second, we delve into a case study focusing on bis[3-(trimethylammonio)propyl]-anthraquinones (BTMAPAQs)[16], extracting both thermodynamic and kinetic insights for its three isomers. Building on these foundational sections, we introduce two in situ experimental methods for quantifying the contributions of these mechanisms in the system.

Results

Thermodynamic overview

To demonstrate the influence of various properties of the hypothetical anthraquinone molecule employed in the system on the interplay between nucleophilicity swing and pH swing mechanisms, we analyzed a set of reaction equilibrium equations inherent to the system. The fully reduced anthraquinone (AQ^{2-}) molecule in an aqueous solution can either undergo the direct capture of CO_2 through $AQ(CO_2)_2^{2-}$ adduct formation or engage in a proton-coupled reaction

$$AQ^{2-} + 2CO_2(aq) \rightleftharpoons AQ(CO_2)_2^{2-} \qquad K_{AQ\_adduct} = \frac{\left[AQ(CO_2)_2^{2-}\right]}{\left[AQ^{2-}\right][CO_2(aq)]^2} \tag{1}$$

$$AQ^{2-} + 2H^+ \rightleftharpoons AQH_2 \qquad K_{protonation} = \frac{[AQH_2]}{\left[AQ^{2-}\right]\left[H^+\right]^2} \tag{2}$$

where K_{AQ_adduct} and $K_{protonation}$ are the $AQ(CO_2)_2^{2-}$ adduct formation and protonation equilibrium constants, respectively. Both reactions can occur in two steps, involving the sequential acceptance of the first CO_2 or H^+ molecule followed by the second. The experimental determination of K_{AQ_adduct} is elucidated in the next section through cyclic voltammetry, although extracting the equilibrium constant for the initial step in isolation presents challenges. Conversely, the double step protonation/deprotonation can be deduced from the Pourbaix diagram, resulting in the following equilibrium equations:

$$AQH_2 \rightleftharpoons AQH^- + H^+ \quad K_{a_1} = \frac{[AQH^-][H^+]}{[AQH_2]}, \tag{3}$$

$$AQH^- \rightleftharpoons AQ^{2-} + H^+ \quad K_{a_2} = \frac{\left[AQ^{2-}\right][H^+]}{[AQH^-]}. \tag{4}$$

In these reactions, K_{a_1} and K_{a_2} are the equilibrium constants for the first and second deprotonation step, respectively. The corresponding pK_a values are calculated by taking the negative base 10 logarithm of K_a. For reactions 3 and 4, occurring from right to left (protonation reaction), the result is the consumption of protons and an increase in the pH of the solution. The produced hydroxides can then undergo bicarbonate and carbonate formation reactions, resulting in an indirect capture of CO_2

$$CO_2(aq) + H_2O \rightleftharpoons HCO_3^- + H^+ \quad K_4 = \frac{\left[HCO_3^-\right]\left[H^+\right]}{[CO_2(aq)]}, \tag{5}$$

$$HCO_3^- \rightleftharpoons CO_3^{2-} + H^+ \quad K_5 = \frac{\left[CO_3^{2-}\right]\left[H^+\right]}{\left[HCO_3^-\right]}. \tag{6}$$

Reactions 1–6 involve the consumption or production of various charge species. In the solution, charge neutrality must always be maintained. Thus

$$\begin{aligned} &+2[AQ^{2-}] + 2\left[AQ(CO_2)_2^{2-}\right] + [AQH^-] + [OH^-] \\ &+ \left[HCO_3^-\right] + 2\left[CO_3^{2-}\right] - \left[H^+\right] - [M^+] = 0 \end{aligned}, \tag{7}$$

where M^+ represents the counterion resulting from dissolving the anthraquinone salt in the solution (for example, K^+ or Na^+). Additionally, the sum of concentrations of all AQ-containing molecules is conserved at its total dissolved concentration (C_T). Therefore

$$+\left[AQ^{2-}\right] + \left[AQ(CO_2)_2^{2-}\right] + [AQH^-] + [AQH_2] - (C_T) = 0. \tag{8}$$

An additional constraint arises from the water dissociation equilibrium, resulting in

$$H_2O \rightleftharpoons OH^- + H^+ \quad K_w = [OH^-]\left[H^+\right]. \tag{9}$$

Finally, the concentration of the $CO_2(aq)$ is dictated by the partial pressure of CO_2 (p_{CO_2}) and follows Henry's Law

$$[CO_2(aq)] = C_{Henry} p_{CO_2}, \tag{10}$$

where C_{Henry} is the Henry's constant, taken to be 35 mM per bar at room temperature[9], representing its solubility in water and assumed to be unchanged in the presence of 0.1 M AQ. Given that the present thermodynamic analysis serves as an overview of the interplay between the nucleophilicity swing and pH swing mechanisms, we focus on the above main reactions, while those leading to intermediate compounds such as $AQ(CO_2)^{2-}$ and $AQHCO_2^-$ and species formed owing to mixed mechanisms are assumed to be disregarded for lack of estimation for them and for simplicity.

Here, we begin by considering a total concentration of 0.1 M AQ dissolved under a partial pressure of 0.1 bar. With pK_{a1} and pK_{a2} set at 11 and 13, respectively—values typical for several anthrahydroquinones reported so far[16,19–21]—we further consider equilibrium constants K_4, K_5 and K_w as 1.1×10^{-6} M (ref. 22), 4.1×10^{-10} M (ref. 22) and 1×10^{-14} M^2, respectively. Regarding the equilibrium constants for bicarbonate and carbonate formation, we assume that the presence of 0.1 M AQ has not substantially altered the salinity of the solution and the numbers are taken at a salinity of zero. Under these specified conditions, Fig. 1a illustrates the dynamic interplay between nucleophilicity swing and pH swing mechanisms in the capture of CO_2 as a function of the $AQ(CO_2)_2^{2-}$ adduct formation equilibrium constant. This analysis predicts that, at K_{AQ_adduct} less than 1×10^{12} M^{-2}, the thermodynamic driving force for the nucleophilicity swing mechanism is too low and thus the CO_2 capture proceeds mainly via the pH swing mechanism. The opposite is correct for K_{AQ_adduct} values above 1×10^{17} M^{-2}. Between these two limits, both mechanisms contribute to the capture of CO_2. Understanding this interplay in relation to the properties of the employed molecule is crucial in the context of the material discovery cycle for carbon capture applications. For instance, if a newly synthesized molecule, under the desired operational conditions, exhibits primarily the pH swing capture mechanism, optimizing the molecule's capture capacity necessitates a focus on maximizing its pK_a, as well as solubility, to increase the concentration of OH^- molecules produced. Conversely, for molecules with strong adduct formation equilibrium constants, maximizing pK_a becomes irrelevant, and attention should be directed merely toward enhancing the solubility of the AQ molecule.

https://doi.org/10.1038/s44286-024-00153-y

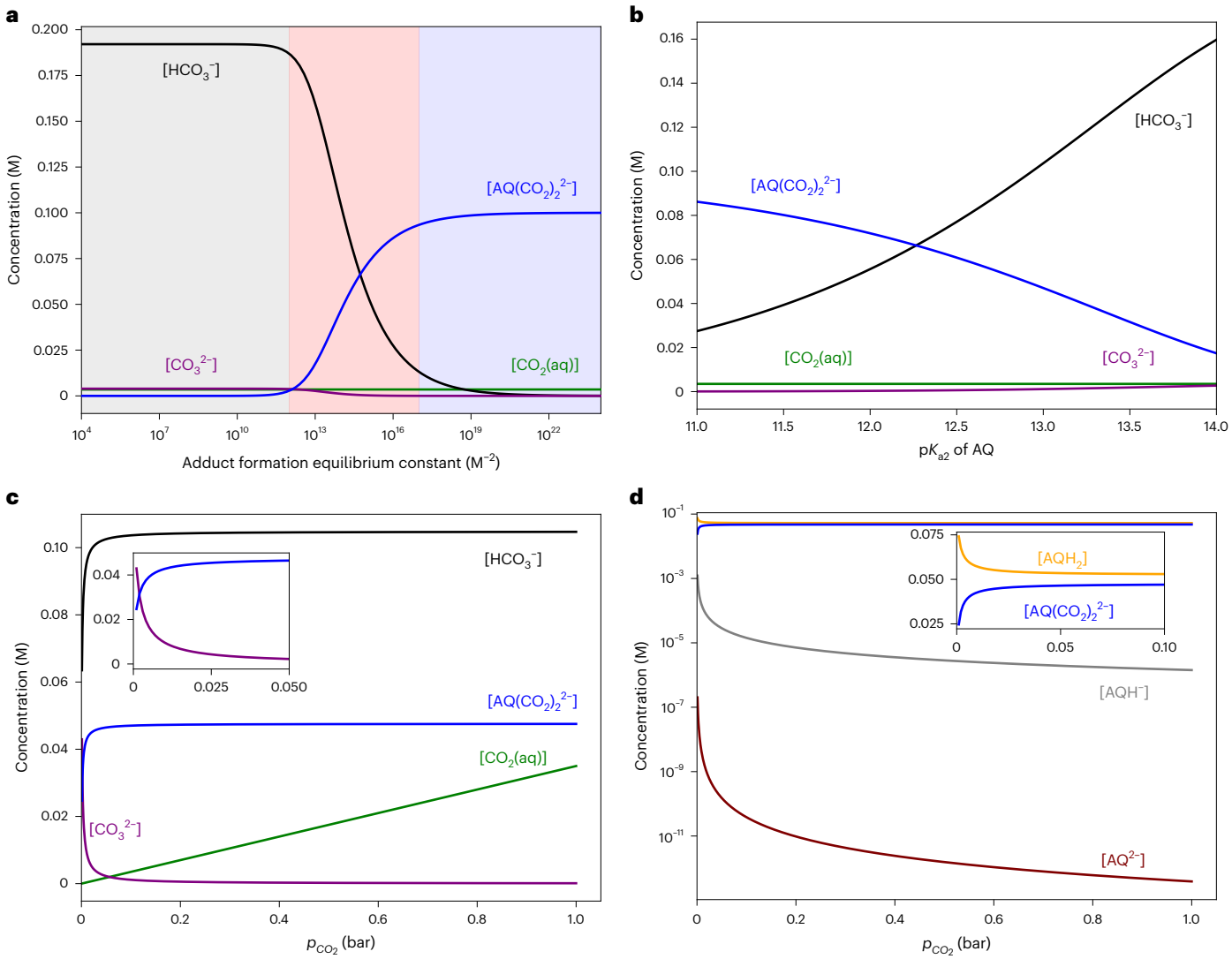

Fig. 1 | Equilibrium concentrations resulting from solving equilibrium equations. Unless specified, a total concentration of 0.1 M AQ dissolved under a partial pressure of 0.1 bar is assumed. The AQ pK_{a1} and pK_{a2} values are set at 11 and 13, respectively, with equilibrium constants K_4, K_5 and K_w at 1.1×10^{-6} M, 4.1×10^{-10} M and 1×10^{-14} M^2, respectively, and K_{AQ_adduct} of 1×10^{14} M^{-2}. **a**, The concentration profiles of HCO_3^-, CO_3^{2-}, CO_2 (aq) and $AQ(CO_2)_2^{2-}$ at different K_{AQ_adduct} values. **b**, The concentrations of HCO_3^-, CO_3^{2-}, CO_2 (aq) and $AQ(CO_2)_2^{2-}$ at varying pK_{a2} values of the AQ molecule. **c**, The concentrations of HCO_3^-, CO_3^{2-}, CO_2 (aq) and $AQ(CO_2)_2^{2-}$ at different partial pressures of CO_2. **d**, The concentrations of AQ^{2-}, $AQ(CO_2)_2^{2-}$ and AQ, AQH^- at different partial pressures of CO_2.

It is important to note that basicity and nucleophilicity are intrinsically linked as both properties are governed by the electron-donating ability of the molecule. Consequently, these properties cannot be independently modified in isolation. However, the molecular structure can be strategically optimized to favor either of the two mechanisms (examples are provided in Supplementary Information). The results of such an optimization are illustrated in Fig. 1b,c and Supplementary Fig. 1. For intermediate values of K_{AQ_adduct} (for example, 1×10^{14} M^{-2}), where both mechanisms are at play, increasing the pK_a of the AQ molecule shifts the contribution more toward bicarbonate/carbonate formation, as depicted in Fig. 1b and the zoomed-in image in Supplementary Fig. 1d. In contrast, under conditions where K_{AQ_adduct} is strong (for example, 1×10^{22} M^{-2}), even with limited pK_a values (for example, pK_{a1} = 7 and pK_{a2} = 7), the $AQ(CO_2)_2^{2-}$ adduct formation mechanism captures up to the expected capacity independent of enhancements in pK_{a2} (Supplementary Fig. 1a). However, under such limiting conditions, when K_{AQ_adduct} is weak (for example, 1×10^4 M^{-2}), increasing the pK_a of the anthrahydroquinone molecule becomes a crucial factor for enhancing the capture capacity, as depicted in Supplementary Fig. 1a. Note that capture capacity is defined as the molar ratio of CO_2 molecules captured to AQ molecules present.

Another important factor is the effect of the CO_2 partial pressure. Under the conditions set in Fig. 1a and for intermediate values of K_{AQ_adduct} (for example, 1×10^{14} M^{-2}), where both mechanisms are at play, increasing p_{CO_2} to values higher than 0.1 bar would indeed increase the CO_2 (aq) concentration according to Henry's law, but it results in negligible change in the individual contribution of nucleophilicity swing and pH swing mechanisms toward the total capture, as shown in Fig. 1c,d. However, at dilute CO_2 concentrations (less than 0.05 bar), the thermodynamic driving force for $AQ(CO_2)_2^{2-}$ adduct formation drops and, in the bicarbonate/carbonate equilibration, carbonate formation contribution increases, which would have an effect on the capacity of the capture. In the adduct formation pathway, each AQ molecule captures two CO_2 molecules by engaging both nucleophilic oxygen sites. Meanwhile, in the pH swing pathway, a two-step protonation process yields two OH^- ions per AQ molecule. When these hydroxides

https://doi.org/10.1038/s44286-024-00153-y

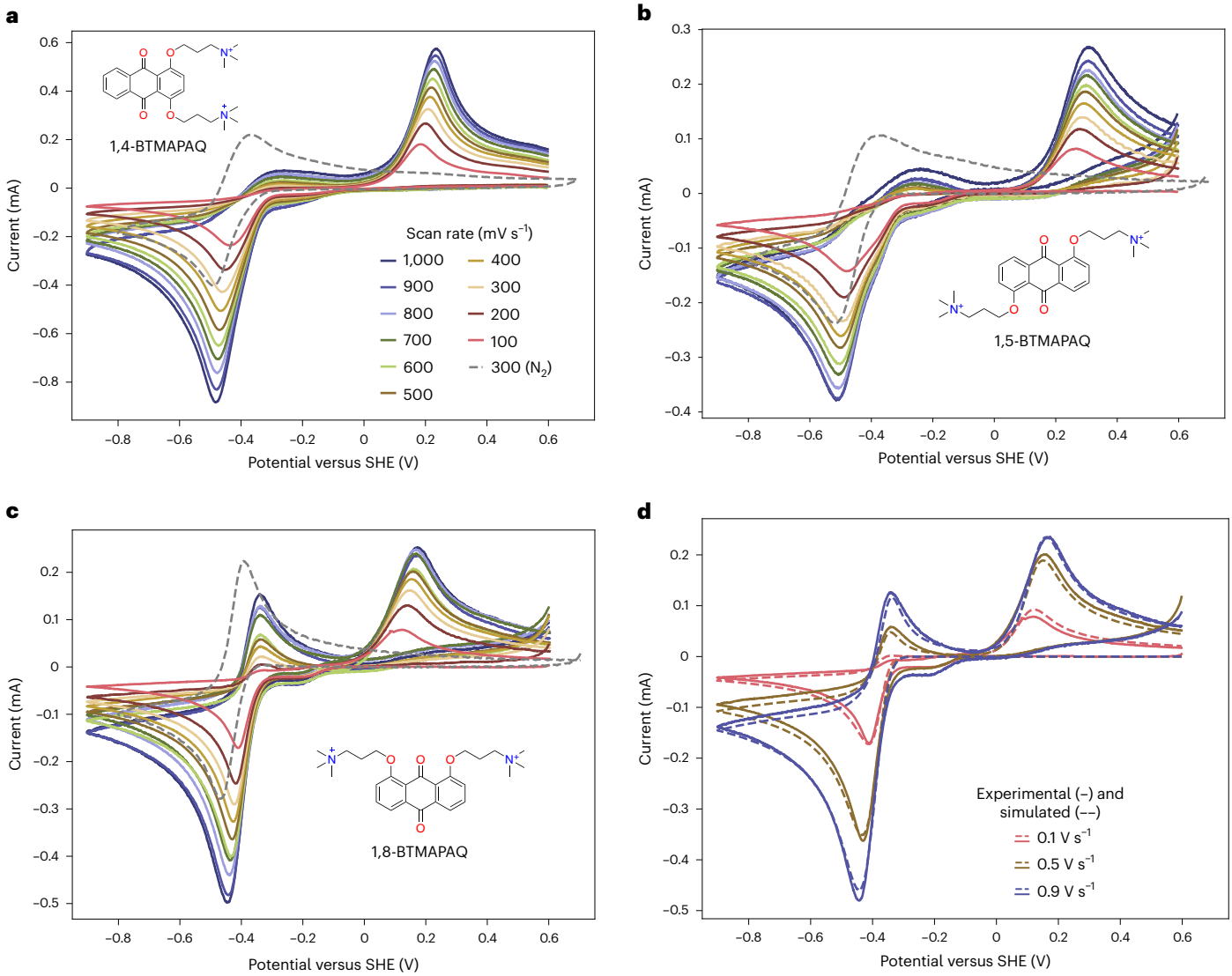

Fig. 2 | Molecular structures and cyclic voltammetry profiles of BTMAPAQ isomers. a–**c**, The cyclic voltammetry profiles for 5 mM of 1,4-BTMAPAQ (**a**), 1,5-BTMAPAQ (**b**) and 1,8-BTMAPAQ (**c**) dissolved in 1 M KCl under a pure CO_2 headspace at different scan rates between 100 mV s^{-1} and 1,000 mV s^{-1}. For comparison, the cyclic voltammetry profile under a pure N_2 headspace is also depicted as a dashed line at a scan rate of 300 mV s^{-1} for each isomer. **d**, The experimental (solid lines) and fitted (dashed lines) cyclic voltammetry profiles of 1,8-BTMAPAQ for three scan rates of 0.1 V s^{-1}, 0.5 V s^{-1} and 0.9 V s^{-1}.

predominantly form bicarbonate groups, each OH^- captures one CO_2, resulting in a two CO_2 capture capacity per one AQ molecule. Contrastingly, carbonate formation consumes two OH^- ions, resulting in a one CO_2 capture capacity per one AQ molecule. Therefore, $AQ(CO_2)_2^{2-}$ adduct formation and bicarbonate formation both exhibit a capture capacity ratio of two to one, while carbonate formation yields a one to one ratio. In the context of the interplay between nucleophilicity swing and pH swing mechanisms, one can see that for the molecules where K_{AQ_adduct} is strong (for example, 1×10^{22} M^{-2}), the thermodynamic driving force for $AQ(CO_2)_2^{2-}$ adduct formation is very strong and even at dilute CO_2 concentrations (400 ppm) the capture capacity proceeds at a two to one ratio through nucleophilicity swing mechanisms (Supplementary Fig. 1b). Conversely, when K_{AQ_adduct} is weak (for example, 1×10^4 M^{-2}), the dominant mechanism becomes pH swing and reducing the p_{CO2} to values less than 0.05 bar shifts the equilibrium toward carbonate formation, diminishing the capture capacity to a one to one ratio, which is particularly relevant for cells engineered for direct air capture where CO_2 partial pressure is low. The potential impact of these mechanisms on the performance is further discussed in Supplementary Information.

Thermodynamic and kinetic analysis of BTMAPAQ isomers

In this section, we present a case study for the specific case of BTMAPAQ isomers[16], as a representative compound in aqueous quinone-mediated carbon capture systems. Figure 2a–c illustrates the cyclic voltammetry (CV) of 1,4-, 1,5- and 1,8-BTMAPAQ isomers at various scan rates under a pure stream of CO_2 and at one scan rate under pure N_2. The CV plots of the isomers at all other scan rates under a pure N_2 headspace is further shown in Supplementary Fig. 2. For each isomer, a new oxidation peak emerges under the CO_2 headspace, shifted to more positive potentials compared with that under pure N_2 headspace, while the reduction peak remains almost identical. The more positive oxidation peak corresponds to the newly formed $AQ(CO_2)_2^{2-}$ redox-active species, which cannot exist under the pure nitrogen environment. The less positive redox potential is attributed to the AQ^{2-} oxidation given that it is occurring under the nitrogen headspace. In the nucleophilicity swing mechanism, the oxidation potential of $AQ(CO_2)_2^{2-}$ is substantially more positive compared with the pH swing mechanism, where AQH_2 demonstrates a more negative oxidation peak, proximal to the reduction peaks of AQ^{2-}. These differences critically influence the thermodynamic energy requirements and oxygen stability of the

system (Supplementary Information). In the thermodynamic context, the equilibrium constants for $AQ(CO_2)_2^{2-}$ adduct formation (K_{AQ_adduct}) for these isomers can be deduced by examining the difference in the half-wave potential peaks associated with the AQ^{2-} and $AQ(CO_2)_2^{2-}$ redox reactions[23] through equation (S1) in Supplementary Information. Using this equation, we find the K_{AQ_adduct} to be 1.6×10^{22}, 7.3×10^{21} and 2.8×10^{18} M^{-2} for the isomers 1,4-, 1,5- and 1,8-BTMAPAQ, respectively. Compared with the predictions from the equilibrium model shown in Fig. 1a, these are attributed to a very strong $AQ(CO_2)_2^{2-}$ adduct formation region, predicting a system dominated by the nucleophilicity swing mechanism.

To gain some understanding of the kinetics of the reaction, we conducted the CV tests under different scan rates as shown in Fig. 2a–c. At higher scan rates, the CV is swept faster across the same potential range, resulting in a quicker run. Given that under CO_2, a chemical reaction is occurring ($AQ(CO_2)_2^{2-}$ adduct formation, according to equation (1)), there would be less time for the chemical reaction to proceed at higher scan rates. It can be observed that for the 1,4- and 1,5-BTMAPAQ isomers, increasing the scan rate would barely result in any current being extracted at the oxidation potential attributed to the oxidation of AQ^{2-}, which implies that the chemical quinone adduct formation reaction is occurring at rates faster than the scan rates used. Thus, even at 1,000 mV s^{-1}, we extract current predominantly from $AQ(CO_2)_2^{2-}$. Interestingly, for the 1,8-BTMAPAQ isomer, increasing the scan rate reveals a growing peak at the oxidation potentials related to AQ^{2-} oxidation, which indicates that the chemical reaction rate of $AQ(CO_2)_2^{2-}$ adduct formation is slower for this isomer compared with the other two isomers and cannot keep up with the fast rate of potential change. To quantify the kinetic rates associated with the $AQ(CO_2)_2^{2-}$ adduct formation reaction, we fit experimental CV data to a reaction scheme assuming an electrochemical–chemical–electrochemical mechanism, with details extensively described in the Supplementary Information. Examples of a fitting for 1,8-BTMAPAQ are shown in Fig. 2d and the rest of the fittings are provided in Supplementary Figs. 5–7, indicating a very good agreement between the model and the experimental data. For 1,4- and 1,5-BTMAPAQ isomers, an increase in scan rate barely results in current extraction at the potential relevant to AQ reduction. Therefore, we report a lower limit on k_c for these two isomers, below which the chemical reaction would be too slow to keep up with the fast scan rates. However, for 1,8-BTMAPAQ, an exact value of k_c, rather than a limit, is reported.

The extracted parameters for the three isomers are presented in Supplementary Table 1. The k_c values are >6.7, >6.0 and 2.4 s^{-1}, which would be >192, >171 and 68.6 M^{-1} s^{-1} (per moles of CO_2) for 1,4-, 1,5- and 1,8-BTMAPAQ isomers, respectively, indicating the rate constant for the occurrence of the nucleophilicity swing mechanism. In contrast, the rate constant for bicarbonate/carbonate formation that is occurring in the pH swing mechanism is reported to be 12.1×10^3 M^{-1} s^{-1} at 25 °C (ref. 24), substantially higher than what we are reporting for the $BTMAPAQ(CO_2)_2^{2-}$ adduct formation mechanism. Having obtained the rate constants, we can predict the rates of both bicarbonate formation and the formation of the $BTMAPAQ(CO_2)_2^{2-}$ adduct under various conditions (Supplementary Information), which demonstrates the extent to which bicarbonate formation can proceed more rapidly than the $BTMAPAQ(CO_2)_2^{2-}$ adduct formation. This comparison highlights that although thermodynamically we predict the $BTMAPAQ(CO_2)_2^{2-}$ adduct formation mechanism to occur predominantly for these three isomers, kinetically the pH swing mechanism is faster. As such, each mechanism exhibits different kinetic and reaction rates, which affect the overall rate of CO_2 capture in the designed system (Supplementary Information).

In situ methods

The previous two sections underscore the necessity for an experimental methodology capable of discerning the intricate interplay between the pH swing and nucleophilicity swing mechanisms (Supplementary Information). As shown in Supplementary Fig. 12, using pH as an indicator for the amount of OH^- formed during the reaction is insufficient, primarily owing to the buffering effect of the carbonate/bicarbonate system. In the following sections, we introduce two in situ experimental techniques designed for this purpose.

Reference electrodes. The cyclic voltammetry plots depicted in Fig. 2 reveal the distinct oxidation potential signature of the $BTMAPAQ(CO_2)_2^{2-}$ adduct in comparison with the reduced BTMAPAQ molecules. This discernible voltage separation, observed in multiple cases of other quinones[7,23], should allow us to accurately quantify the contribution of nucleophilicity swing toward total carbon capture. To illustrate this method and investigate its sensitivity, we conducted experiments utilizing a flow cell equipped with a reference electrode on the negative side (BTMAPAQ side), which allows us to measure the real-time potential of the negative electrode against the reference electrode (Supplementary Information). Utilizing this setup, the cell was intentionally charged (Supplementary Information) in a nitrogen environment, followed by a controlled purge with 0.1 bar CO_2 and 0.9 bar of N_2 for varying durations (60 min in Fig. 3a), followed by a switch back to the nitrogen environment. This experimental procedure with different CO_2 purge durations (15, 30 and 60 min) was intentionally designed to allow us to control the amount of adduct formation during the course of the experiment and examine its relationship with the discharge voltage profiles (see Supplementary Information for flow battery operation details, experimental setup and calibration procedure).

The voltage profile depicted in Fig. 3a is zoomed in the upper plot of Fig. 3b, accompanied by its corresponding negative half-cell potential measured from the reference electrode. Two distinct plateaus emerge in the full-cell voltage profile (Fig. 3a, dashed gray square), mirroring the double plateaus identified in the negative half-cell potential plot. The more negative discharge potential, averaged at −0.3 V versus standard hydrogen electrode (SHE), aligns well with the oxidation potential of the reduced species from the cyclic voltammetry profiles, while the less negative half-cell potential at 0.1 V versus SHE is close to the adduct species' potential signature. We attribute the differences between the cell potential and the CV potentials to the possible local pH and electrolyte composition differences (see Supplementary Information for an explanation of the variation of half-cell potentials across experiments). Given this distinctive potential separation, we can calculate the adduct formation by examining the capacity delivered at the voltage signature of the quinone adduct compound. As depicted in Fig. 3c, extending the duration of purging with CO_2 from 15 min to 60 min clearly shows an increase in the capacity delivered at the potential signature of the adduct species. In separate experiments, we purged with 0.1 bar CO_2/0.9 bar of N_2 from the beginning of the experiment with a 120 min purging during the rest time, clearly demonstrating that such a prolonged purging duration would increase the capacity delivered by the adduct. Eventually, in the case of 7 h of purging, the entire discharge capacity is exclusively delivered by the $BTMAPAQ(CO_2)_2^{2-}$ adduct species.

Figure 3d (top) illustrates the CO_2 release volume calculated both from CO_2 sensor measurements and the oxidation voltage signature of the $BTMAPAQ(CO_2)_2^{2-}$ adduct for the experiments in Fig. 3a,b (Supplementary Information). The volume obtained from the CO_2 sensor includes the combined contribution of nucleophilicity swing and pH swing mechanisms (Fig. 3a, dashed red squares), while the CO_2 volume determined by deducing the adduct concentration from the half-cell discharge voltages represents solely the contribution of the $BTMAPAQ(CO_2)_2^{2-}$ adduct. As a result, the disparity between these two values is attributed to the pH swing mechanism. Interestingly, the contribution of the pH swing mechanism versus the nucleophilicity swing mechanism changes across these experiments. In Fig. 3d (bottom), the percentage contribution of each mechanism to the total

https://doi.org/10.1038/s44286-024-00153-y

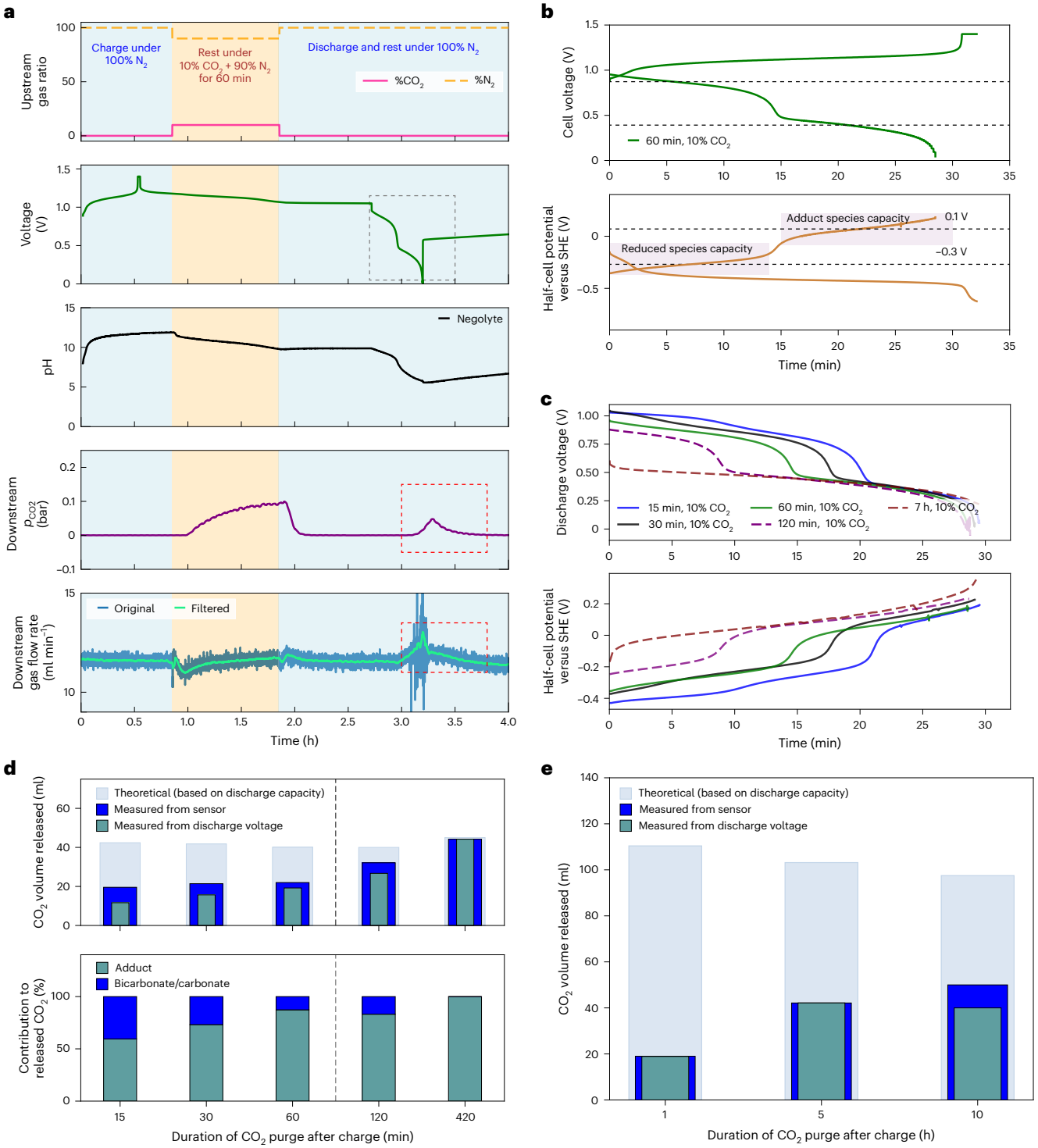

Fig. 3 | Flow cell operation of BTMAPAQ with in situ reference electrode. **a**, The upstream gas ratio, voltage, pH, measured partial pressure of CO_2 and flow rate at the downstream measured during the experiment utilizing a flow cell comprising 12 ml of 0.1 M 1,5-BTMAPAQ paired with 40 ml of 0.2 M BTMAPFc. The cell was charged in a nitrogen environment, followed by a controlled purge with 0.1 bar CO_2 and 0.9 bar N_2 for 60 min, followed by a switch back to the nitrogen environment. **b**, Zoomed-in full-cell voltage of the battery shown in Fig. 3a (top) and negative half-cell potential measured via in situ reference electrode during operation (bottom). **c**, Full-cell and negative half-cell potentials of the cell operated under different duration of CO_2 purge time. The solid lines depict experiments where the charge itself was conducted under N_2, whereas for the dashed line experiments, the purging with CO_2 is conducted from the beginning of the charge phase. **d**, The CO_2 release volume calculated from the CO_2 sensor measurements and the oxidation voltage signature of the adduct (top). For comparison, the maximum theoretical CO_2 release volume calculated from the total discharge capacity is also shown. The percentage contribution of each mechanism to the total capture amount (bottom). The vertical dashed lines distinguish experiments with CO_2 purging only during rest (left) from those with prolonged CO_2 purging starting from charge and continuing into rest (right). **e**, The CO_2 release volume calculated from the CO_2 sensor measurements and the oxidation voltage signature of the adduct for 7 ml of 0.4 M of 1,4-BTMAPAQ and very diluted CO_2 concentrations of 0.01 bar (1% CO2, 99% N_2) under different rest durations. Note that the CO_2 sensor has an accuracy of ±300 ppm ±5% of the reading, and the flow meter has an accuracy of ±1.5% (0–30 standard cubic centimeter per minute (sccm)) based on their specifications (Supplementary Information).

capture amount is presented. For the short, 15 min duration tests, we observe a 40% contribution from the pH swing mechanism. However, with a prolonged, 7 h purge time, the capture predominantly occurs through the nucleophilicity mechanism. This observation aligns very well with our earlier discussions on the thermodynamic and kinetic predictions for the BTMAPAQ isomers, demonstrating the slow kinetics of the nucleophilicity swing mechanism compared with the pH swing mechanism, but the eventual equilibrium domination of the nucleophilicity swing mechanism. The experiments with shorter purge times show a 40% contribution from the pH swing mechanism, while longer purge times demonstrate the complete dominance of the nucleophilicity swing mechanism, which indicates that, if the molecules were detected in real time during the capture phase, an exchange reaction between the organic carbonate adduct and inorganic carbonate would be expected. This observation draws parallels to the reported self-exchange electron-transfer reactions observed between diamagnetic and paramagnetic ions of anthraquinones[25]. The observed potential exchange reaction is intriguing and warrants further investigation. Furthermore, to show the applicability of the method, we conducted the method under different sets of conditions, that is, tests for a different isomer 1,4-BTMAPAQ at high concentrations of 0.4 M and very diluted CO_2 concentrations of 0.01 (1% CO_2, 99% N_2) (Supplementary Fig. 20). At these high AQ concentrations, the salinity of the solution deviates from the assumptions made in our equilibrium modeling scheme, and thus we do not draw expectations from our model. However, we can expect that the high AQ concentration combined with the dilute CO_2 partial pressure should substantially increase the likelihood of AQ binding with CO_2 over bicarbonate/carbonate formation. Figure 3e illustrates the measurements conducted over different durations of purge time (1–10 h). In these experiments at high concentrations of BTMAPAQ, we indeed observe the dominance of the nucleophilicity swing mechanism in all tests. Note that, owing to the extremely low concentrations of CO_2, extended purge durations are necessary to achieve high capture capacities.

In this electrolyte, effectively a mixture of two redox-active species (reduced and the adduct) has formed. As per our prior work on mixed organic redox-active species[26], when the potential separation between two mixed species is over 300 mV, the concentration of the first redox species is consumed before the second redox event begins. This means that for the present case, the capacity at each plateau can be directly correlated with the corresponding species concentration. However, for close potential separations (<300 mV), a modeling scheme such as the one developed in our prior work[26] must be used for the accurate prediction of the concentrations.

It is crucial to note that, although this method is conducted in situ, meaning measurements are taken during the test, it is essentially an 'aftermath' method as we cannot quantify the concentration of the quinone adduct species until the discharge occurs and we examine the discharge voltage profiles. In the next section, we introduce a method for the real-time measurement of the adduct during the capture phase.

Fluorescence microscopy-based visualization. We first investigated the real-time absorbance of the 1,5-BTMAPAQ species by integrating an in situ ultraviolet–visible (UV–vis) spectrometer into the electrolyte flow path in an operating flow cell, as illustrated in Supplementary Fig. 23. Figure 4a shows the absorbance spectra of 5 mM 1,5-BTMAPAQ in 1 M KCl within a flow cell, operating against 20 mM bis((3-trimethylammonio)propyl)ferrocene dichloride (BTMAPFc) under a 100% N_2 stream to capture the real-time absorbance profiles during reduction of 1,5-BTMAPAQ in the absence of any 1,5-BTMAPAQ$(CO_2)_2^{2-}$ adduct. Under these conditions, five distinct peaks at wavelengths of 223, 251, 391, 487 and 523 nm are evident. During charging, the 223 nm peak decreases in absorbance, and the 251 nm and 391 nm peaks increase, with a new peak emerging at 430 nm, corresponding to the conversion of the molecule from its oxidized form to the reduced form. Subsequently, the battery was brought to rest, and UV–vis spectra were monitored as a 50% CO_2/50% N_2 stream is introduced to form the adduct (Fig. 4b). Comparing the spectra at $t = 0$ and after half an hour of purging with CO_2, we observed minor absorbance changes, particularly at 251, 391 and 487 nm, indicating a similarity between the spectra of the reduced species and the adduct, which poses a challenge for precise quantification of the species using this method. Further experiments described in the Supplementary Information similarly revealed minor changes between the two spectra. Consequently, we shifted our focus to fluorescence spectroscopy.

Figure 4c,d shows the emission spectra of the oxidized, reduced and adduct species of 1,5-BTMAPAQ, obtained ex situ using a fluorescent plate reader (for experimental details, see the Supplementary Information). Figure 4c,d illustrates the emission spectra of species excited at 405 nm and 475 nm, respectively. In both cases, the oxidized species shows almost no fluorescence, whereas, interestingly, both the reduced and the adduct species exhibit fluorescence, with the adduct form displaying substantially higher intensity. This intriguing trend does not appear to be unique to this molecule. We observed a similarly high fluorescence intensity in the adduct for other anthraquinones, including 2,2′-((9,10-dioxo-9,10-dihydroanthracene-2,6-diyl)bis(oxy))-dipropionic acid (2,6-D2PEAQ)[19] and 2-2-propionate ether anthraquinone (22PEAQ)[27], as demonstrated in Supplementary Fig. 25. Note that the solutions contain mixtures of different forms of the anthraquinone, for example, the reduced solution contains the collection of AQ^{2-} as well as AQH^- and AQH_2. This mixture may induce diverse energy transition states, influencing the emission intensity in response to varying excitation wavelengths. However, the noteworthy insight gathered from these figures is that, through a careful selection of emission wavelength regions, we can identify areas where the fluorescence signatures of the reduced, oxidized and adduct species of 1,5-BTMAPAQ are distinct enough to potentially enable quantification of the BTMAPAQ$(CO_2)_2^{2-}$. Specifically, when considering an emission wavelength close to 520 nm for compounds excited at 405 nm (Fig. 4c), we observe that the adduct form still exhibits high fluorescence, while the reduced species approaches the bottom of its emission peak. Conversely, at an emission wavelength near 600 nm for compounds excited at 475 nm (Fig. 4d), the opposite is observed. Furthermore, the emission spectra of the pure bicarbonate/carbonate solutions do not show any fluorescence properties that differ from the background pH 14 solution, as depicted in Supplementary Fig. 26. This emission analysis procedure can be adapted for different conditions (Supplementary Information).

Next, we proceeded by developing a custom-designed optically transparent microfluidic electrochemical flow cell (Fig. 5a) that can be integrated into a fluorescence microscope and is compatible with optical imaging. Figure 5b displays the widefield image of the porous electrode extracted from this cell, while Fig. 5c provides a schematic of the experimental setup (Supplementary Information). To investigate the potential correlation between fluorescence intensity at wavelengths identified by the ex situ study and the adduct concentration, we designed an experiment wherein the battery is initially charged under N_2, followed by the introduction of CO_2. Figure 5d,e shows the data associated with the operation of the described microfluidic cell under the fluorescent microscope, where two channels with different excitation/absorption settings were established for monitoring, one with excitation–emission wavelengths of 488–594 nm and the other with 405–521 nm, respectively. At the initial time point ($t_0 = 0$), no fluorescence is evident, consistent with the ex situ data, attributed to the oxidized compound not fluorescing within the chosen wavelengths. As the charging process begins and progresses under a nitrogen atmosphere, the reduced form becomes fluorescent (channel 1, $t_1 = 2{,}894.5$ s), with intensity increasing alongside the charging capacity. During this period, there is a minor change in the fluorescence intensity of channel 2, as expected due to the absence of any adduct

https://doi.org/10.1038/s44286-024-00153-y

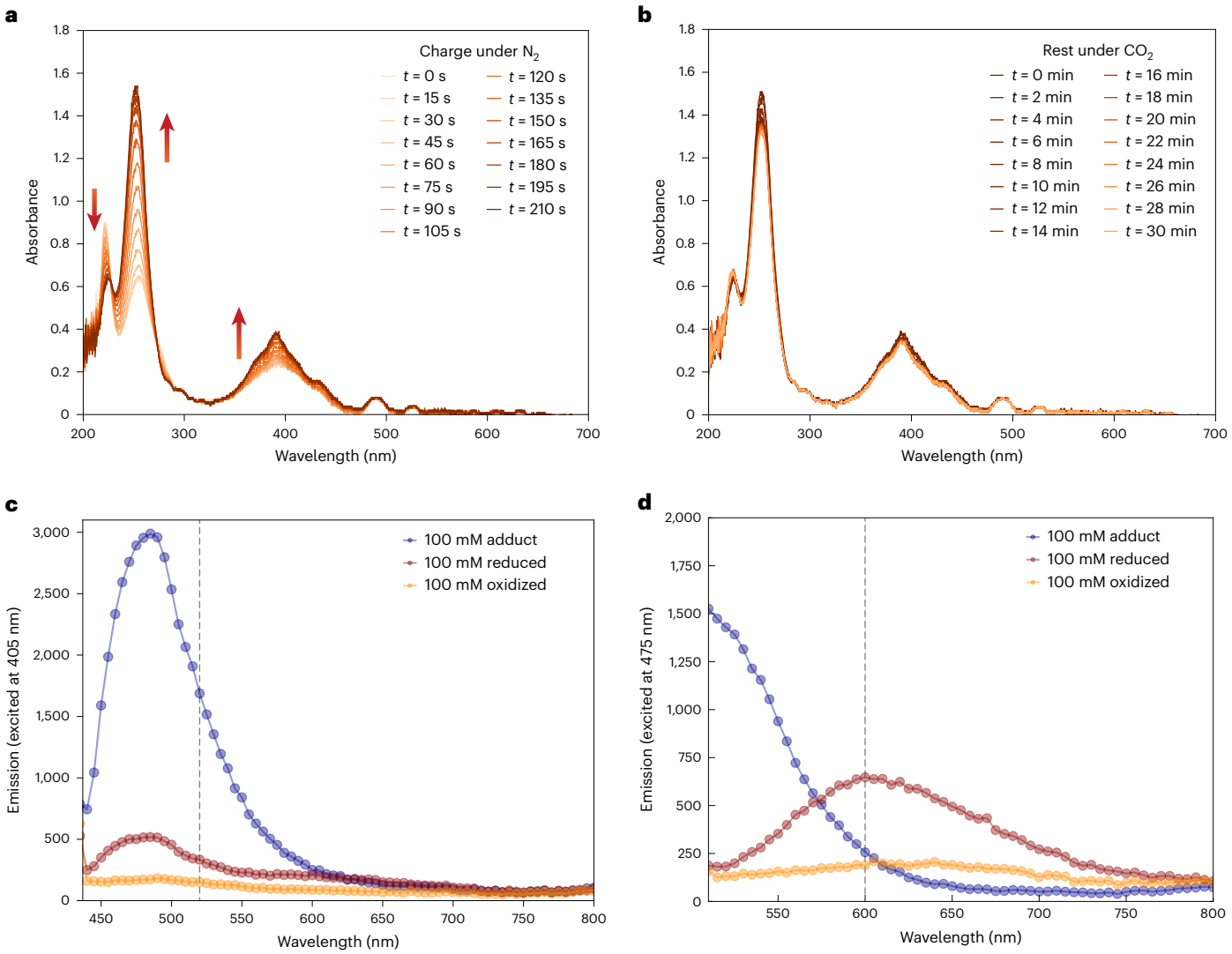

Fig. 4 | Absorbance and emission spectra of 1,5-BTMAPAQ under different experimental conditions. a, The in situ absorbance spectra of 5 mM 1,5-BTMAPAQ dissolved in 1 M KCl during the charging phase (reduction of BTMAPAQ) in a battery operating versus 40 mM BTMAPFc in 1 M KCl under pure nitrogen phase. The absorbance spectra were taken until the charge was complete. The downward and upward arrows indicate the decrease and increase, respectively, in absorbance at specific wavelengths over time during the charging process under a nitrogen atmosphere. **b**, The in situ absorbance spectra of 5 mM 1,5-BTMAPAQ dissolved in 1 M KCl taken during the rest time immediately after the charging phase. In the first minute, 50% CO_2/50% N_2 was introduced to the solution. **c**, The ex situ fluorescence spectra of 100 mM of the adduct, reduced and oxidized species of 1,5-BTMAPAQ excited at 405 nm. **d**, The ex situ fluorescence spectra of 100 mM of the adduct, reduced and oxidized species of 1,5-BTMAPAQ excited at 475 nm. The vertical dashed lines in **c** and **d** mark specific emission wavelength regions that differentiate the fluorescence signals of quinone adduct and reduced quinone species.

species. Subsequent purging with CO_2 (1 bar) induces the conversion of the reduced form to the CO_2–quinone adduct, resulting in the loss of fluorescence in channel 1. Meanwhile, channel 2, characterized by a distinct fluorescence signal from the adduct, becomes intense. Upon discharging, the fluorescence gradually fades (t_3 = 4,140.5 s). During the discharging phase, we intentionally altered the discharge current rate to demonstrate the correlation between the intensity change and the rate of discharge, as evidenced by the comparison between the discharge capacity and intensity plots in Fig. 5d. CO_2 gas bubbles formed as a result of the CO_2 release during discharge are also evident (Supplementary Video 1), more clearly observed near the outlet of the cell where bubble accumulation occurs.

While the intensity appears to correlate with the concentration of the BTMAPAQ$(CO_2)_2^{2-}$ adduct, for this method to be applicable for quantification, we must calibrate the measurement, that is, establish a correlation between intensity and concentration under a known condition. The most rigorous approach is either to inject a known concentration of the isolated solution of adduct into the cell and measure the emission intensity or to upgrade the setup with a downstream CO_2 sensor and flow meter and a reference electrode. This allows for measuring the potential of the negative half cell against a reference under a known condition, creating a standard concentration–intensity calibration plot. In this proof of concept, we make an assumption that operating the microfluidic cell under a pure stream of CO_2 (1 bar) from the beginning of the charging process facilitates BTMAPAQ$(CO_2)_2^{2-}$ adduct formation and results in the full dominance of BTMAPAQ$(CO_2)_2^{2-}$ adduct, consistent with our thermodynamic view. Under such an assumption, the fully charged capacity of 37 C measured by the potentiostat is attributed to the production of the adduct, which can be correlated with the 6,000 units of intensity measured by the microscope in channel 2. Utilizing this established calibration, we then conducted an experiment involving a charging phase under a pure nitrogen stream, followed by purging the system with a pure stream of CO_2 to capture carbon dioxide for only a short wait time afterward.

https://doi.org/10.1038/s44286-024-00153-y

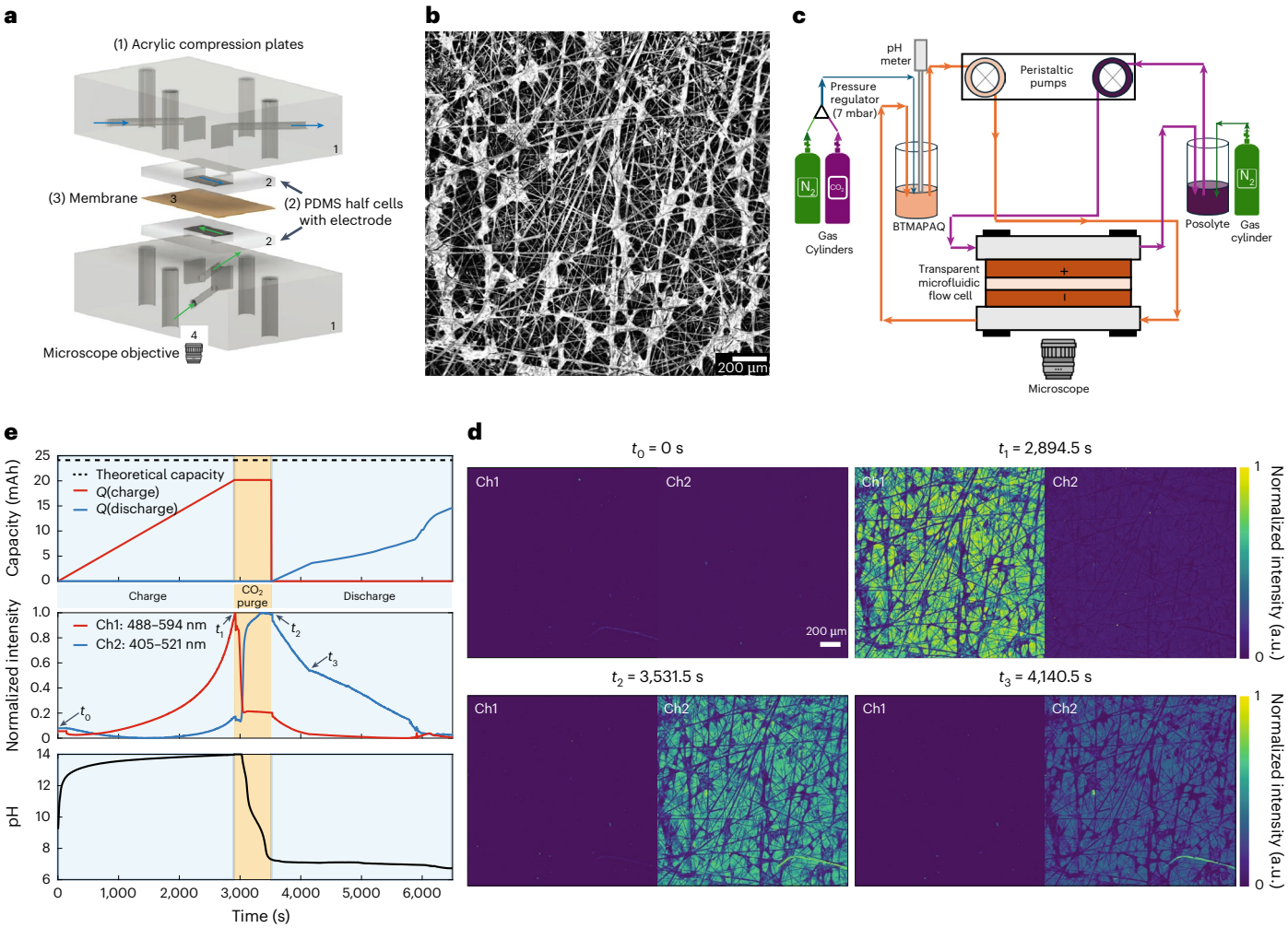

Fig. 5 | In situ electrochemical fluorescence microscopy for carbon capture: setup and operation. a, A schematic of the custom-designed optically transparent microfluidic inspired flow cell designed for the in situ electrochemical investigation. **b**, A widefield optical microscopy image of the porous carbon paper electrode inside the electrochemical cell. **c**, The experimental setup for the study of the electrochemical carbon capture flow cells using in situ fluorescence microscopy. **d**, The capacity, averaged over an entire image normalized intensity (normalized based on the initial intensity), and pH during the operation of the microfluidic cell containing 4 ml of 0.1 M 1,5-BTMAPAQ in 1 M KCl paired with 20 ml of 0.2 M BTMAPFc in 1 M KCl under a fluorescence microscope. **e**, The normalized intensity at a pixel level (1 µm) of the two channels (channel 1 (ch1) and channel 2 (ch2)) at times of interest (t_0, t_1, t_2 and t_3) shown with arrows in the normalized intensity subplot in **d**.

It is anticipated that the resulting intensity of the adduct, and hence the concentration, would be lower than observed in the first case (Fig. 6a). Indeed, the concentration of the adduct formed under these conditions, extracted from the intensity of channel 2, is measured at 0.035 M, representing approximately 70% of the total capacity (Fig. 6b). This method is equally applicable for the detection of adducts under dilute streams of CO_2. Figure 6c illustrates the data extracted from the operation of the microfluidic cell under dilute streams of 1% and 400 ppm (100% included for comparison). We observe the formation of 0.025 M of the BTMAPAQ$(CO_2)_2^{2-}$ adduct under the dilute condition of 0.01 bar CO_2 (1% CO_2, 99% N_2) within 50 min, detected in real time during the formation. This short timeframe (50 min) appears insufficient for any adduct to form under the 400 ppm condition. Moreover, the method is robust enough to be employed for the extraction of kinetic rates of adduct formation chemical reactions (Fig. 6d). To achieve this, we increased the imaging rate to subsecond intervals (125 ms) and conducted experiments using 1,5-BTMAPAQ and 1,8-BTMAPAQ isomers. Through CV analysis, we demonstrated a kinetic rate constant for the 1,5-BTMAPAQ isomer almost three times that of the 1,8-BTMAPAQ isomer (Supplementary Table 1). The in situ fast imaging of the adduct formation for the two isomers similarly reveals a threefold difference in kinetic rates.

Further incorporation of CO_2 sensors and flow meters into the negolyte reservoir's path would enable a direct comparison between the adduct concentration measured by the fluorescence microscope and the total captured capacity measured by the CO_2 sensor and the flow meter. Other possibilities include combining in situ fluorescence techniques with other in situ methods, such as Raman spectroscopy[28,29]. Moreover, establishing a rigorous correlation between intensity and concentration is crucial for enhancing the reliability and accuracy of quantification processes. Additionally, as the field advances in designing more stable compounds in oxygen environments, experiments can be conducted without interference from oxygen over longer durations. This method provides the capability to distinguish among the oxidized, reduced and adduct species and quantify their relative concentration with subsecond time resolution through their fluorescence signatures at single-digit micrometer resolution, demonstrating a highly promising technique for studying such systems. Furthermore, the method of conducting parallel monitoring of the fluorescence signatures of the species involved in a reaction is inspiring

https://doi.org/10.1038/s44286-024-00153-y

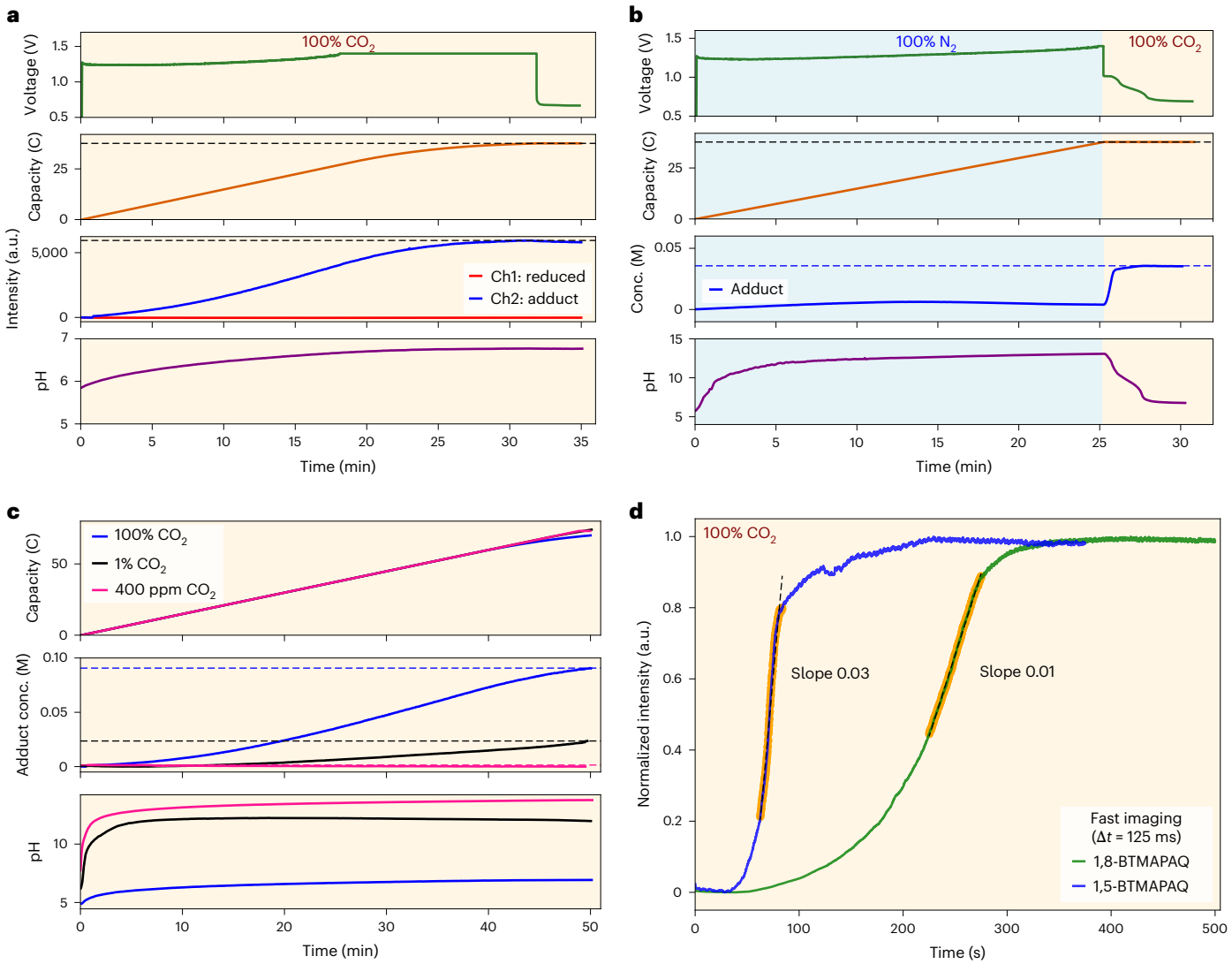

Fig. 6 | Information extracted from the operation of the microfluidic flow cell under a fluorescence microscope. The flow cell was operated under nitrogen and carbon dioxide streams, monitoring channels with excitation and absorption wavelengths of 488 and 594, respectively, in channel 1 (ch1) and 405 and 521, respectively, in channel 2 (ch2). Channel 1 wavelengths correspond to the reduced form concentration and channel 2 correspond to the adduct concentration. **a**, The voltage, capacity, in situ fluorescence intensity and pH of a solution of 5 mM 1,5-BTMAPAQ dissolved in 1 M KCl under a pure stream of CO_2. **b**, The voltage, capacity, concentration ((conc.) extracted from in situ fluorescence intensity) and pH of a solution of 5 mM 1,5-BTMAPAQ dissolved in 1 M KCl under a pure stream of CO_2. **c**, The capacity, adduct concentration and pH at three different CO_2 partial pressures mixed with nitrogen. The horizontal dashed lines in **a**–**c** represent the maximum concentration and intensity of the species observed during the experiments, providing a reference point for comparing the extent of adduct formation under varying conditions. **d**, The normalized intensity of adduct versus time measured with an increased imaging rate to subsecond intervals (125 ms) for two isomers of 1,5-BTMAPAQ and 1,8-BTMAPAQ.

for studying reaction mechanisms and concentration quantification in other systems.

Conclusions

In the present work, we began by providing a thermodynamic overview of the interplay between nucleophilicity swing and pH swing mechanisms as functions of the properties of a hypothetical quinone molecule, highlighting the importance of understanding the contribution of these mechanisms. We then proceeded to focus on the kinetic and thermodynamic properties of the BTMAPAQ isomers as a case study, revealing a strong thermodynamic tendency for BTMAPAQ to form a CO_2 adduct, although kinetically, this mechanism is predicted to be slower than the pH swing mechanism. We then proceeded to introduce two techniques for the experimental differentiation between the contributions of the pH swing mechanism and nucleophilicity swing mechanism. The first method was based on the voltage signature difference between the reduced and the adduct form of the quinone, conducted by incorporating an in situ reference electrode. In the second method, we introduced a noninvasive, in situ approach using fluorescence microscopy, providing the capability to isolate the contribution of the nucleophilicity mechanism through quinone adduct quantification. This technique holds promise for studying similar systems in detail, demonstrating a method for investigation of carbon capture processes.

Methods

Cyclic voltammetry measurements

For all three-electrode cyclic voltammetry experiments, a glassy carbon working electrode was used, accompanied by an Ag/AgCl reference electrode (sourced from BASi and presoaked in a 3 M KCl solution)

and a graphite counter electrode. The electrochemical measurements, including cyclic voltammetry and linear sweep voltammetry were performed using a Gamry Potentiostat.

Flow cell assembly with a reference electrode

Flow cell experiments utilized cell hardware sourced from Fuel Cell Tech and were configured into a zero-gap assembly. This setup incorporated POCO graphite flow plates, sealed with pyrolytic carbon, utilizing interdigitated flow fields for uniform distribution. Electrodes were constructed from a single layer of an AvCarb HCBA carbon cloth, each with a geometric surface area of 5 cm^2. Selemion DSV-N served as the chosen anion exchange membrane. In all experiments depicted in Fig. 3 utilizing the in situ reference electrode, we employed a gear pump for the negolyte, calibrated to a flow rate of 50 ml min^{-1}, and a peristaltic pump for the posolyte, optimized at 70 ml min^{-1}. The choice of a gear pump for the negolyte was based on our observations that, at these specific flow rates, the pulsation inherent to peristaltic pumps adversely affected the accuracy of the flow meter sensors. For the negolyte, a flow rate of 50 ml min^{-1} was found optimal due to the presence of the in situ reference electrode cell along its path, which has a smaller inlet diameter. A higher flow rate could potentially disturb the reference electrode setup. Consequently, the flow rates were optimized to ensure precise and stable operation. Electrochemical analysis was conducted using a Biologic SP-150e and Gamry Reference 3000 potentiostat setup. Electrolyte circulation was achieved with a Cole-Parmer Digital gear pump. Chemical reagents, including BTMAPFc and (ferrocenylmethyl)trimethylammonium chloride from TCI America, along with tetramethyl ammonium chloride and tetrabutylammonium chloride from Sigma–Aldrich, were employed as received, without additional purification.

For the reference electrode, a custom-made reference electrode holder was used to house an Hg/HgO reference electrode (BASi EF-1369) in the path of the electrolyte close to the inlet of the half cell. The reference electrode holder was designed with two small chambers separated by Selemion DSV-N. The chamber for the supporting electrolyte was filled with 1 M KCl, while the adjacent chamber was equipped with an inlet and outlet to allow for the flow of the battery electrolyte. Within the chamber containing the supporting electrolyte, the Hg/HgO reference electrode was submerged.

Flow cells were charged using the constant current followed by constant voltage method. Subsequently, the cells were placed in a resting state for a designated period to facilitate the completion of carbon capture. Following this, the cells were discharged and the battery was again put into a rest mode to allow for the release of CO_2. A continuous feed gas mixture, consisting of N_2 and CO_2, was directed through the anthraquinone electrolytes, maintaining a constant flow with predetermined partial pressures. The total flow rate was 11.76 ml min^{-1} for all tests except for the tests under dilute conditions of 1% CO_2 + 99% CO_2 where the flow rate was 23.52 ml min^{-1}. The FS4001 MEMS mass flow sensor and SprintIR CO_2 sensor (GC-0018) were used in our tests.

Ex situ UV–vis tests

UV–vis absorbance spectra were obtained with a DH-2000-BAL UV–visualization light source from Ocean Optics with optical fiber connectors, a quartz cuvette and a cuvette holder with inlet and outlet allowing for continuous flow of electrolyte. The cuvette holder was positioned before the inlet of the flow cell. The cuvette path length was 100 µm. All the absorbance spectra are blank corrected.

Ex situ fluorescence plate reader

A 5 ml solution of 0.1 M 1,5-BTMAPAQ (oxidized form) was first completely reduced against 15 ml of 0.2 M BTMAPFc in a flow battery inside a glovebox. Dry ice was then transferred inside the glovebox and added to the fully reduced solution to prepare the adduct form of 1,5-BTMAPAQ. Subsequently, 200 µl of each sample (oxidized, reduced and adduct) was loaded into separate wells of a Greiner microplate (96-well, polystyrene, flat-bottom, µclear, black, clear bottom) inside the glovebox. To prevent reoxidation due to the diffusion of atmospheric oxygen into the electrolytes, the microplate lid was sealed before taking the samples outside of the glovebox. The microplate was then transferred outside to a BioTek Synergy HT plate reader for photophysical experiments.

Microfluidic transparent flow cell

The microfluidic cell structure includes an anion exchange membrane (DSV-N) sandwiched between two 5 × 10 mm Avcarb190 porous carbon electrodes layered in pockets molded within polydimethylsiloxane (PDMS) half cells and two acrylic end plates for compression. The half-cell has a thickness of 8 mm, suitable for direct observation with a 10×/0.3 numerical aperture Leica objective (556503) with a working distance of 11 mm mounted on a confocal microscope (Leica DMi8 body with Andor dragonfly spinning disk). The unprecedented resulting transverse resolution for local electrochemical characterization in porous electrode with this objective was 1 µm per pixel and about 25 µm for the depth of field. Peristaltic pumps were employed for circulating the electrolyte, and the headspace on the negolyte side could be switched from N_2 to CO_2 during the experiments. Further information is provided in Supplementary Information.

In situ fluorescence tests

Fluorescence microscopy was performed using a Leica DMi8 microscope body with a Dragonfly spinning disk equipped with a Leica 10×/0.3 numerical aperture HC PL FLUOTAR lens. In all imaging experiments presented in this study, the following parameters were employed, unless specified otherwise: an exposure time of 2 s and an acquisition time of 2.5 s per frame. Two channels were configured with an excitation wavelength of 488 and an emission wavelength peaking at 594, as well as an excitation wavelength of 405 and an emission wavelength peaking at 521. Further information is provided in Supplementary Information.

Synthesis

Synthesis of BTMAPAQs. Into a 1 l Schlenk flask, previously flame dried, 40 mmol of dihydroxyanthraquinone, 88 mmol of anhydrous K_2CO_3 and 9.5 mmol of KI in 160 ml of anhydrous dimethylformamide were suspended. The mixture was stirred under nitrogen for 20 min before adding 88 mmol of 3-bromopropyl trimethylammonium bromide to the resulting dark mixture. This mixture was then sealed off from the air to exclude moisture and vigorously stirred at 100 °C for 16 h, leading to a brownish slurry. Once cooled, 150 ml of ethyl acetate was mixed into the slurry, stirred at room temperature for 30 min and then filtered to separate the brown solid. This washing step was repeated several times until the filtrate turned colorless. The solid was then dissolved in methanol, and this solution was filtered to eliminate insoluble inorganic salts. Subsequently, the filtrate was evaporated under reduced pressure to remove methanol, yielding a dark red solid. This solid was then dissolved in deionized water and passed through a preprepared anion exchange resin column to exchange bromide ions with chloride ions. The resulting dark red to bright yellow (depending on the concentration) solution was evaporated under reduced pressure to eliminate water and retrieve the red solid. This solid was redissolved in methanol and the saturated solution was gradually added to 200 ml of ethyl acetate to precipitate out the product. The resulting precipitates were filtered to obtain the final product as orange to yellow solids, with yields ranging from 85% to 95%.

Synthesis of 22PEAQ. Into a 100 ml pear-shaped flask, 5 g of 2-hydroxyanthraquinone (22.3 mmol) was introduced along with ethyl 2-bromopropionate (3.75 ml, 29 mmol, 1.3 equiv.) and 7.5 g of potassium carbonate (54 mmol, 2.4 equiv.). The mixture was stirred in 40 ml of dimethylformamide at 80 °C for 3 h, followed by vacuum filtration to

isolate the ester. The ester, without undergoing further purification, was then dispersed in a mixture of 30 ml water and 30 ml isopropanol, to which 7.5 g of potassium hydroxide (133 mmol, 16 equiv.) was added. This mixture was stirred at 80 °C for another 3 h and then precipitated using 1 M HCl to obtain a green solid. The process yielded 2.4 g of the product, representing a 52.9% yield.

Synthesis of D2PEAQ. First, 10 g of 2,6-dihydroxyanthraquinone (41.6 mmol) were combined with 15 g of potassium carbonate (108 mmol, 2.6 equiv.), 15 ml of methyl 2-bromopropionate (22.45 g, 134.4 mmol, 3.23 equiv.) and 30 ml of dimethylformamide. The mixture was stirred at 80 °C for 1 h, leading to the formation of three sandy yellow precipitates. Subsequently, 20 ml of water was introduced to rinse the flask, followed by vacuum filtration. The resulting solid, without undergoing any purification, was then dispersed in a mixture of 150 ml of 2-propanol and 150 ml of water, with the addition of 15 g of potassium hydroxide (267 mmol, 6.43 equiv.). This mixture was agitated at 80 °C for 3 h, after which 1.5 M hydrochloric acid was added gradually until a yellow precipitate formed. The final mixture was vacuum filtered to obtain a yellow solid, with a final yield of 9.15 g (57%).

Data availability

Further data supporting the findings of this study are provided in the Supplementary Information. All the source data for this article (both the main manuscript and the Supplementary Information) are available via GitHub at https://github.com/AzizGordonEchem/2024-09-QuCO2-NCE. Source data are provided with this paper.

Code availability

The code written for solving the set of equilibrium equations described in the Thermodynamic Overview section is available via GitHub at https://github.com/AzizGordonEchem/2024-09-QuCO2-NCE.

References

1. Bui, M. et al. Carbon capture anÿd storage (CCS): the way forward. *Energy Environ. Sci.* **11**, 1062–1176 (2018).
2. Rochelle, G. T. Amine scrubbing for CO_2 capture. *Science* **325**, 1652–1654 (2009).
3. Rochelle, G. T. Thermal degradation of amines for CO_2 capture. *Curr. Opin. Chem. Eng.* **1**, 183–190 (2012).
4. Diederichsen, K. M. et al. Electrochemical methods for carbon dioxide separations. *Nat. Rev. Methods Primers* **2**, 68 (2022).
5. Rheinhardt, J. H., Singh, P., Tarakeshwar, P. & Buttry, D. A. Electrochemical capture and release of carbon dioxide. *ACS Energy Lett.* **2**, 454–461 (2017).
6. Rahimi, M., Khurram, A., Hatton, T. A. & Gallant, B. Electrochemical carbon capture processes for mitigation of CO_2 emissions. *Chem. Soc. Rev.* **51**, 8676–8695 (2022).
7. Liu, Y., Ye, H. Z., Diederichsen, K. M., Van Voorhis, T. & Hatton, T. A. Electrochemically mediated carbon dioxide separation with quinone chemistry in salt-concentrated aqueous media. *Nat. Commun.* **11**, 2278 (2020).
8. Li, X., Zhao, X., Liu, Y., Hatton, T. A. & Liu, Y. Redox-tunable Lewis bases for electrochemical carbon dioxide capture. *Nat. Energy* **7**, 1065–1075 (2022).
9. Jin, S., Wu, M., Gordon, R. G., Aziz, M. J. & Kwabi, D. G. pH swing cycle for CO_2 capture electrochemically driven through proton-coupled electron transfer. *Energy Environ. Sci.* **13**, 3706–3722 (2020).
10. Jin, S., Wu, M., Jing, Y., Gordon, R. G. & Aziz, M. J. Low energy carbon capture via electrochemically induced pH swing with electrochemical rebalancing. *Nat. Commun.* **13**, 2140 (2022).
11. Gurkan, B., Simeon, F. & Hatton, T. A. Quinone reduction in ionic liquids for electrochemical CO_2 separation. *ACS Sustain. Chem. Eng.* **3**, 1394–1405 (2015).
12. Diederichsen, K. M., Liu, Y., Ozbek, N., Seo, H. & Hatton, T. A. Toward solvent-free continuous-flow electrochemically mediated carbon capture with high-concentration liquid quinone chemistry. *Joule* **6**, 221–239 (2022).
13. Barlow, J. M. & Yang, J. Y. Oxygen-stable electrochemical CO_2 capture and concentration with quinones using alcohol additives. *J. Am. Chem. Soc.* **144**, 14161–14169 (2022).
14. Voskian, S. & Hatton, T. A. Faradaic electro-swing reactive adsorption for CO_2 capture. *Energy Environ. Sci.* **12**, 3530–3547 (2019).
15. Wielend, D., Apaydin, D. H. & Sariciftci, N. S. Anthraquinone thin-film electrodes for reversible CO_2 capture and release. *J. Mater. Chem. A* **6**, 15095–15101 (2018).
16. Jing, Y. et al. Electrochemically induced CO_2 capture enabled by aqueous quinone flow chemistry. *ACS Energy Lett.* **9**, 3526–3535 (2024).
17. Liu, C. et al. CO_2 capture from flue gas using an electrochemically reversible hydroquinone/quinone solution. *Energy Fuels* **33**, 3380–3389 (2019).
18. Luo, L. et al. Regeneration of Na_2Q in an electrochemical CO_2 capture system. *Energy Fuels* **35**, 12260–12269 (2021).
19. Kerr, E. F. et al. High energy density aqueous flow battery utilizing extremely stable, branching-induced high-solubility anthraquinone near neutral pH. *ACS Energy Lett.* **8**, 600–607 (2022).
20. Kwabi, D. G., Ji, Y. & Aziz, M. J. Electrolyte lifetime in aqueous organic redox flow batteries: a critical review. *Chem. Rev.* **120**, 6467–6489 (2020).
21. Wu, M. et al. Highly stable, low redox potential quinone for aqueous flow batteries. *Batter. Supercaps* **5**, e202200009 (2022).
22. Rabindra, L. N. R. et al. The dissociation constants of carbonic acid in seawater at salinities 5 to 45 and temperatures 0 to 45 °C. *Mar. Chem.* **44**, 249–267 (1993).
23. Simeon, F. et al. Electrochemical and molecular assessment of quinones as CO_2-binding redox molecules for carbon capture. *J. Phys. Chem. C* **126**, 1389–1399 (2022).
24. Conway, W., Wang, X., Burns, R., McCann, N. & Maeder, M. Comprehensive study of the hydration and dehydration reactions of carbon dioxide inaqueous solution. *J. Phys. Chem. A* **114**, 1734–1740 (2009).
25. Zhao, E. W. et al. In situ NMR metrology reveals reaction mechanisms in redox flow batteries. *Nature* **579**, 224–228 (2020).
26. Amini, K. et al. Electrochemical performance of mixed redox-active organic molecules in redox flow batteries. *J. Electrochem. Soc.* **170**, 120535 (2023).
27. Amini, K. et al. An extremely stable, highly soluble monosubstituted anthraquinone for aqueous redox flow batteries. *Adv. Funct. Mater.* **33**, 2211338 (2023).
28. Lu, X. et al. In situ observation of the pH gradient near the gas diffusion electrode of CO_2 reduction in alkaline electrolyte. *J. Am. Chem. Soc.* **142**, 15438–15444 (2020).
29. Lamb, K. J. et al. Capacitance-assisted sustainable electrochemical carbon dioxide mineralisation. *ChemSusChem* **11**, 137–148 (2018).

Acknowledgements

This research was supported by the National Science Foundation through grant CBET-1914543 and by US Department of Energy award DE-AC05-76RL01830 through Pacific Northwest National Laboratory subcontract 654799. K.A. was supported in part through the Natural Sciences and Engineering Research Council of Canada Postdoctoral Fellowship program (application no. PDF-557232-2021). The authors also thank T. Rinberg, A. Bergman, E. Fell, T. George, K. Lee and M. Jin for valuable discussions.

Author contributions

M.J.A. and R.G.G. supervised the project. K.A. and M.J.A. conceived the idea. K.A. developed the thermodynamic model with input from Y.J. and D.X. M.S.E. implemented the code, and K.A. analyzed the data. Y.J. synthesized BTMAPAQ isomers. E.F.K. synthesized 22PEAQ and D2PEAQ compounds. K.A. conducted the CV tests on the BTMAPAQ isomers. J.D.S. developed and implemented the model for CV fittings. K.A. conducted in situ tests with the reference electrode and analyzed the data. K.A. and M.A. performed ex situ UV–vis tests and analyzed the data. K.A. carried out ex situ fluorescence plate reader tests. T.C. designed and built the transparent microfluidic flow cell. K.A. and T.C. performed the in situ fluorescence tests and analyzed the data. All authors contributed to the discussion. K.A. wrote the manuscript, with all co-authors contributing to the editing.

Competing interests

The authors declare no competing interests.

Additional information

Supplementary information The online version contains supplementary material available at https://doi.org/10.1038/s44286-024-00153-y.

Correspondence and requests for materials should be addressed to Michael J. Aziz.

Peer review information *Nature Chemical Engineering* thanks Yayuan Liu, Bingjun Xu and the other, anonymous, reviewer(s) for their contribution to the peer review of this work.

nature chemical engineering

Supplementary information

https://doi.org/10.1038/s44286-024-00153-y

In situ techniques for aqueous quinone-mediated electrochemical carbon capture and release

In the format provided by the authors and unedited

1

2

3

1. Equilibrium concentrations corresponding to the discussion in the "Thermodynamic Overview" Section

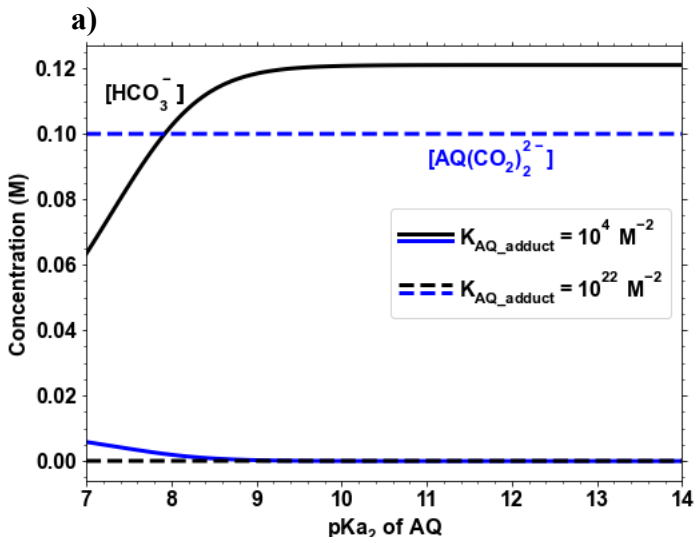

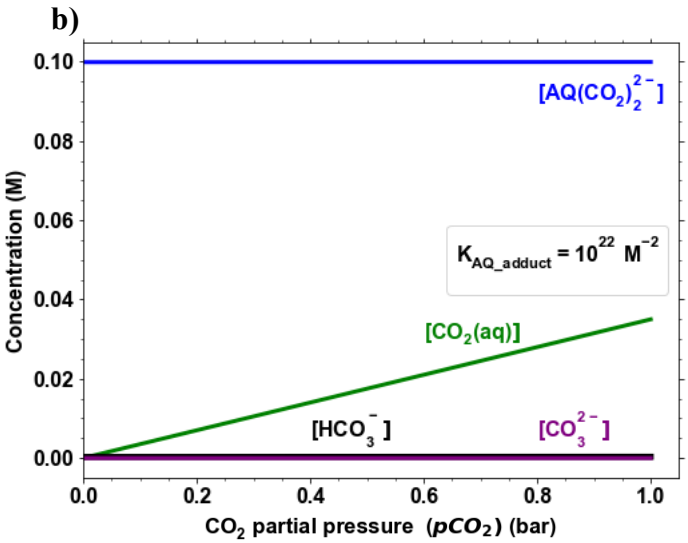

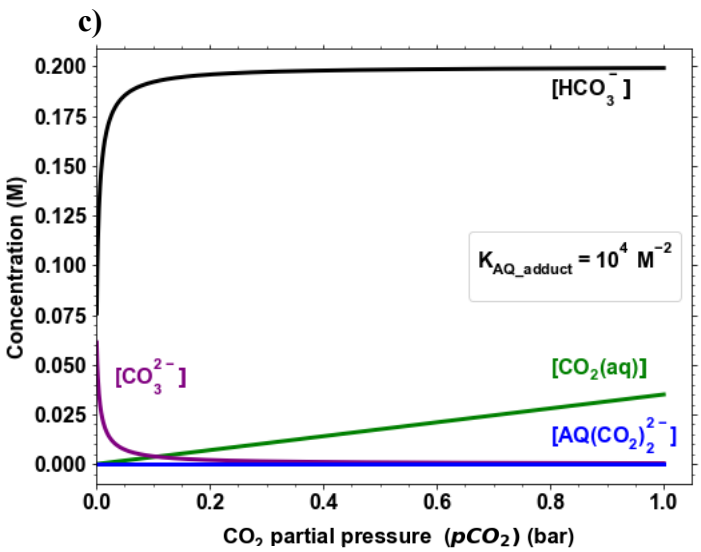

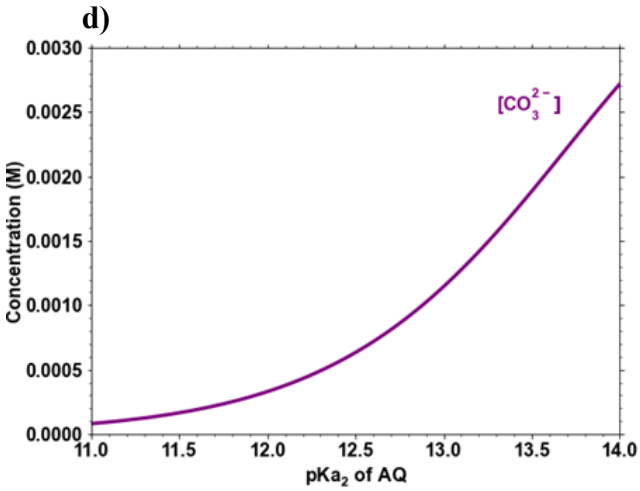

Figure S1 *(a) – (c): Equilibrium concentrations determined by solving the corresponding equilibrium equations described in the "Thermodynamic Overview" section. A total concentration of 0.1 M AQ with equilibrium constants* K_4, K_5, *and* K_w *at* $1.1 * 10^{-6}\ M$, $4.1 * 10^{-10}\ M$, *and* $10^{-14}\ M^2$ *,respectively, is assumed. a) Concentrations of* HCO_3^-, *and* $AQ(CO_2)_2{}^{2-}$ *at varying* pKa_2 *values of the AQ molecule and at two different* K_{AQ_adduct} *values. Here the* pKa_1 *is assumed to be 7. b) Concentrations of* AQ^{2-}, $AQ(CO_2)_2{}^{2-}$, AQ, AQH^- *at different partial pressures of* CO_2 *at a strong* K_{AQ_adduct} *of* $10^{22}\ M^{-2}$. *Here* pKa_1 *and* pKa_2 *values are set at 11 and 13, respectively. c) Concentrations of* HCO_3^-, CO_3^{2-}, $CO_2(aq)$, $AQ(CO_2)_2{}^{2-}$ *at different partial pressures of* CO_2 *and at a weak* K_{AQ_adduct} *of* $10^4\ M^{-2}$. *Here* pKa_1 *and* pKa_2 *values are set at 11 and 13, respectively. d) Zoomed-in figure of Figure 1b, demonstrating the increase in* $[CO_3^{2-}]$ *concentration with the increase in* pKa_2.

2. Understanding the Impact of Mechanisms on System Performance

In this section, we elucidate examples showing how each mechanism impacts critical performance metrics of the final system and explain why developing these systems as a "black box," without understanding the contributions of the underlying mechanisms, is inadequate. A comprehensive understanding of the nucleophilicity-swing and pH-swing mechanisms is essential for optimizing system performance in terms of capture capacity, energy requirements, stability, kinetic and reaction rates, and material choice:

1. **Capture Capacity:** The carbonate formation in the pH-swing route results in half the capture capacity compared to the bicarbonate and nucleophilicity-swing pathways. Our thermodynamic overview shows that this distinction is particularly relevant for cells engineered for direct air capture (DAC), where CO_2 partial pressure is low. Under these conditions, the carbonate pathway dominates, leading to a significant reduction in capture capacity if the pH-swing mechanism is prevalent. Conversely, if the nucleophilicity-swing mechanism is dominant, the capture capacity can be twice as high. Thus, understanding the contributions of each mechanism is important for estimating capture capacity, especially for DAC applications.

2. **Energy Requirements:** The energy requirements for driving each mechanism differ, affecting the final energetic cost of the designed system. The nucleophilicity-swing mechanism involves the formation of the AQ-CO_2 adduct, where CO_2 acts as an electron-withdrawing group. This increases the electron density around the quinone core and stabilizes the reduced AQ-CO_2 adduct. This stabilization effect makes the AQ-CO_2 adduct less likely to lose electrons (i.e., be oxidized), resulting in a more positive oxidation potential (BTMAPAQ case study with a strong binding constant shows this new oxidation peak). In contrast, AQH_2 (formed during the pH-swing mechanism) represents the fully reduced form of anthraquinone, having accepted two protons and two electrons. The reduction of AQ to AQH_2 lacks the stabilizing effect of an electron-withdrawing group like CO_2. Therefore, the oxidation potential for AQH_2 is less positive compared to the AQ-CO_2

adduct. From a thermodynamic energy requirement perspective (ignoring kinetic and real-world losses), in a system where the AQ-CO_2 mechanism is dominant, the energy requirement is expected to be higher due to the larger ΔE (change in potential). Thus, understanding the contributions of each mechanism is important for estimating the energetic cost of the designed system.

3. **Stability and System Lifetime:** The stability of the quinone molecules and the overall system is influenced by the contribution of each mechanism. For instance, in the nucleophilicity-swing mechanism, the degradation rate of the organic molecule AQ-CO_2, as opposed to AQH_2, needs to be studied. AQs have shown degradation pathways such as dimerization and anthrone formation, and thus, the lifetime of the cell would depend on the degradation rate of AQH_2 (for pH-swing) versus AQ-CO_2 (for nucleophilicity-swing). Quantifying the amount of AQ-CO_2 formed versus AQH_2, coupled with their respective degradation rates, would allow us to estimate the lifetime of the cell in terms of chemical degradation.

   Another important aspect of performance is the oxygen stability of the system, which depends on the contribution of each mechanism. As described in point 2 above, the formation of AQ-CO_2 results in a compound with a more positive oxidation peak. This closer oxidation peak of the AQ-CO_2 adduct to the oxygen redox potential reduces the thermodynamic tendency for oxidation by oxygen. As a result, the AQ-CO_2 adduct would be more oxygen-stable compared to AQH_2 (pH-swing mechanism) from a thermodynamic point of view. Thus, understanding the dominance and contribution of the nucleophilicity-swing mechanism versus the pH-swing mechanism allows us to make better predictions regarding oxygen stability.

4. **Kinetic and Reaction Rates:** Each mechanism exhibits different kinetic and reaction rates, which would affect the overall rate of CO_2 capture in the designed system. In our specific case study, we determined the individual kinetic rate constants for each mechanism, providing a range of kinetic rates (detailed in the SI Section 4). Understanding these kinetic differences allows us to optimize the system accordingly. For instance, if one mechanism is kinetically hindered compared to the other, we can modify the operational conditions or the AQ molecule itself to favor the faster mechanism. This understanding is thus important for maximizing the capture rates and overall performance under various conditions.

5. **Materials Choice for the System:** Understanding and quantifying the contribution of each mechanism will also affect the choice of materials for system engineering. For example, with the pH-swing mechanism, the formation of bicarbonate and carbonate ions introduces additional considerations for membrane selection. Bicarbonate and carbonate ions are smaller and less sterically hindered compared to AQ-CO_2 adducts, which can result in higher membrane crossover rates, especially with anion exchange membranes. This affects the choice of membrane materials, as more selective membranes are required to prevent ion crossover and maintain system efficiency.

Thus, the contributions and interplay between the nucleophilicity-swing and pH-swing mechanisms impact capture capacity, energy requirements, system stability, reaction kinetics, and material choices. When a new AQ molecule is designed, we need tools to gather information about the contributions of these two sub-mechanisms to better understand whether the material fits the specific scenario it has been designed for or if it needs further modification. As such, we believe that understanding the interplay between the above two mechanisms is critical in the material discovery cycle.

3. Examples of Strategies for Modifying Molecular Structure to Optimize Performance

These examples illustrate how structural modifications can be strategically employed to optimize molecular performance, steering the behavior toward desired mechanisms for specific applications: 1) **Electron-Donating or Withdrawing Groups**: Introducing electron-donating groups at positions on the molecule can increase the pKa by stabilizing the conjugate acid form without significantly increasing the electron density at the nucleophilic site, thus favoring the pH-swing mechanism. The incorporation of electron-withdrawing groups will lower the pKa of the reduced and protonated redox species, thus favoring the nucleophilicity-swing mechanism Bigot, Anna, et al. "Influence of substituent on spectroscopic and acid-base properties of anthraquinone derivatives." *Copernican Letters* 1 (2010): 51-56]. 2) **Steric Hindrance**: Utilizing steric effects by adding bulky substituents near the nucleophilic site to create steric hindrance can reduce the nucleophilicity of the site by making it less accessible for CO_2 binding, thereby making the pH-swing mechanism dominant. 3) **Solvent Effects**: Utilizing solvents or solvent mixtures that increase the pKa of the molecule by stabilizing the conjugate acid form through solvation effects without significantly enhancing nucleophilicity is another approach. In aprotic media, CO_2 will be captured via nucleophilicity-swing rather than pH-swing mechanism, as there will not be any proton sources [Barlow, Jeffrey M., and Jenny Y. Yang. "Oxygen-stable electrochemical CO2 capture and concentration with quinones using alcohol additives." *Journal of the American Chemical Society* 144.31 (2022): 14161-14169].

4. Information corresponding to the "Thermodynamic and Kinetic Analysis of BTMAP-AQ Isomers" Section

4.1 Cyclic voltammetry profiles of the BTMAP-AQ isomers under pure N_2 headspace at different scan rates

Detail of Experimental Procedure: For all three-electrode cyclic voltammetry experiments, a glassy carbon working electrode was used, accompanied by an Ag/AgCl reference electrode (sourced from BASi and pre-soaked in a 3 M KCl solution), and a graphite counter electrode. The three-electrode setup was placed and sealed inside a round-bottom flask with four outlets, and a tube was used to continuously purge with either CO_2 or N_2 gas into the solution. Before starting the experiment under each gas stream, the system was purged for at least 10 minutes to ensure saturation with the corresponding gas. Between each set of experiments, the working electrode was cleaned with a slurry of fine alumina and rinsed with water to ensure it was thoroughly cleaned. The reference electrode was periodically measured against a master reference electrode

for calibration. If the solution inside the reference electrode was low, it was replaced with 3 M KCl and pre-soaked in the same solution before use. The electrochemical measurements, including cyclic voltammetry and linear sweep voltammetry, were performed using a Gamry Potentiostat.

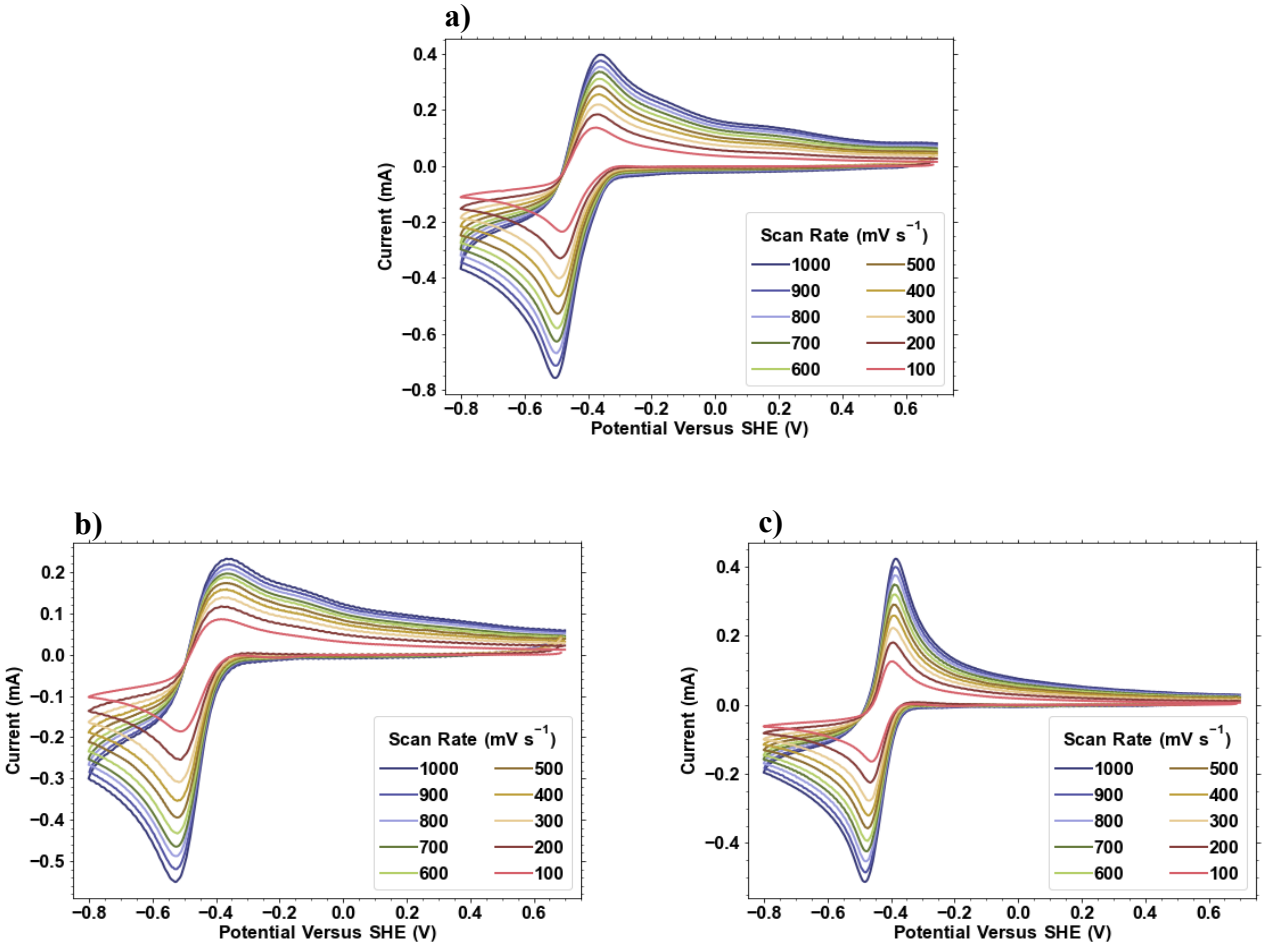

Figure S2 *Cyclic voltammetry profiles of 5 mM of a) 1,4-BTMAP-AQ, b) 1,5-BTMAP-AQ* and c) *1,8-BTMAP-AQ dissolved in 1 M KCl under a pure N_2 headspace at different scan rates between 100 mV/s to 1000 mV/s.*

The CVs under nitrogen show a broader peak for the 1,4 and 1,5 BTMAPAQ isomers compared to the 1,8 BTMAPAQ isomer. This peak broadening can be attributed to structural and steric effects. The positions of the substituent chains on the anthraquinone ring differ significantly among these three isomers, resulting in varying degrees of steric hindrance. This steric hindrance can impede efficient packing and interaction with the electrode surface, leading to broader oxidation peaks in the CV profiles of the different isomers. Similar observations of steric hindrance affecting electrochemical behavior have been reported in the literature [Daasbjerg, Kim, Steen U. Pedersen, and Henning Lund. "Electrochemical measurements of rate constants for the electron transfer reaction to sterically hindered alkyl halides." *Acta Chem. Scand. B* 43 (1989): 876-881][Duffin,

Thorin J., et al. "Direct measurement of the local field within alkyl-ferrocenyl-alkanethiolate monolayers: Importance of the supramolecular and electronic structure on the voltammetric response and potential profile." *Electrochimica Acta* 311 (2019): 92-102.]. Although this is beyond the scope of our present work, we believe that understanding the relationship between steric effects and the electrochemical behavior of isomers is an interesting question for future research.

Note that a small shoulder peak can be observed around 0.2 V vs. SHE in the CVs of 1,4-BTMAPAQ and 1,5-BTMAPAQ (especially 1,4-BTMAPAQ) at high scan rates (see Figure S2). We believe this is due to residual CO_2 impurity from prior experiments or impurities in the nitrogen gas. This peak is nonsignificant at low scan rates and appears slightly at high scan rates. Given that 1,4-BTMAPAQ has the fastest kinetic rate constant of binding with CO_2 (see table S1), this can show up as a small shoulder if residual CO_2 exists and at high scan rates, where the peak is more pronounced based on the Randles-Sevcik equation.

4.2 Calculation of K_{AQ_adduct} from the CV result

The K_{AQ_adduct} is calculated with the following equation:

$$K_{AQ\_adduct} = \exp\left(\frac{nF}{RT}\left(E^{0\prime}_{AQ_{adduct}} - E^{0\prime}\right)\right) \quad \text{(S1)}$$

where n is the number of transferred electrons, F is the Faraday's constant, R is the gas constant, T is the temperature and $E^{0\prime}_{AQ\_adduct}$ and E'^0 are the half-wave redox potential for the $AQ(CO_2)_2^{2-}$ adduct redox reaction and the AQ^{2-} redox reaction, respectively. Below, the derivation of this equation is provided.

We are interested in finding the equilibrium constant for the $AQ(CO_2)_2^{2-}$ adduct formation reaction:

$$AQ^{2-} + 2\ CO_2 \rightleftharpoons AQ(CO_2)_2^{2-} \qquad K_{AQ\_adduct} = = \frac{[AQ(CO2)2^{2-}]}{[AQ^{2-}][CO_2]^2} \quad \text{(S2)}$$

This equilibrium constant can be calculated from the two equilibrium constants shown below:

$$AQ + 2\ e^- \rightleftharpoons AQ^{2-} \qquad E^0\ ,\ K_{r1} = \frac{[AQ^{2-}]}{[AQ]} \quad \text{(S3)}$$

$$AQ + 2\ CO_2 + 2\ e^- \rightleftharpoons AQ(CO_2)_2^{2-} \quad E^0_{AQ\_adduct}\ ,\ K_{r2} = \frac{[AQ(CO2)2^{2-}]}{[AQ][CO_2]^2} \quad \text{(S4)}$$

Comparing (S3) and (S4) with (S2), we find:

$$K_{AQ\_adduct} = \frac{K_{r2}}{K_{r1}} \quad \text{(S5)}$$

Now, from the redox potentials we can write:

$$E = E^0 = \frac{-\Delta G^0}{nF} = \frac{RT}{nF} lnK_{r1} \qquad \text{(S6)}$$

$$E_{AQ\_adduct} = E^0_{AQ\_adduct} = \frac{-\Delta G^0}{nF} = \frac{RT}{nF} lnK_{r2} \quad \text{(S7)}$$

Reordering equations (S6) and (S7) in terms of K_{r1} and K_{r2} we find:

$$K_{r1} = \exp\left(\frac{nF}{RT}E^0\right) \quad \text{(S8)}$$

$$K_{r2} = \exp\left(\frac{nF}{RT}E^0_{AQ\_adduct}\right) \quad \text{(S9)}$$

Thus, K_{AQ_adduct} can thus be calculated as follows:

$$K_{AQ\_adduct} = \exp\left(\frac{nF}{RT}(E^0_{AQ\_adduct} - E^0)\right) \quad \text{(S10)}$$

Employing Equation (S10) (which is identical to S1) for calculation of the K_{AQ_adduct} for 1,4-BTMAP-AQ is shown below. The procedure for calculation of this equation for the other two isomers are identical.

As shown in Figure S3, the E^0 , half-wave potential for the AQ redox reaction would be $E^0 = \frac{(-0.361)+(-0.489)}{2} = -0.425$. For $AQ(CO_2)_2^{2-}$, the oxidation peak is at 0.25 V vs. SHE. Assuming a reversible redox reaction (59 mV potential separation between the oxidation and reduction peak potentials), a reduction peak would be at 0.191 mV vs. SHE. Thus, the half-wave potential for the $AQ(CO_2)_2^{2-}$ redox reaction would be $E^0_{AQ\_adduct} = \frac{(0.250)+(0.191)}{2} = 0.220$. Using equation (S10) with n=2, F = 96485 C/mol, R at 8.314 $\frac{J}{K\,M}$ and T at 293 K, K_{AQ_adduct} for 1,4-BTMAP-AQ isomer is $1.55 * 10^{22}\ M^{-2}$.

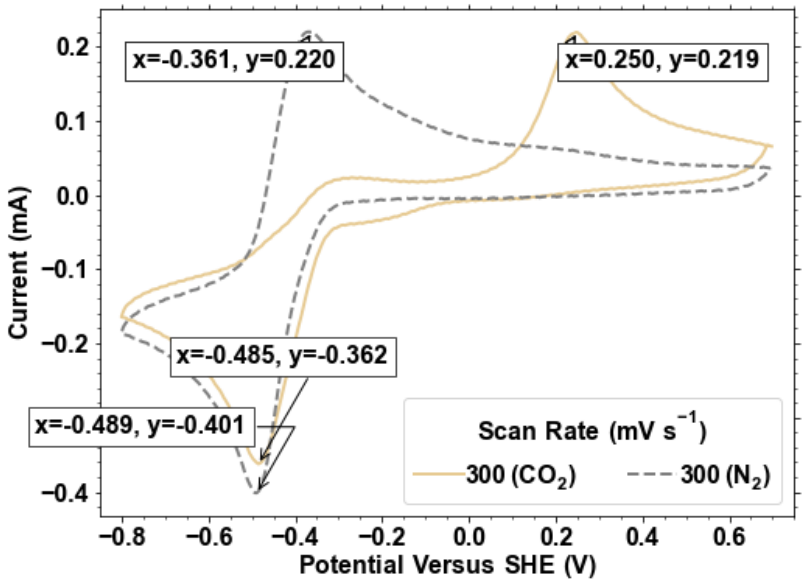

Figure S3 *Cyclic voltammetry profiles of 5 mM of 1,4-BTMAP-AQ dissolved in 1 M KCl at a scan rate of 300 mV/ s under pure N_2 and pure CO_2 headspace.*

4.3 Reaction scheme used for fitting the experimental CV data

In order to quantify the kinetic rates associated with the $AQ(CO_2)_2^{2-}$ adduct formation reaction, we assume the following three-step electrochemical-chemical-electrochemical (ECE) reaction scheme:

- $AQ + 2\ e^- \leftrightarrow AQ^{2-}$ (S11)
- $AQ^{2-} + 2\ CO_2 \rightarrow AQ(CO_2)_2^{2-}$ (S12)
- $AQ(CO_2)_2^{2-} \leftrightarrow AQ + 2\ CO_2 + 2\ e^-$ (S13)

Note that, reaction (S13) can be written in two steps:

- $AQ(CO_2)_2^{2-} \leftrightarrow AQ(CO_2)_2 + 2\ e^-$ (S14)
- $AQ(CO_2)_2 \rightarrow AQ + 2\ CO_2$ (S15)

However, in all the CV diagrams, we do not observe a reduction peak close to the oxidation peak of the $AQ(CO_2)_2^{2-}$ adduct, although the CV profiles are taken immediately after one another. This observation suggests that the reaction S15 is extremely fast, so that the CO_2 is liberated before we can detect a reduction peak for the $AQ(CO_2)_2^{2-}$ adduct. As such, reaction S13 and S14 are written as their sum in a concerted format: $AQ(CO_2)_2^{2-} \rightarrow AQ + 2\ CO_2 + 2\ e^-$. The reversible AQ redox reaction occurs at $E_1^{o\prime}$ formal potential with an electrochemical rate constant of k_0. The chemical quinone-adduct formation reaction occurs at a chemical rate constant of k_c and in presence of excess CO_2, which would result in $AQ(CO_2)_2^{2-}$ species with an assigned redox reaction occurring at $E_2^{o\prime}$ formal potential and with k'_0 electrochemical rate constant. A couple of points are important regarding this scheme. Firstly, the AQ redox reaction (reaction (S11)) unfolds in two single electron steps, as detailed in Section 4.4 in the SI. However, these two steps occur with less than 30 mV separation (see Section 4.4 in the SI and Figure S4), leading to a single merged peak in the cyclic voltammogram profile, and thus, the assumption is made that reaction (11) proceeds in one two-electron step. Similarly, reaction (S14) may occur in two sequential steps but based on the shape of the merged peaks in the CV profile, these sequential steps must occur with small potential separations. The final important note is that the assumption of excess CO_2 is justified in our experimental design; the CV is conducted under continuous flow of pure stream of CO_2 bubbled at high flow rate through the solution. Based on solubility of CO_2 in water under 1 bar, 0.035 M should dissolve under this partial pressure. The AQ concentration in the CVs is 0.005 M and is of course not replenished. Thus, the concentration of CO_2 is at least 7 times higher than AQ, and stochiometric-wise it is 3.5 times higher. Additionally, the high flow rate bubbled inside the solution would ensure negligible mass transfer issues.

4.4 Comparing CV Simulations: Single-Step vs. Two-Step Electron Transfer

To compare the case with single-step two-electron transfer reactions and the case where the anthraquinone undergoes two distinct single-electron transfers, simulations are performed considering these distinct electron transfers:

$$\frac{dC_{ox}(x,t)}{dt} = D_{ox}\frac{d^2C_{ox}(x,t)}{dx^2}$$

$$\frac{dC_{red1}(x,t)}{dt} = D_{red1}\frac{d^2C_{red1}(x,t)}{dx^2}$$

$$\frac{dC_{red2}(x,t)}{dt} = D_{red2}\frac{d^2C_{red2}(x,t)}{dx^2}$$

Where $C_{ox}, C_{red1}, C_{red2}$ represent concentrations of the completely oxidized, singly reduced and doubly reduced anthraquinones in mol/cm^3; t represents time in seconds; x represents space in cm; D_j represents the diffusion coefficient of species,j, in cm^2/s.

Initial conditions are:

$$C_{red1}(x, t = 0) = C_{red2}(x, t = 0) = 0, C_{ox}(x, t = 0) = 5\ mM$$

The boundary conditions at the electrode surface ($x = 0$) for the case of the rate of diffusion matching the rate of electrochemical reaction are:

$$-D_{ox}\frac{\mathrm{dC_{ox}(x = 0,\ t)}}{\mathrm{dx}} = \mathrm{i_1/AF}$$

$$-D_{red1}\frac{\mathrm{dC_{red1}(x = 0,\ t)}}{\mathrm{dx}} = \mathrm{(i_2 - i_1)/AF}$$

$$-D_{red2}\frac{\mathrm{dC_{red2}(x = 0,\ t)}}{\mathrm{dx}} = \mathrm{-i_2/AF}$$

A is the surface area of the electrode in cm^2, F is Faraday's constant (96,485 C/mol), and i is the current in A from a Faradaic reaction, where the two considered reactions are described below:

$$\frac{i_1}{AF} = k_0(-C_{ox}(x = 0, t)\mathrm{e}^{-\frac{\alpha_1 F}{RT}(E - E_1^{o\prime})} + C_{red1}(x = 0, t)\mathrm{e}^{\frac{(1-\alpha_1)F}{RT}(E - E_1^{o\prime})})$$

$$\frac{i_2}{AF} = k_0{}'(-C_{red1}(x = 0, t)\mathrm{e}^{-\frac{\alpha_2 F}{RT}(E - E_2^{o\prime})} + C_{red2}(x = 0, t)\mathrm{e}^{\frac{(1-\alpha_2)F}{RT}(E - E_2^{o\prime})})$$

Here, $k_0, \alpha_1, E_1^{0\prime}$ represent the kinetic rate constant (cm/s), electron transfer coefficient, and reduction potential (V) for the first reduction of the anthraquinone, and $k_0', \alpha_2, E_2^{0\prime}$ represent the kinetic rate constant, electron transfer coefficient, and reduction potential for the second reduction of the anthraquinone. R is the universal gas constant; T is temperature in Kelvin; and E is the electrode potential in volts. As shown in Figure S4, considering $E_2^{0\prime}$ to be 60 mV more negative than $E_1^{0\prime}$ causes the current profile to be much thicker than the experiment shows, whereas assuming no separation between the first and second reduction leads to a thin reduction peak, very similar to the experiment. Additionally, when allowing the peak separation to be varied for optimizations, the optimizer never allowed for a peak separation greater than 30 mV, even at extremely high kinetic rate constants of 0.1 cm/s, which was used in Figure S4.

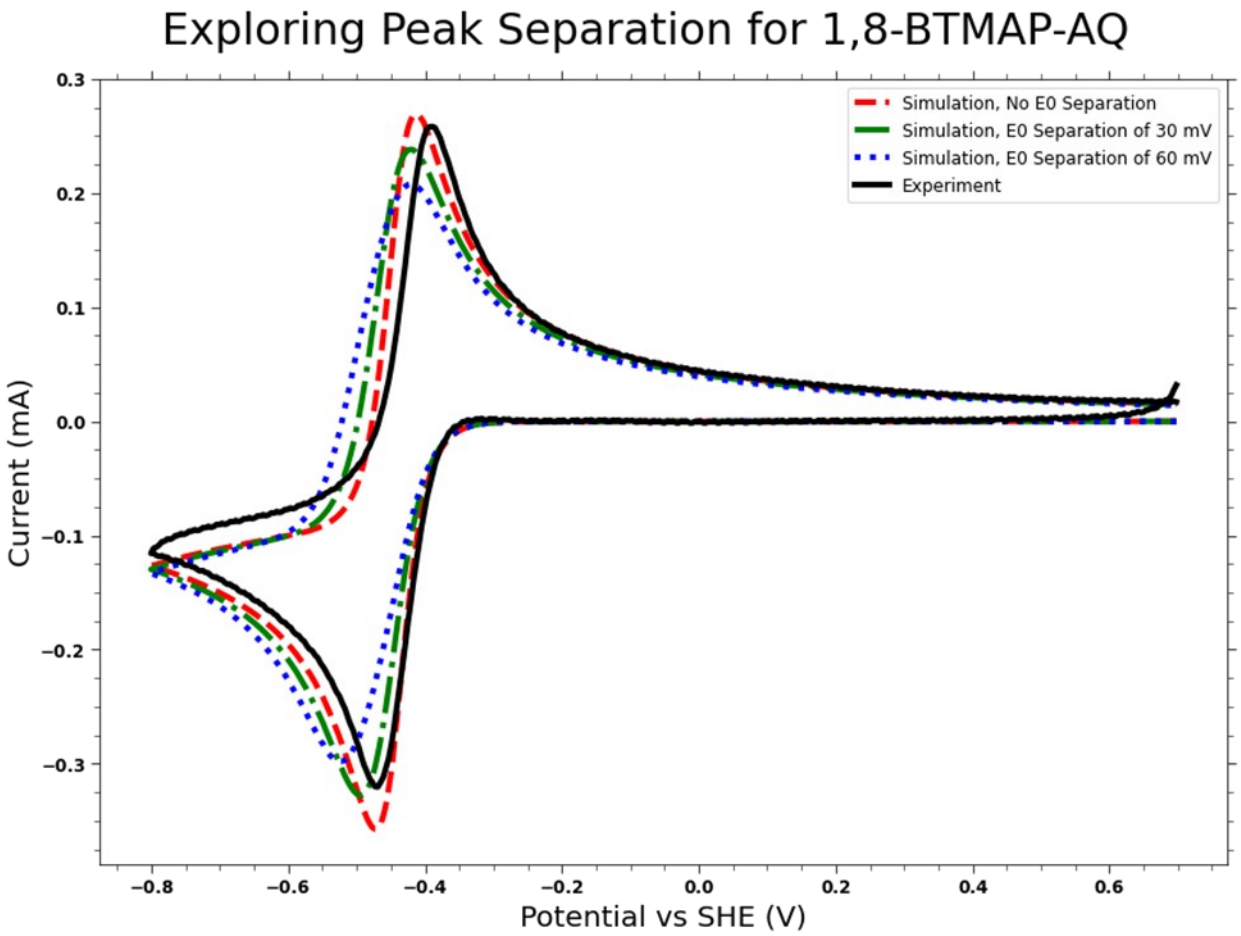

Figure S4: *Simulations of two distinct single-electron transfers using the diffusion coefficient, and electron transfer coefficient for the oxidized and reduced species from rotating disc electrode experiments and experimental data for cyclic voltammograms of 1,8-BTMAP-AQ at 0.4 V/s. Kinetic rate constants are increased to 0.1 cm/s to attempt to minimize widths of the current peaks, but even at those high values, the simulations show peak widths higher than the experimental data. The electrode area is 0.196 cm^2.*

4.5 Electrochemical-Chemical-Electrochemical (ECE) mechanism model (following the explanation in Section 4.3)

Having shown the reduction potentials are very close together, a simplified model for fitting to the data is used. The model for the ECE mechanism with two electrons transferred per electrochemical reaction uses the following mass conservation equations in one spatial dimension:

$$\frac{dC_{ox}(x,t)}{dt} = D_{ox}\frac{d^2C_{ox}(x,t)}{dx^2}$$

$$\frac{dC_{red}(x,t)}{dt} = D_{red}\frac{d^2C_{red}(x,t)}{dx^2} - \mathrm{k_c C_{red}(x,t)}$$

$$\frac{dC_{add}(x,t)}{dt} = D_{add}\frac{d^2C_{add}(x,t)}{dx^2} + \mathrm{k_c C_{red}(x,t)}$$

C represents concentration in mol/cm^3; subscripts ox, red, add stand for oxidized, reduced and adduct species, respectively; and k_c represents the chemical reaction rate for conversion of the reduced species to the adduct species.

Initial conditions are:

$$C_{red}(x, t = 0) = C_{add}(x, t = 0) = 0, C_{ox}(x, t = 0) = 5\ mM$$

The boundary conditions at the electrode surface for the case of the rate of diffusion matching the rate of electrochemical reaction are:

$$-D_{ox}\frac{\mathrm{dC_{ox}(x=0,\ t)}}{\mathrm{dx}} = \mathrm{i_1/nAF} = \frac{\mathrm{D_{red}dC_{red}(x=0,t)}}{\mathrm{dx}}$$

$$-D_{add}\frac{\mathrm{dC_{add}(x=0,\ t)}}{\mathrm{dx}} = \mathrm{i_2/nAF}$$

Where D is the diffusion coefficient in cm^2/s, n is the number of electrons transferred per electrochemical reaction, A is the surface area of the electrode in cm^2(*0.196 cm^2*), F is Faraday's constant (96,485 C/mol), and i is the current in A from a Faradaic reaction, where the two considered reactions are described below:

$$\frac{i_1}{nAF} = k_0(-C_{ox}(x=0,t)\mathrm{e}^{-\frac{\alpha_1 nF}{RT}(E-E_1^{o\prime})} + C_{red}(x=0,t)\mathrm{e}^{\frac{(1-\alpha_1)nF}{RT}(E-E_1^{o\prime})})$$

$$\frac{i_2}{nAF} = \quad k_0{}'C_{add}(x=0,t)\mathrm{e}^{\frac{(1-\alpha_2)nF}{RT}(E-E_2^{o\prime})}$$

Where k_0 and $k_0{}'$ are the kinetic rate constants of the first and the second electrochemical reactions in the ECE reaction scheme, respectively, in cm/s; α is the electron transfer coefficient for a given reaction; and $E^{0\prime}$ is the reduction potential in volts for a given reaction. The second electrochemical reaction occurs with no backward reaction (reduction) because any generated product is immediately consumed through an irreversible chemical reaction, as illustrated in reaction schemes S13-15 in Section 4.3 in the SI, which is supported by our cyclic voltammetry data.

The mass conservation equations are written using a centered difference scheme and explicit method for time stepping. The time steps are set by the number of data points in the experiment, and the differential spatial step is calculated so the time step is smaller than the diffusive timescale. For cases where the relative tolerance of 2% is not met, we add more data points by averaging between points in the original data set to allow for finer time resolution. Simulations within the relative tolerance of 2% are not visually distinguishable from each other in their current profiles. The simulations are fit to experimental data using Python's lmfit package. Before any analysis is done, current profiles from a solution with no redox active species are subtracted from the data to remove any capacitive current. Since reference electrode potentials can vary slightly, before performing fitting, the reduction potential is calculated from a single scan for a given molecule by

averaging the potentials for the reduction peak and first oxidation peak. From there, a least-squares fit between the current profiles from experiments in a N_2 environment and simulations is performed to obtain the diffusion coefficient, kinetic rate constant, and electron transfer coefficient of the oxidized and reduced species. After performing fits for each scan rate, the parameters that give the lowest error for the current profile are used to simulate cyclic voltammetry for each scan rate. From there, the diffusion coefficient, kinetic rate constant, chemical rate constant, electron transfer coefficient, and reduction potential of the adduct species are fit from the data taken with CO_2 in the atmosphere. Since the adduct species has a different molecular structure than the original reduced/oxidized species, we allow the adduct species to have a different diffusion coefficient than the reduced/oxidized species. This procedure is outlined below:

0. Subtract current profiles from blank electrolytes (only supporting solution) from the current profiles for each BTMAP-AQ experiment. Calculate the reduction potential, $E_1^{0\prime}$, using the average potential between the peak reduction current and first peak oxidation current for one scan rate in each BTMAP-AQ experiment.
1. Fit the simulation with the chemical rate constant set to 0 s^{-1} to experiments taken under a N_2 atmosphere to calculate $k_0, \alpha_1,$ and D_O. We assume $D_O = D_R$, but our simulator doesn't require it. The fitting procedure is:
    a. Perform a least-squares fit to the data using lmfit's minimize function for each scan rate, and then use the parameters from the fit that gave the lowest error across the scan. Simulate with these parameters for every scan rate.
2. Fit the simulation to experiments taken with CO_2 in the atmosphere to calculate $k_0', E_2^{0\prime}, \alpha_2, D_{add}$ and k_c using the procedure in Step 1.a.

The simulations and their matches to experiments are given below in Figures S5-S8:

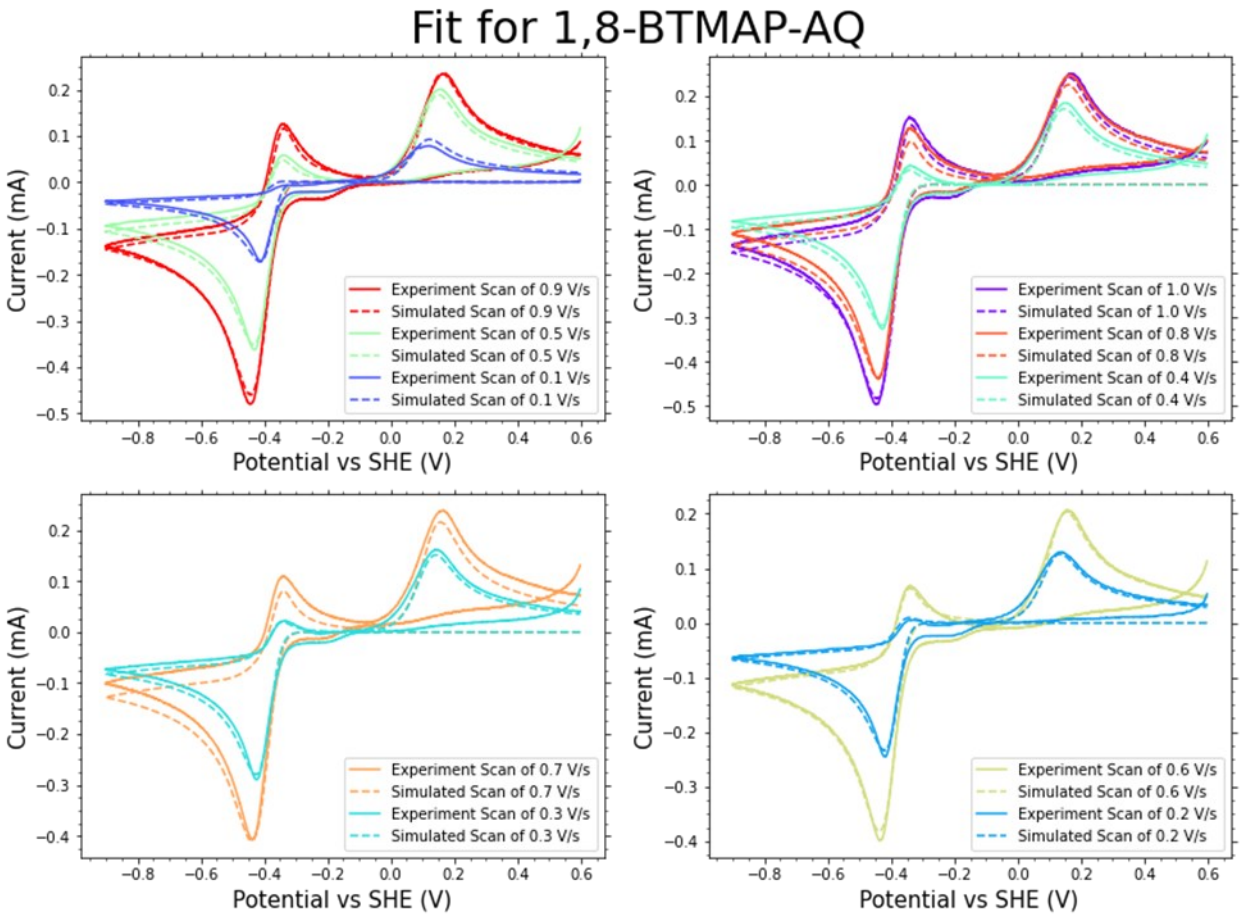

Figure S5: *Simulations and experimental data for cyclic voltammograms of 1,8-BTMAP-AQ. Parameter values are outlined in Table 1.*

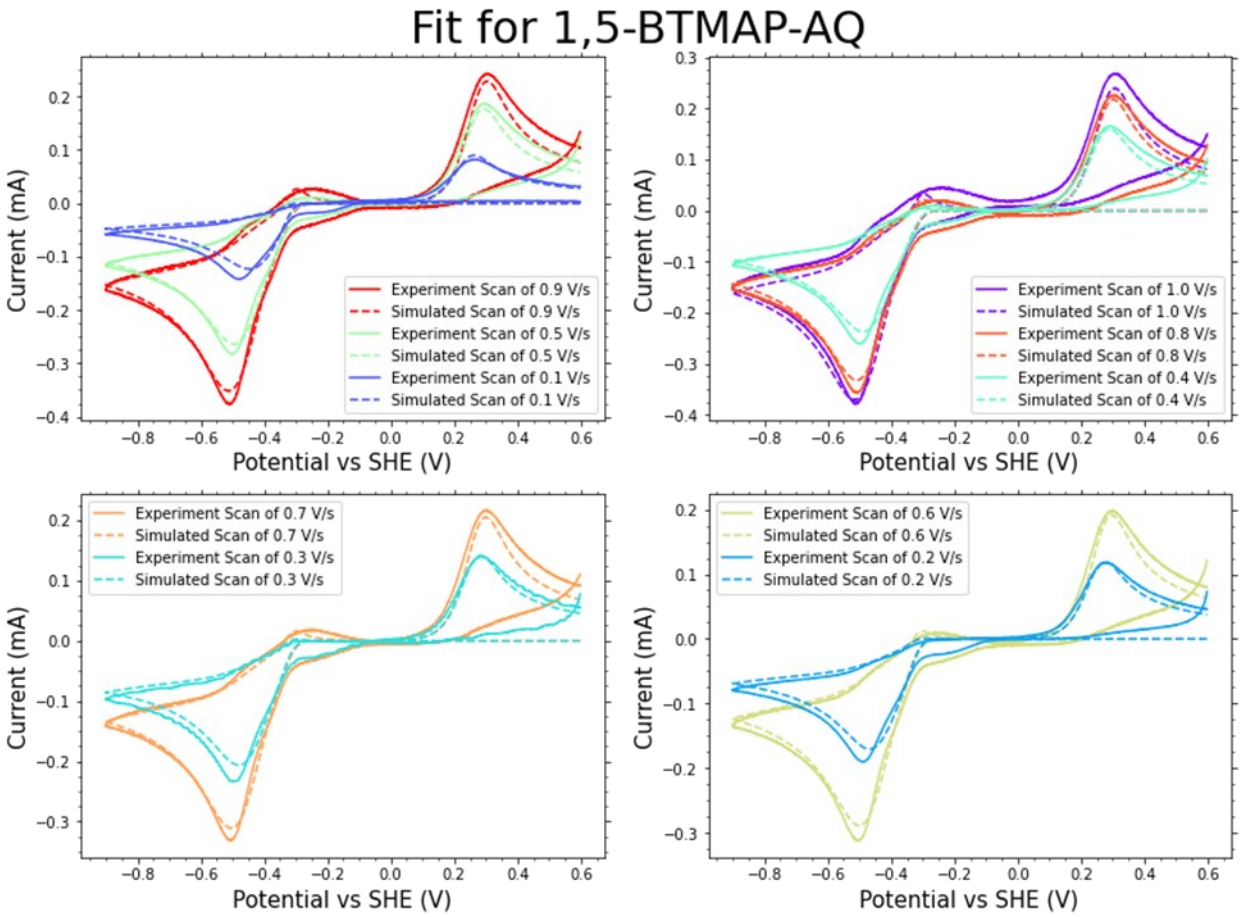

Figure S6: *Simulations and experimental data for cyclic voltammograms of 1,5-BTMAP-AQ. Parameter values are outlined in Table 1.*

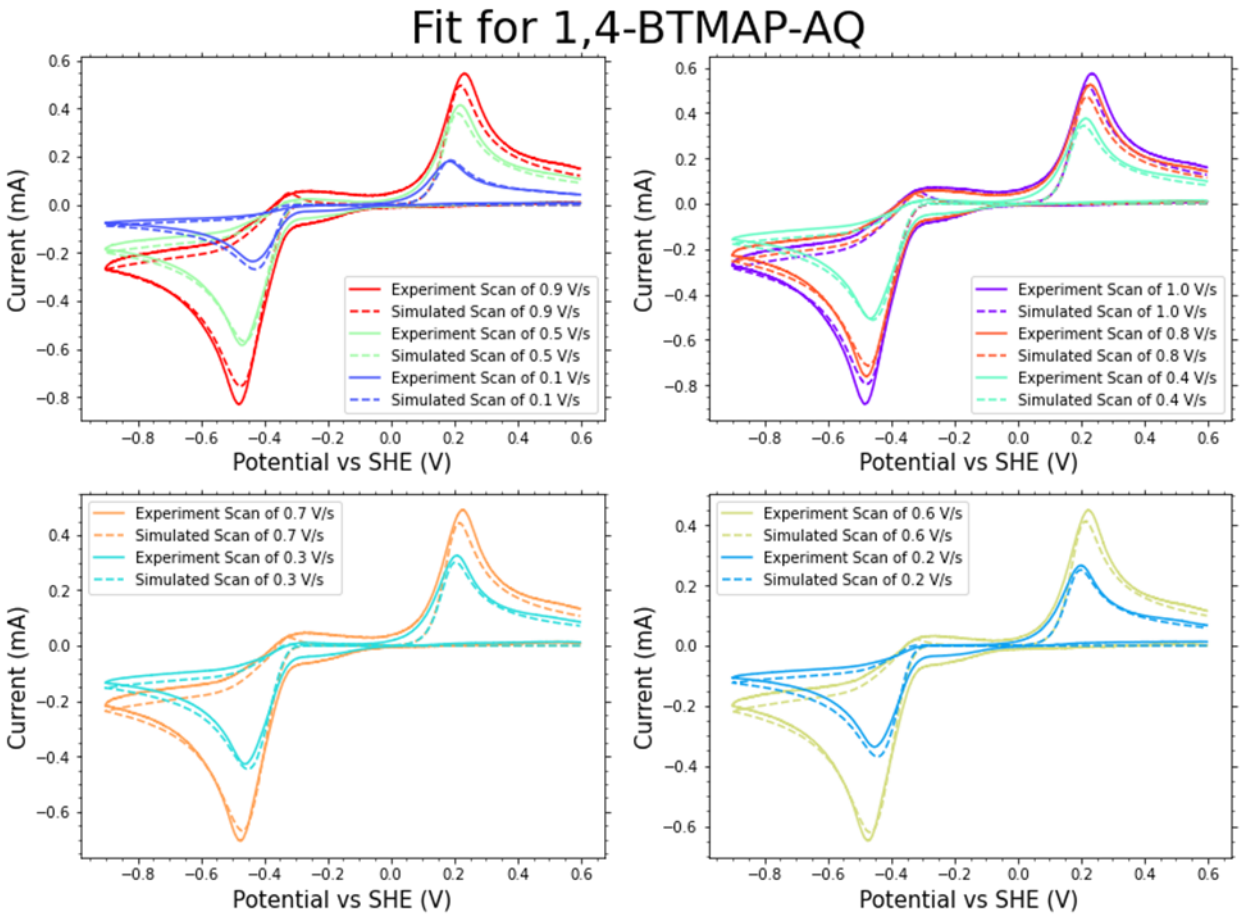

Figure S7: *Simulations and experimental data for cyclic voltammograms of 1,4-BTMAP-AQ. Parameter values are outlined in Table 1.*

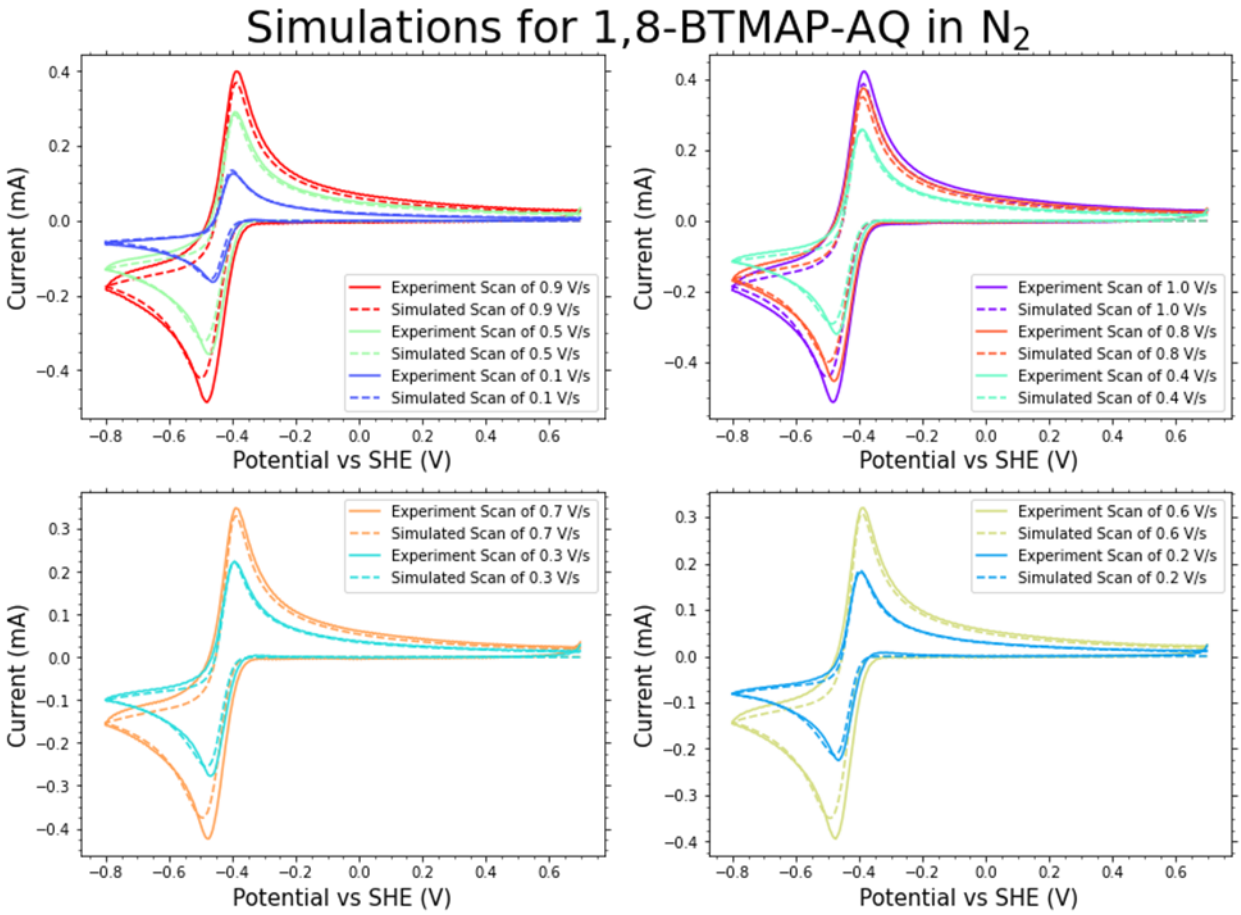

Figure S8: *Simulations and experimental data for cyclic voltammograms of 1,8-BTMAP-AQ in a N_2 environment, using the same parameters used in the environment with CO_2 but with the chemical rate constant set to 0 s^{-1}, showing the same behavior for the non-adduct species in both environments.*

It is important to note that the properties of the AQ redox reaction (reaction (12)), such as its electrochemical reaction rate constant and diffusion coefficient can be extracted in isolation under nitrogen environment. Figures S9-S11 show the properties extracted from rotating disk electrode tests under a nitrogen environment for all the isomers. The fitting parameters achieved for AQ under CO_2 are close to the range of the extracted properties of AQ in isolation under a nitrogen environment.

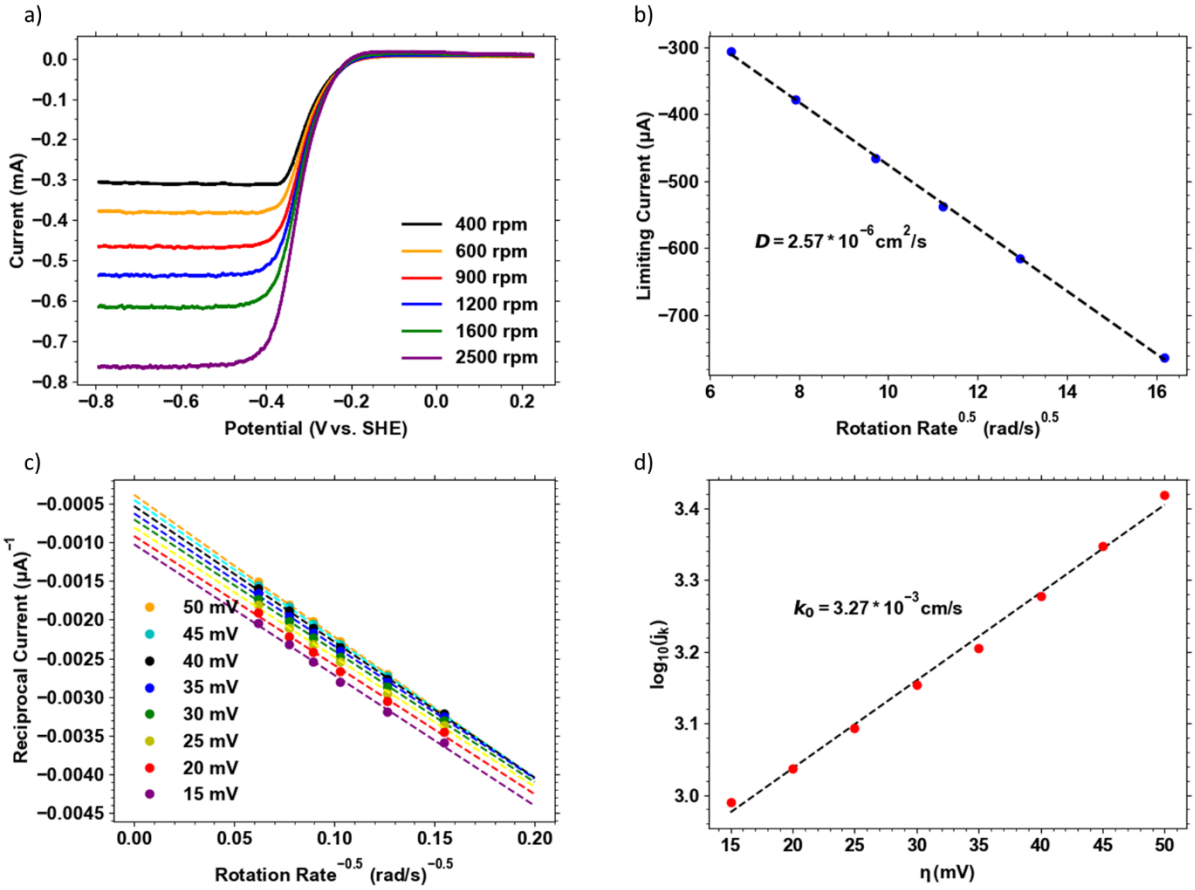

Figure S9 *Rotating disk electrode tests using 5 mM 1,4-BTMAP-AQ dissolved in 1 M KCl under nitrogen headspace. a) Linear sweep voltammograms on a glassy carbon rotating disk electrode at rotation rates between 400 and 2500 rpm with potential sweeping rate of 20 mV s^{-1}. b) Levich plot of limiting current versus square root of rotation rate. c) Koutecký–Levich plot at different overpotentials. (d) Fitted Tafel plot.*

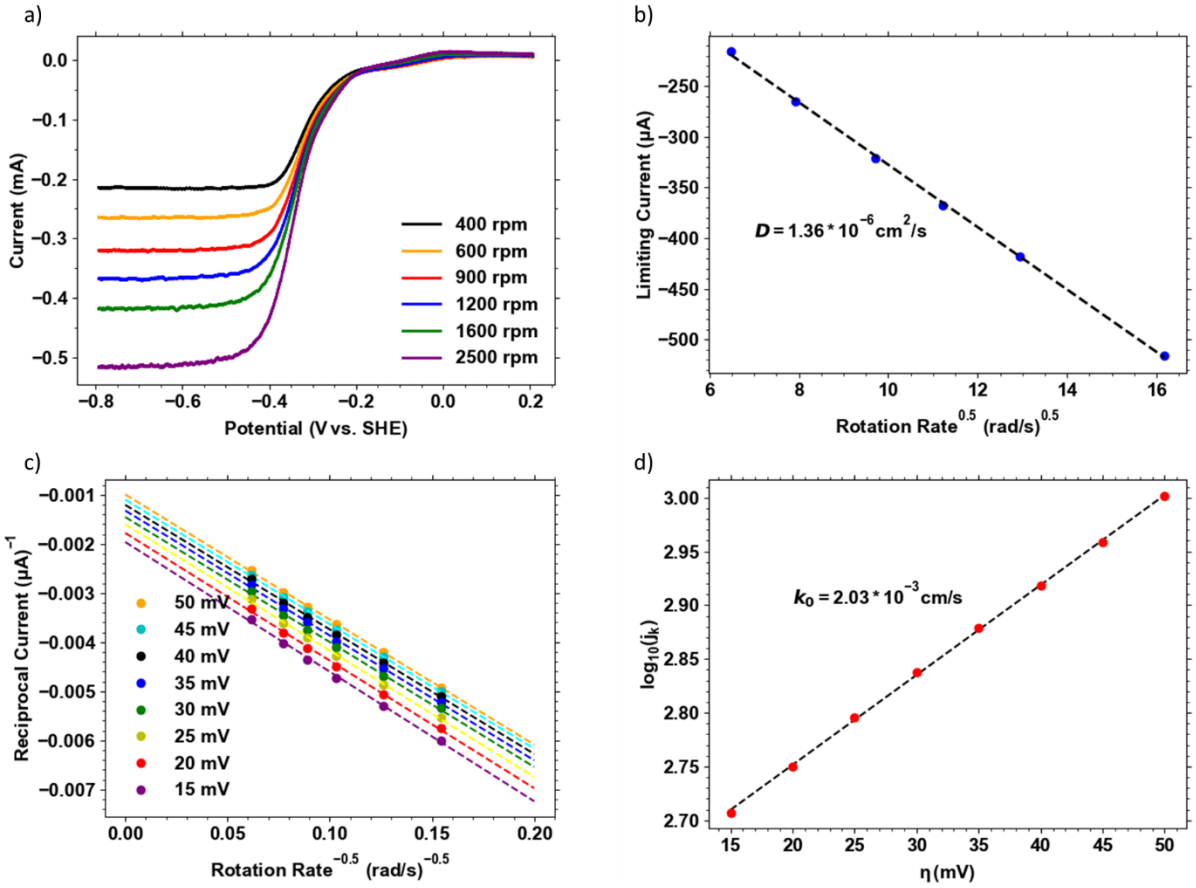

Figure S10 *Rotating disk electrode tests using 5 mM 1,5-BTMAP-AQ dissolved in 1 M KCl under nitrogen headspace. a) Linear sweep voltammograms on a glassy carbon rotating disk electrode at rotation rates between 400 and 2500 rpm with potential sweeping rate of 20 mV* s^{-1}*. b) Levich plot of limiting current versus square root of rotation rate. c) Koutecký–Levich plot at different overpotentials. (d) Fitted Tafel plot.*

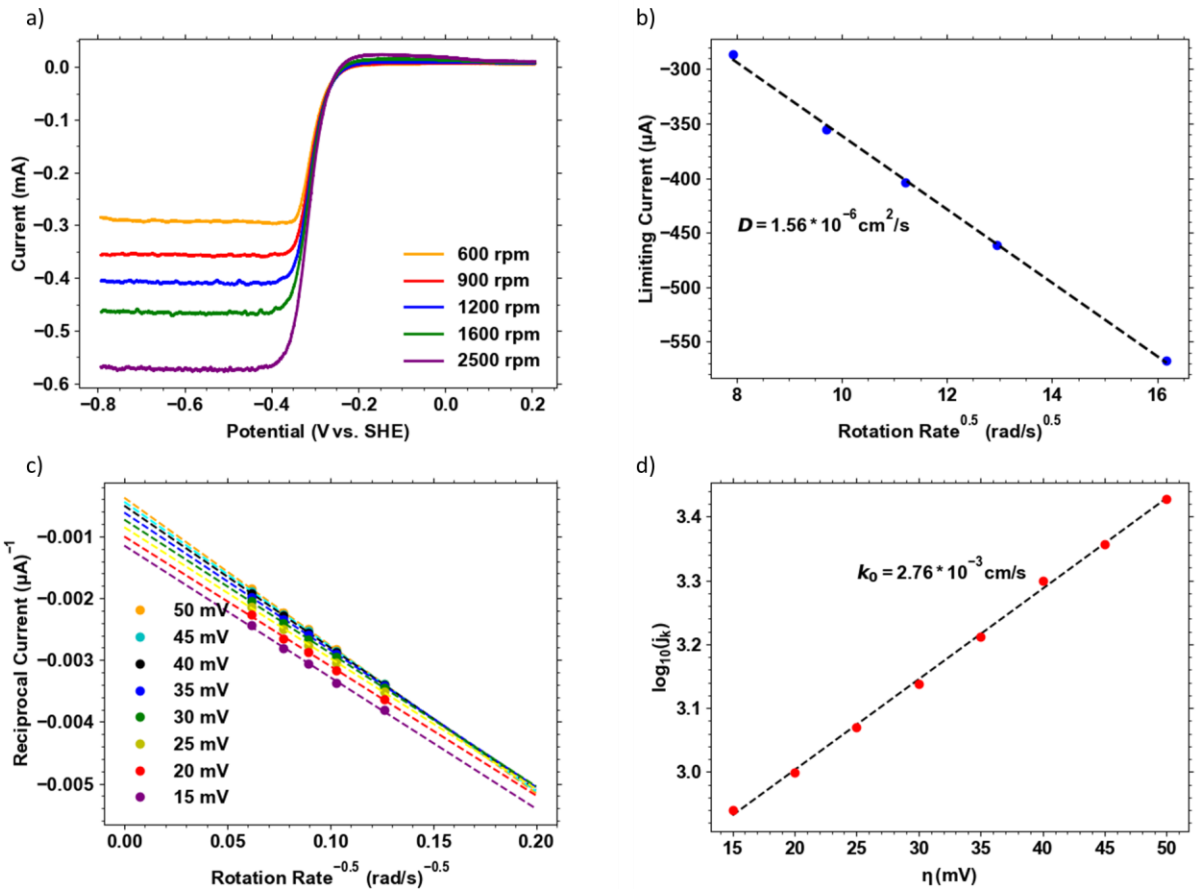

Figure S11 *Rotating disk electrode tests using 5 mM 1,8-BTMAP-AQ dissolved in 1 M KCl under nitrogen headspace. a) Linear sweep voltammograms on a glassy carbon rotating disk electrode at rotation rates between 400 and 2500 rpm with potential sweeping rate of 20 mV s^{-1}. b) Levich plot of limiting current versus square root of rotation rate. c) Koutecký–Levich plot at different overpotentials. (d) Fitted Tafel plot.*

4.6 Parameters extracted from fitting experimental CV profiles to the ECE mechanism scheme

Table S1: *Parameters extracted from fitting experimental cyclic voltammetry profiles of BTMAPAQ isomers to the ECE mechanism scheme.*

Parameters	*1-4BTMAPAQ*	*1-5BTMAPAQ*	*1-8BTMAPAQ*
k_0 *[cm/s]*	*1.46E-3*	*5.11E-4*	*1.75E-3*

k_0' *[cm/s]*	*4.90E-4*	*1.14E-3*	*6.70E-3*
k_c *[1/ s]*	*6.7*	*6.0*	*2.4*
E_1^o *[V vs SHE]*	*-0.371*	*-0.352*	*-0.379*
E_2^o *[V vs SHE]*	*0.106*	*0.206*	*0.133*
α_1	*0.32*	*0.23*	*0.37*
α_2	*0.54*	*0.66*	*0.64*
D [cm²/s]	*3.29E-6*	*1.00E-6*	*1.00E-6*
D_{add} *[cm²/s]*	*5.69E-6*	*2.34E-6*	*2.02E-6*

4.7 Comparing the rates of the BTMAPAQ$(CO_2)_2^{2-}$ adduct formation and bicarbonate formation

From our cyclic voltammetry, the rate constants values (k_c) found to be >192, >171, and 68.6 $M^{-1}s^{-1}$ (per moles of CO_2) for 1,4-, 1,5-, and 1,8-BTMAPAQ isomers, respectively, indicating the rate constant for the occurrence of the nucleophilicity-swing mechanism. In contrast, the rate constant for bicarbonate/carbonate formation that is occurring in the pH-swing mechanism is reported to be $k_C' = 12.1 * 10^3\ M^{-1}s^{-1}$ at 25°C [Wang, Xiaoguang, et al. "Comprehensive study of the hydration and dehydration reactions of carbon dioxide in aqueous solution." *The journal of physical chemistry A* 114.4 (2010): 1734-1740]. Note that the protonation reaction of AQ needs to occur first before the bicarbonate/carbonate reaction can proceed. Therefore, the rate of protonation is also crucial. However, given the reports on the concerted protonation of quinones with the electron transfer in aqueous media [Costentin, Cyrille. "Electrochemical approach to the mechanistic study of proton-coupled electron transfer." *Chemical Reviews* 108.7 (2008): 2145-2179], it is reasonable to assume that the rate of the bicarbonate/carbonate reactions is the limiting factor in the pH-swing mechanism. Additionally, given a single merged peak for the BTMAPAQ$(CO_2)_2^{2-}$ in the cyclic voltammetry plot, the two-step complexation of BTMAPAQ with CO_2 must have occurred with small potential separations. The extracted rate constants from the CV plots are attributed to the first step in complexation of BTMAPAQ with CO_2, assuming that this is the limiting reaction. So, for the reaction $AQ^{2-} + CO_2(aq) \leftrightarrow AQ(CO_2)^{2-}$, the rate is written as $R_{AQ,adduct} = k_c[CO_2(aq)][AQ^{-2}]$, whereas for bicarbonate formation the rate would be $R_{bicarbonate} = k'_c[CO_2(aq)][OH^-]$.

Taking the extracted rate constants and the relationship described above, we can find the rate of the two mechanisms under different hypothetical conditions. For example, under the conditions of high AQ concentration of 1 M, 0.1 bar of $CO_2(aq)$ and 0.1 M of OH^-, for the compound 1,5-

BTMAPAQ, the rate would be $R_{AQ,adduct} = 192\ [M^{-2}s^{-1}] * 0.0035\ [M] * 1[M] = 0.672\ [M\ s^{-1}]$, whereas for bicarbonate formation the rate would be $R_{bicarbonate} = 12.1 * 10^3[M^{-2}s^{-1}] * 0.0035\ [M] * 0.1\ [M] = 4.235\ [M\ s^{-1}]$, suggesting that bicarbonate formation is kinetically favorable even at high concentrations of AQ. Under such conditions, the OH^- concentration needs to be 0.01 M or less for the rates to become comparable.

5 Information corresponding to the "In Situ Method 1: Reference Electrode" Section

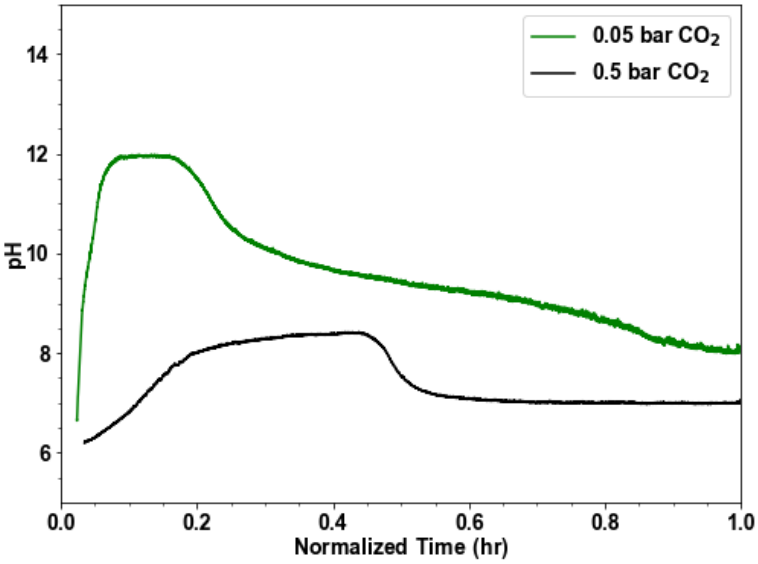

Figure S12 *pH change monitored in the negolyte during charge and rest time after charge of a flow cell comprising 10 mL of 0.115 M 1,5-BTMAPAQ negolyte paired with 1 M KCl and 40 mL of 0.2 M FcNCl in 1 M KCl posolyte purged with 50%* CO_2*/50%N2 (0.5 bar* CO_2*) and 5%* CO_2*/95%N2 (0.05 bar* CO_2*). Initially, the pH rises, but subsequent formation of bicarbonate/carbonate buffers the solution. Note that because of buffering, the pH remains below the the* pKa_2 *of BTMAPAQ. Additionally, it was observed that a higher partial pressure of* CO_2 *led to a faster occurrence of carbonate/bicarbonate buffering, preventing the pH from reaching higher values.*

5.1 Prior literature on the use of in situ reference electrodes in electrochemical cells

The use of in situ reference electrodes in electrochemical cells to measure the half-cell potentials of the negative and positive electrodes separately has been employed in various types of cells, such as lithium-ion batteries, fuel cells, and redox flow batteries (RFBs). This approach allows for the characterization of individual half-cells, providing information about potential distribution, kinetics, and overpotential for each half-cell reaction. The concept was first described in fuel cells, where a fine reference wire is sandwiched between membranes or enclosed within a region of the polymer electrolyte that extends past the cell. This approach was later implemented in redox flow

batteries. The use of in situ reference electrodes in flow cells is particularly advantageous. The electrolyte in flow cells circulates outside of the battery, facilitating easy access to the electrolyte and allowing the integration of a reference electrode without placing it inside the battery cell itself, thereby avoiding potential interference with cell operation.

Several earlier studies pertaining to all-vanadium redox flow batteries (RFBs) utilized in situ reference electrodes for polarization analysis. For instance, Langner et al. [Langner, Joachim, et al. "Determination of overpotentials in all vanadium redox flow batteries." *ECS Transactions* 58.37 (2014): 1] and Derr et al. [Derr, Igor, et al. "Degradation of all-vanadium redox flow batteries (VRFB) investigated by electrochemical impedance and X-ray photoelectron spectroscopy: Part 2 electrochemical degradation." *Journal of Power Sources* 325 (2016): 351-359.] positioned Ag/AgCl reference electrodes at the inlets of the battery, among the first studies demonstrating direct monitoring of the electrolyte's potential in these RFBs. Aaron et al. [Aaron, Doug, et al. "Polarization curve analysis of all-vanadium redox flow batteries." *Journal of Applied Electrochemistry* 41 (2011): 1175-1182] [Aaron, Douglas, et al. "In situ kinetics studies in all-vanadium redox flow batteries." *ECS Electrochemistry Letters* 2.3 (2013): A29] enhanced this method by inserting dynamic hydrogen electrodes with Pt wire between two layers of cation-exchange membranes, providing a more stable reference potential. Furthermore, a more intricate four-point design employing four Pt wire pseudo-reference electrodes has been proposed [Mazúr, Petr, et al. "A complex four-point method for the evaluation of ohmic and faradaic losses within a redox flow battery single-cell." *MethodsX* 6 (2019): 534-539], offering improved accuracy in potential measurements.

In our present work, we utilize in situ reference electrodes not for polarization breakdown, but to correlate the voltage plateaus and the capacity delivered at each plateau with the two distinct redox reactions of AQ^{2-} (or AQH_2) oxidation and AQ-CO_2 oxidation, which occur at separate redox potentials. The two plateaus are evident in the full cell voltage; however, this voltage is the result of the combined potentials of the negolyte and posolyte. We need to demonstrate that these two plateaus are indeed the result of two redox reactions on the negolyte side (the side where carbon capture is occurring in the system). This became possible through the insertion of a reference electrode to directly measure the negolyte potential.

As such, in this work, the application of in situ reference electrodes for dissecting the capacity delivered in electrolytes containing mixed redox-active species is demonstrated. By isolating and measuring the negolyte potential, we can specifically identify the contribution of the AQ-CO_2 adduct to the overall capacity. Furthermore, by subtracting the measurements obtained from external CO_2 sensors, which measure the total capture capacity, we can accurately determine the specific contribution of the pH-swing mechanism to the overall capacity. This approach allows us to differentiate and quantify the distinct contributions of various redox-active species within the electrolyte, providing a clearer understanding of the underlying electrochemical processes.

5.2 Operation of flow cells and schematic and pictures of the flow cell equipped with a reference electrode

Here we provide more details regarding the operation of flow cells. Flow cells were charged using the constant current followed by constant voltage (CCCV) method. A constant current of 20 mA/cm^2 was applied until the voltage reached 1.4 V, afterward, the voltage was held at this value until the current dropped to 1 mA/cm^2. The use of the CCCV method ensures that we access the majority of the cell's capacity and charge it close to 100%. During the experiment, charging was conducted under a 100% N_2 environment. After completing the charge, the battery was put to rest, and we began purging with 10% CO_2 + 90% N_2 for 60 minutes. At the end of the 60 minutes, the gas ratio changed back to 100% N_2 while the battery was at rest. Once the gas was stable at 100% N_2, we began the discharge with the CCCV method. After the completion of discharge, we put the battery under rest to ensure all the captured CO_2 was released back.

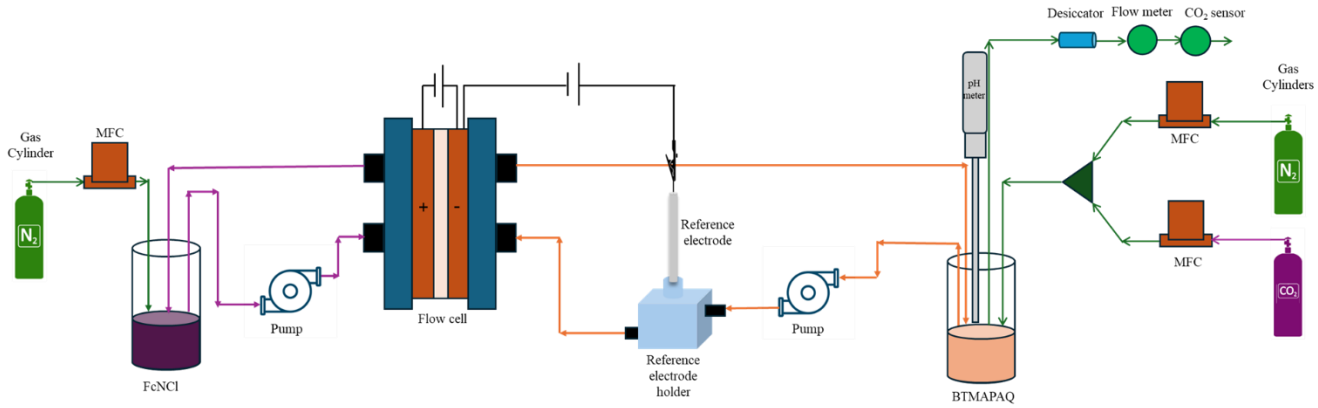

Figure S13 *Schematic of the setup used for the in situ reference electrode study.*

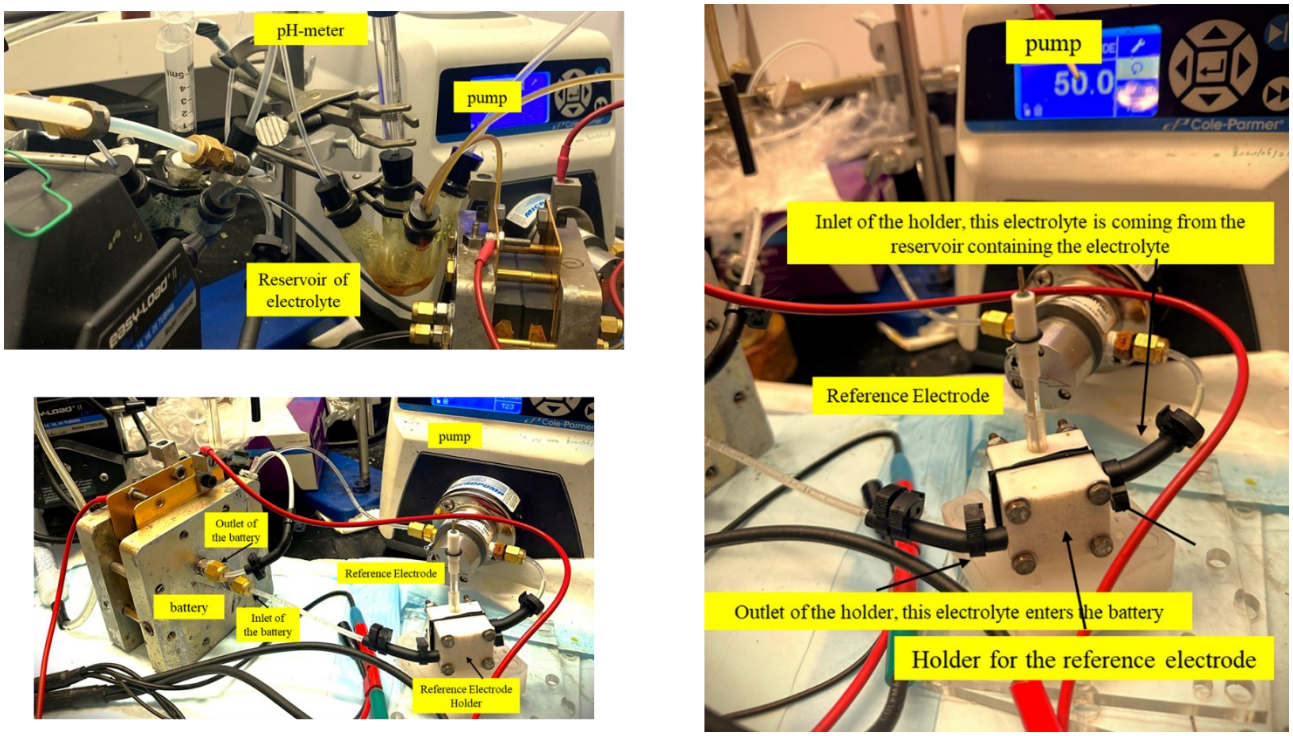

Figure S14 *Pictures of the setup used for the in situ reference electrode study.*

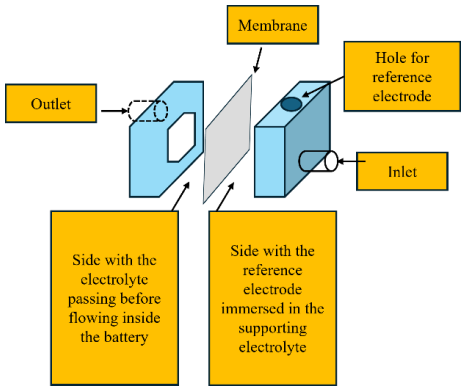

Figure S15 *Schematic of the reference electrode holder.*

5.3 Calibration procedure for the reference electrode

The Hg/HgO reference electrode (BASi EF-1369) was calibrated against a master Ag/AgCl electrode in 1 M NaOH, where the expected potential against Ag/AgCl is -80 mV ± 20 mV. Between each experiment, the reference electrode was removed from its holder and measured against the master electrode to ensure proper calibration. The internal solution of the electrode was refreshed as necessary to maintain accuracy.

The reference electrode holder is designed with one side allowing electrolyte flow, separated by a DSV-N membrane (the same membrane used inside the battery). The other chamber contains the supporting electrolyte (1 M KCl). Before each experiment, the supporting electrolyte solution in the reference electrode chamber was refreshed. For different experimental sets, the chamber was opened, and the membrane was replaced to ensure consistency.

To verify the performance of the reference electrode, the battery was cycled under a nitrogen environment for one cycle before starting the actual experiment. This preliminary cycle allowed us to compare data and confirm that the reference electrode was functioning correctly. Given that each experimental cycle was relatively short (approximately one hour, as shown in Figure 3), the reference electrode maintained stable performance across multiple cycles before requiring refreshment.

5.4 Detailed Explanation of each subfigure in Figure 3 in the manuscript

In this section, we provide comprehensive details of each subfigure in Figure 3.

Summary of Figure 3a

Figure 3a presents an experiment where the cell was intentionally charged in a nitrogen environment, followed by a controlled purge with 0.1 bar CO_2 and 0.9 bar N_2 for 60 minutes, before switching back to the nitrogen environment. The top row of Figure 3a shows the upstream gas ratio, which is 100% nitrogen except for the 60 minutes of 10% CO_2 – 90% N_2 after the charge phase. The next rows display the voltage and pH changes during the entire experiment. The two bottom plots show the CO_2 pressure sensor and the flow meter data. The dashed red box around the downstream pCO_2 and flow rate data during discharge indicates where sensors detect a signal

for CO_2 release, which is the sum of releases from nucleophilicity swing and pH swing mechanisms. The gray dashed box around the discharge voltage refers to a double plateau that forms because a mixture of $AQ(CO_2)_2^{2-}$ and AQ^{2-} is present in the solution. This double plateau originates from the negative half-cell of the battery, as confirmed by the in situ reference electrode in Figure 3b. From the capacity delivered at the more positive redox potential, we can back-calculate the $AQ(CO_2)_2^{2-}$ concentration.

Summary of Figure 3b

Figure 3b shows a zoomed-in view of the cell voltage from Figure 3a, as well as the corresponding negative half-cell potential of the negolyte side measured via the reference electrode in the setup during this experiment. This demonstrates that the double plateau observed in the full cell voltage indeed stems from the double plateau in the negative half-cell and is due to a mixture of $AQ(CO_2)_2^{2-}$ and AQ^{2-} present in the solution.

Summary of Figure 3c

The experimental procedure described above was then conducted with different CO_2 purge durations. This was intentionally designed to allow us to control the amount of adduct formation during the course of the experiment and examine its relationship with the discharge voltage profiles. By controlling the duration of the purging CO_2, we aimed to create different ratios of $AQ(CO_2)_2^{2-}$ and AQ^{2-} and thus examine the resulting changes in the double plateaus forming in the voltage profile. Figure 3c and Figure S16 shows the experiments we conducted by controlling the duration of the purge. As the CO_2 purge time increases, we expect more CO_2 to be captured, leading to the formation of more $AQ(CO_2)_2^{2-}$. If the voltage profile is a reliable method for quantification, it should be sensitive to the purge duration. As shown in Figure 3c, longer purge times result in a more extended voltage plateau corresponding to $AQ(CO_2)_2^{2-}$, indicating that a larger capacity is delivered from reducing $AQ(CO_2)_2^{2-}$. This plot confirms that the voltage profile is indeed sensitive to the duration of the purging with CO_2 and can be used to quantify the amount of $AQ(CO_2)_2^{2-}$ by analyzing the capacity delivered at the corresponding voltage plateau.

Summary of Figure 3d

Figure 3d presents the quantification conducted. Note that the total theoretical CO_2 capacity, based on discharge capacities, is within the same range across all the experiments. This consistency is observed given that, in all tests, 12 ml of 0.1 M 1,5-BTMAP AQ was prepared. Furthermore, as anticipated, an increase in the duration of the purging with CO_2 leads to a proportional rise in the total captured amount measured by the sensor.

The calculation process is divided into several steps for ease of understanding.

1. **Theoretical CO_2 volume calculation based on discharge capacity**:

The light blue bar in Figure 3d demonstrates the theoretically expected CO_2 volume. It is calculated from the amount of capacity we found during the discharge phase. Below, please find a step-by-step example:

- An example is given where a discharge capacity of 172.69 C was observed (Figure 3a). This value translates to 8.95×10^{-4} moles of a compound being oxidized during the discharge phase. The calculation uses the formula Q = nFM, where Q is the charge (172.69 C), n is the number of electrons transferred (2), F is Faraday's constant (96485 C/mol), and M is the moles of the compound.
- To find the maximum expected volume, we assume that the entire capacity is derived from the oxidation of the $AQ(CO_2)_2^{2-}$ adduct (rather than AQ^{2-}), and so the theoretical maximum CO_2 released is calculated to be $2 \times 8.95 \times 10^{-4}$ moles. This is because each AQ^{2-} molecule binds to two CO_2 molecules. The total comes to 0.00178 moles, equivalent to 40 ml of CO_2 according to the ideal gas law.

2. **Measuring CO_2 volume released from the sensor**:

The dark blue bars in Figure 3d show the CO_2 volume measured using sensors, following the method outlined in a previous work (cite). Since the deviation from baseline the flow meter data is solely caused by CO_2 release, the amount of CO_2 release is calculated by integrating the difference between the recorded flow rate and the baseline. The formula used is:

$$Q_{CO_2} = \sum_{n=t_i}^{t_f} (\dot{V}^{base} - \dot{V}^n)\Delta t$$

where Q_{CO_2} is the volume of CO_2, t_i is the start time, t_f is the final time, $\dot{V}^n$ is the instantaneous volumetric flow rate at the nth data recording time t_n , and $\dot{V}^{base}$ is the baseline flow rate. Figure S17 shows the integration and quantified volume for each of the bars shown in Figure 3d. It is important to note that this measurement includes contributions from both nucleophilicity and pH swing mechanisms, as the sensor cannot distinguish between the two.

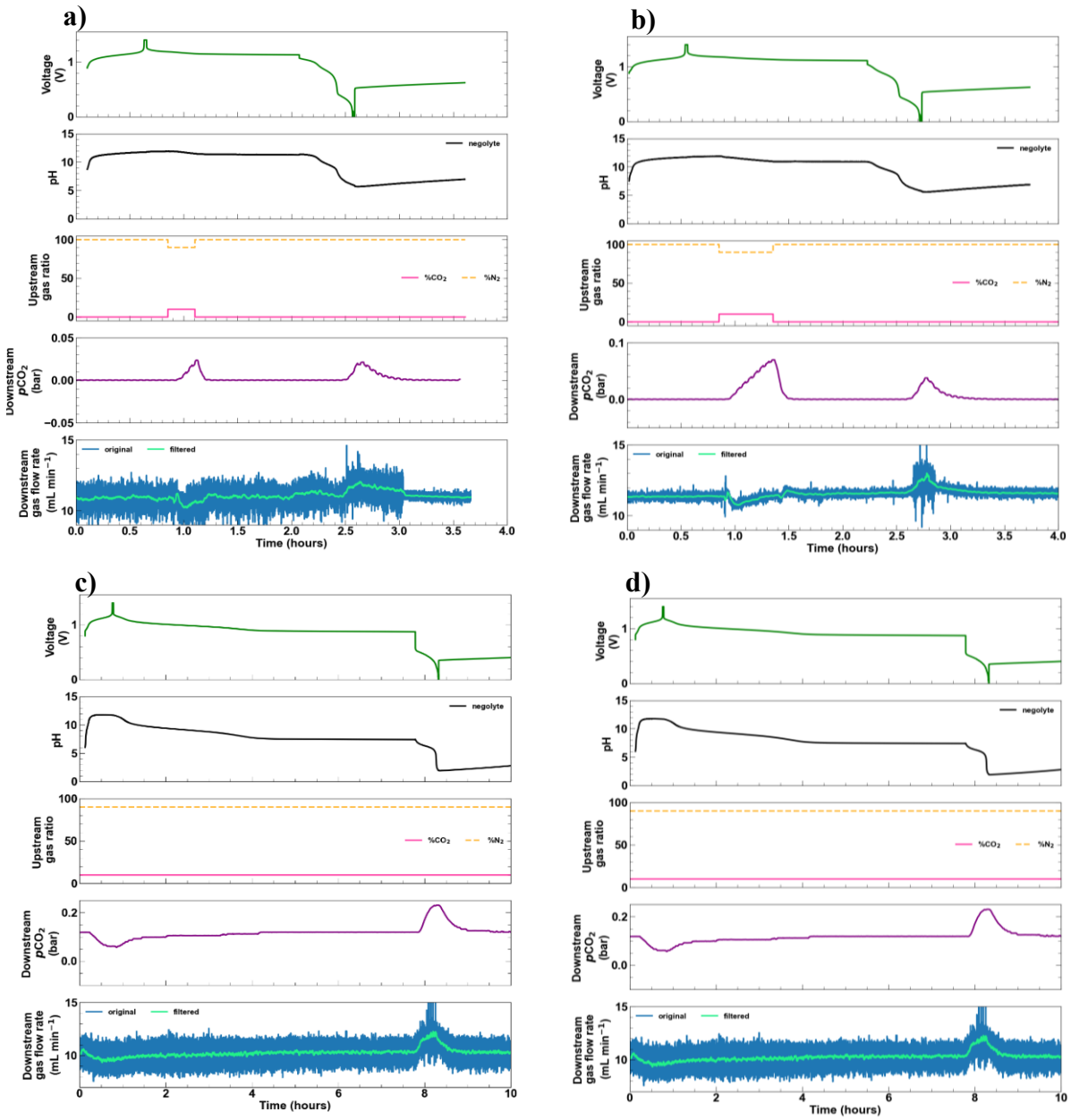

Figure S16 *Voltage, pH, upstream gas ratio, downstream partial pressure of* CO_2 *and downstream gas flow rate measured during the experiment utilizing a flow cell comprising 12 ml of 0.1 M 1,5BTMAP-AQ paired with 40 ml of 0.2 M BTMAP-FC. The cell was charged in a nitrogen environment, followed by a controlled 0.1 bar* CO_2 *environment for a) 15 minutes and b) 30 minutes followed by a switch back to the nitrogen environment. In a separate experiment, the cell was charged under 0.1 bar* CO_2 *introduced from the beginning of the test with a rest time of c) 120 minutes and d) 7 hours.*

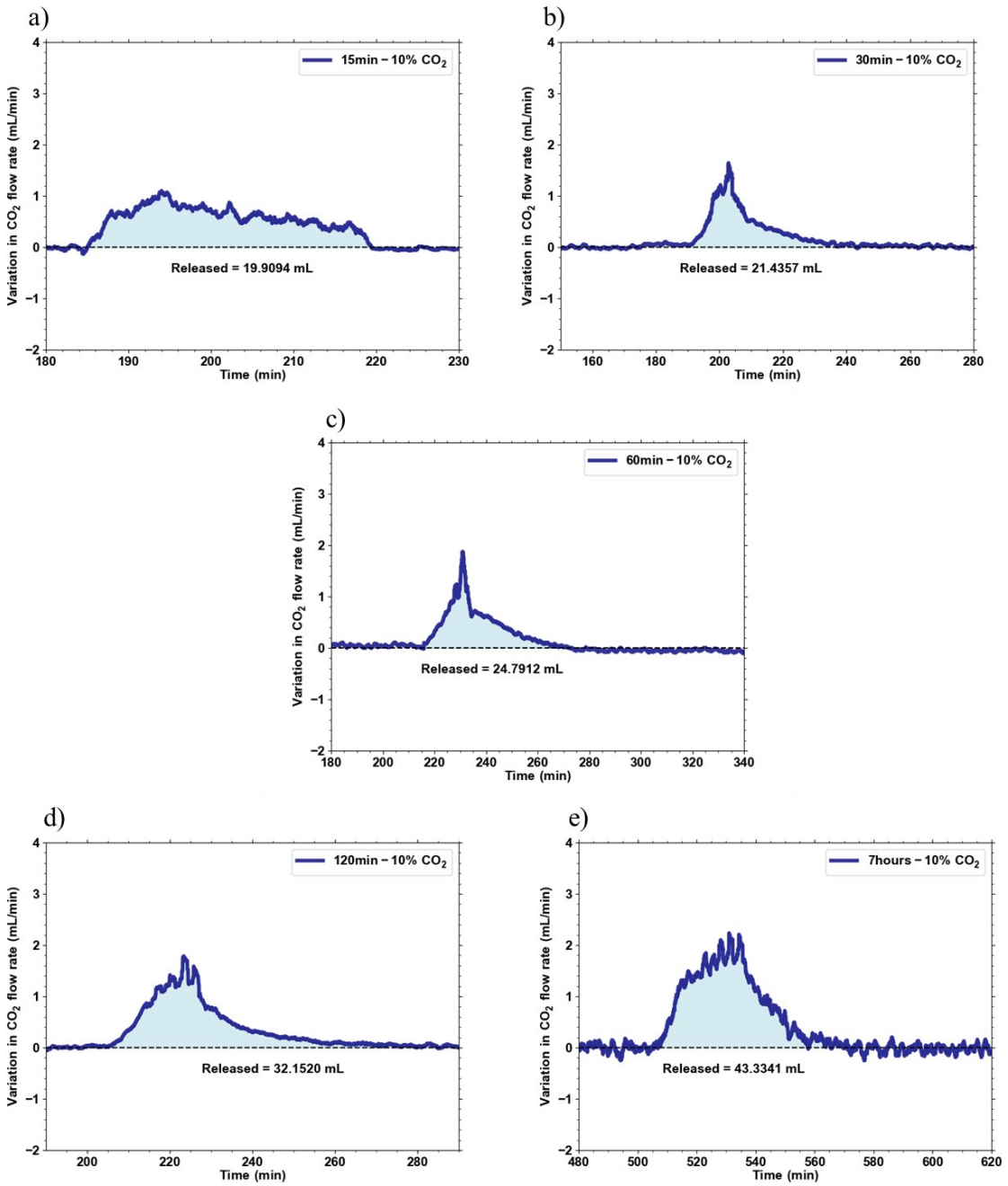

614 ***Figure S17*** *Calculated volumes of released* CO_2 *by 1,5-BTMAPAQs in a feed gas stream of 90%*
615 *N_2 and 10%* CO_2.

616

617 3. CO_2 **volume release based on discharge voltage**:

618 The orange bar refers to the CO_2 volume released solely from the $AQ(CO_2)_2^{2-}$. (nucleophilicity-
619 swing mechanism) that we could extract using the capacity delivered solely at the voltage plateau
620 of the $AQ(CO_2)_2^{2-}$. in the negative half-cell potential measured using the reference electrode (the

portion of the voltage delivered in the pink box in Figure S18. The capacity is the time duration corresponding to this portion of the voltage plateau times the current. We only consider the discharge capacity relevant to this voltage plateau.

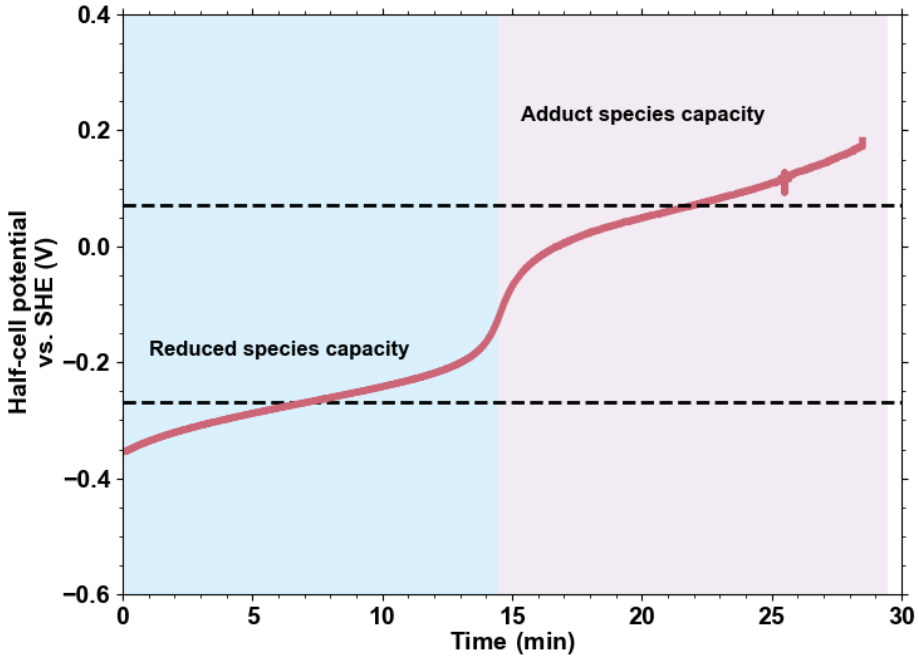

Figure S18 *Negative half-cell potential measured via in situ reference electrode during operation (measured during experiment shown in Figure 3a). The portion of the voltage plateau in the pink area refers to the capacity delivered via* $AQ(CO_2)_2^{2-}$ *compound.*

This capacity is then converted to CO_2 volume released, attributed solely to the $AQ(CO_2)_2^{2-}$ adduct formation mechanism, as it is measured at the voltage signature of the $AQ(CO_2)_2^{2-}$ adduct's redox potential. To convert capacity to CO_2 volume, we first back-calculate the moles of $AQ(CO_2)_2^{2-}$ from this capacity using the formula Q=nFM, where Q is the capacity, n is the number of electrons transferred (2), F is Faraday's constant (96485 C/mol), and M is the moles of the compound. Once we find the moles of $AQ(CO_2)_2^{2-}$ formed during each experiment, we can determine the moles of CO_2 it contains (each mole of AQ^{2-} accepts two moles of CO_2 to form the $AQ(CO_2)_2^{2-}$ complex). Using the ideal gas law, we then calculate the volume of CO_2 corresponding to that number of moles (1 mole of ideal gas is 22.4 L).

4. **Determining the pH swing contribution**:

To isolate the contribution from the pH swing mechanism, we subtract the CO_2 volume attributed to the $AQ(CO_2)2-$ adduct formation (orange bars) from the total volume measured by the sensor

(dark blue bars). The remaining volume must have been captured through the pH swing mechanism.

Note that we have additionally conducted a test using the same 10 ml of 0.1 M solution of 1,5 BTMAPAQ at 100% CO_2 at 1 bar, introduced from the beginning of the tests with a wait time of 105 minutes after the charging phase for complete transition to equilibrium. Similarly, under this condition, we see the complete dominance of the nucleophilicity-swing mechanism. The expected maximum CO_2 volume release from this experiment is 38.5 ml (based on the discharge capacity) delivered all at the potential signature of the AQ-CO_2 adduct (single plateau), and the number registered from the sensor is close to this value at 39.4 ml, further confirming the dominance of nucleophilicity-swing mechanism at equilibrium under these conditions.

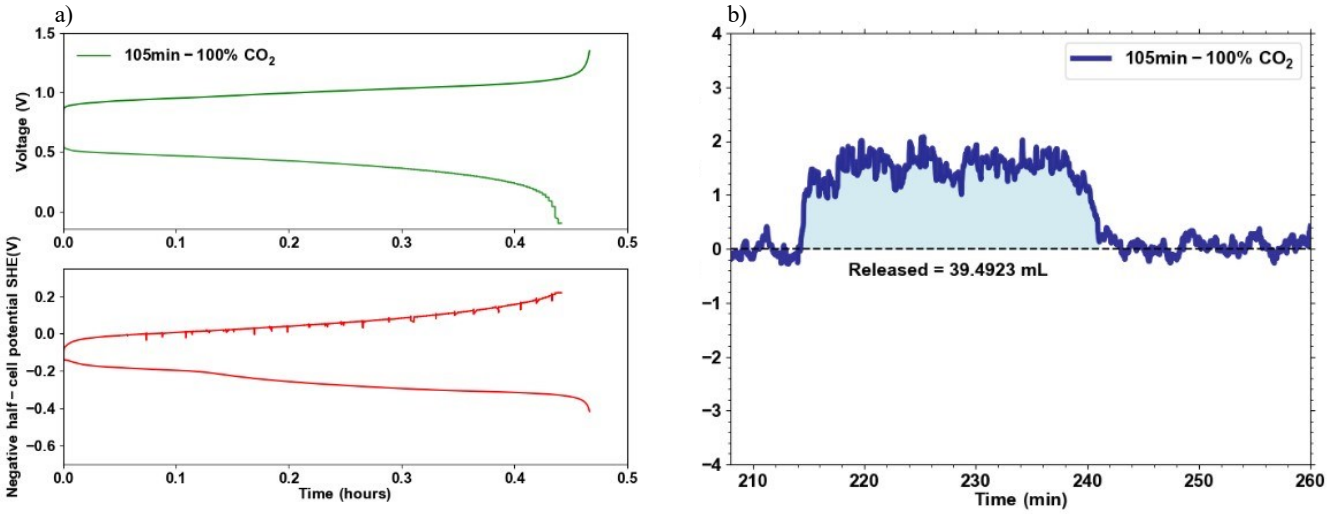

Figure S19 a) Full-cell and half-cell potential during an *experiment utilizing a flow cell comprising 10 ml of 0.1 M 1,5BTMAP-AQ paired with 40 ml of 0.2 M BTMAP-FC. The cell was charged under 1 bar* CO_2 *introduced from the beginning of the test with a rest time of 105 minutes. b) Calculated volume of released* CO_2 *during the experiment.*

Summary of Figure 3e

Figure 3e, we repeated the above experiments using a different isomer of BTMAPAQ (1,4 BTMAPAQ) at a high concentration of 0.4 M and a dilute concentration of CO_2 (99% N_2, 1% CO_2) to demonstrate that the method can be applied across different conditions. The individual experiments are shown in Figure S20.

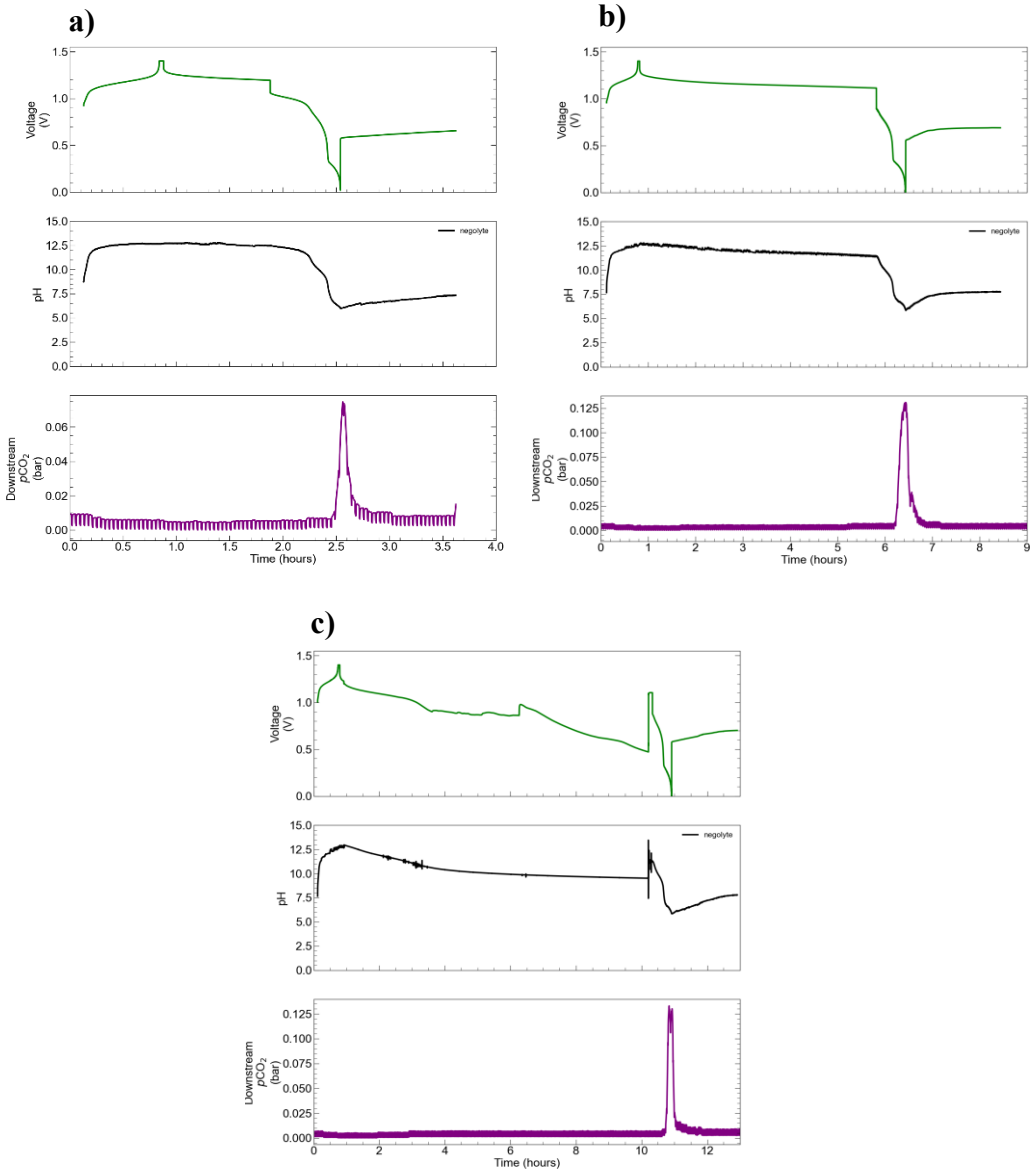

Figure S20 *Voltage, pH and downstream partial pressure of* CO_2 *measured for a cell with 7 ml of 0.4 M of 1,4-BTMAP-AQ and very diluted* CO_2 *concentrations of 0.01bar with rest durations of a) 1 hour, b) 5 hours and c) 10 hours after the charged phase.*

The bars shown in Figure 3e were quantified using the same procedure discussed above for Figure 3d. The only difference is that, given the dilute 1% CO_2 gas condition, we increased the gas flow rate from 11.25 ml/min in previous experiments to 22.5 ml/min to facilitate the capture process under such dilute conditions. Under these conditions, we directly used the pCO_2 sensor data to measure CO_2 release by integrating the area under the downstream pCO_2 release peak (in bar*hours). Given a gas flow rate of 22.5 ml/min, the CO_2 volume is calculated using the ideal gas law. The pCO_2 sensor and quantification data are shown in Figure S21.

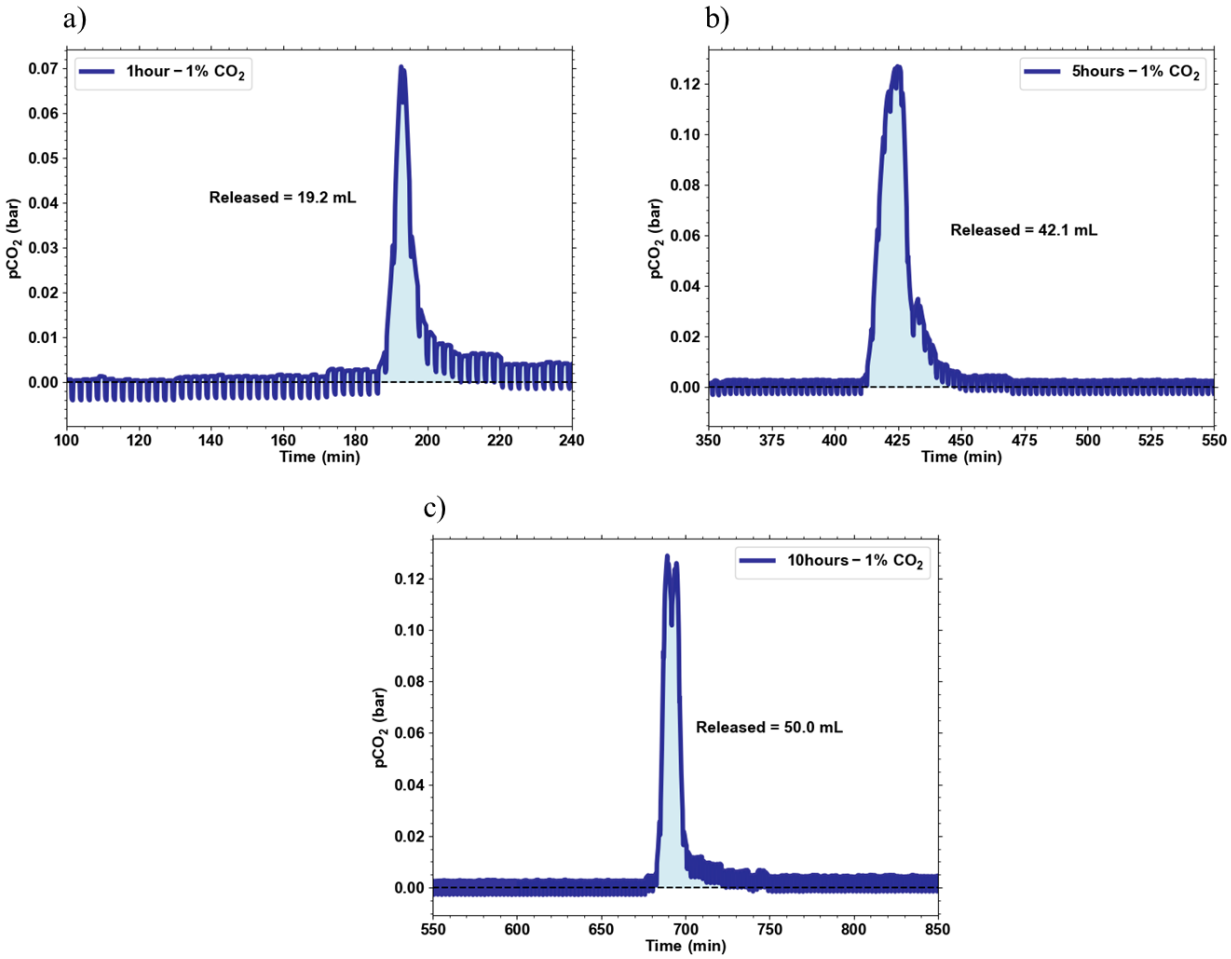

Figure S21 *Calculated volumes of released* CO_2 *by 1,4-BTMAPAQs in a feed gas stream of 99%* N_2 *and 1%* CO_2.

A Note About Sensor Accuracy

For the calculations in Figure 3d, we set the flow rate to 11.25 ml/min. The flow meter has an accuracy of ±1.5% (0-30 sccm) based on its specification. To calculate the error in the volume measurement, we first determined the error in the flow rate set to 11.25 ml/min, which is ±0.16875 ml/min. Given that the volume is the integral of the flow rate over time, the relative error in the flow rate propagates to the volume measurement. For example, if we measured a volume of 40 ml, the relative error in the flow rate is approximately 1.5%, leading to an absolute error in the volume of ±0.6 ml. Therefore, the volume of CO_2 released is 40 ml ± 0.6 ml.

For Figure 3e, as mentioned in SI "Summary of Figure 3e", the volume of CO_2 released was determined by integrating the partial pressure of CO_2 over time, multiplying by the flow rate, and using the ideal gas law. The CO_2 sensor has an accuracy of ±300 ppm ± 5% of the reading. For example, for an integrated partial pressure reading of 0.1 bar and a flow rate of 22.5 ml/min, the CO_2 sensor error is approximately ±0.0053 bar and the flow meter error is ±0.3375 ml/min. Combining these errors, the relative total error was found to be approximately 5.5%. Therefore, for a calculated volume of 40 ml of CO_2, the error is ±2.2 ml.

Figure 3e (sensor accuracy)	
Measured from flow sensor(ml)	Error (ml)
19.56	±0.29
21.41	±0.32
22	±0.33
32.12	±0.48
44.2	±0.66

Figure 3d (sensor accuracy)	
Volume (ml)	Corrected Error (ml)
19	±1.0081
42.14	±2.1339
50	±2.5236

5.5 Understanding variations in measured voltage and half-cell redox potentials across experimental conditions shown in Figure 3.

It can be observed in Figure 3b that across different experiments with varying durations of CO_2, resulting in different ratios of AQ-CO_2 adduct, bicarbonate, and carbonate forms, there is variation in the measured potential; in other words, the voltage profiles do not overlay at the starting point. There are two primary reasons for this. Firstly, the observed shifts in half-cell potentials can be attributed to variations in pH resulting from different durations of CO_2 purging during the experiments. Figure S16 illustrates how each duration of purging with CO_2 results in a different pH at the onset of discharge. For simplicity, we have included here Figure S22, which overlays the pH change for 2 experiments where the cell was purged with CO_2 during the charging process for 15 minutes and 120 minutes, respectively. pH influences the redox potential of anthraquinones according to their Pourbaix diagram after protonation. The redox potential changes by approximately 0.0591 V (or 59.1 mV) for each unit change in pH in reactions involving the transfer of 2 protons and 2 electrons. Therefore, we did not expect the potentials for each run to overlay perfectly, as each occurs at a different pH due to varying amounts of CO_2 captured. Secondly, a more pronounced reason behind this shift is related to the properties of an electrolyte containing a mixture of redox-active species. Our prior computational and experimental studies (Amini, Kiana, et al. "Electrochemical Performance of Mixed Redox-Active Organic Molecules in Redox Flow Batteries." *Journal of The Electrochemical Society* 170.12 (2023): 120535.) have shown that changes in the concentration ratios of these species within the electrolyte can lead to observable shifts in half-cell potentials. Our previous work discussed the intricate reasons behind these shifts in such mixtures. In summary, depending on which species predominates in the electrolyte, the kinetic and mass transfer losses in the system would differ, resulting in shifts in the overall half-cell potential. These shifts do not affect our results. What's crucial is the capacity delivered at each plateau. AQ-CO_2 exhibits a more positive redox potential, while AQ^{2-} shows a more negative one, rendering the exact potential position inconsequential. Our focus lies on the capacity achieved at each plateau. This principle holds particularly true when species feature significant potential disparities (250-300 mV and higher). When the potential difference is narrower (less than 150-200 mV), distinguishing between voltage plateaus becomes challenging, potentially resulting in a blend of both reactions' capacities due to their closely aligned redox potentials. In such scenarios, our experimental approach remains viable but necessitates coupling with a model akin to our previous work to ascertain individual concentrations.

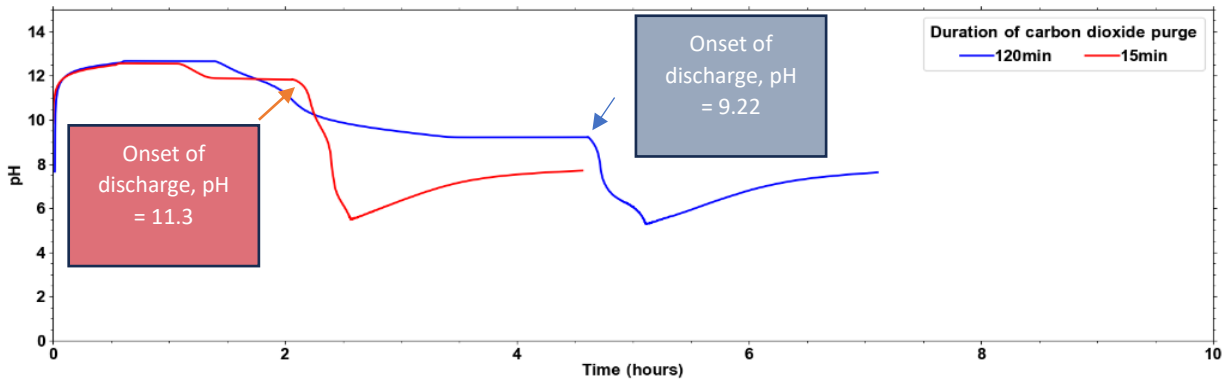

728

729

730 ***Figure S22***: *pH profile measured during the experiment described in Figure 3 for the*
731 *experiments where cell was purged with* CO_2 *for 120 minutes and 15 minutes during charge,*
732 *respectively. The figure emphasis the pH at the onset of the discharge for the two experiments.*

6 Information corresponding to the "In Situ Method 2: Fluorescence Visualization" Section

6.1 . UV-Vis experiments

UV-Vis absorbance spectra were obtained with a DH-2000-BAL UV-Visualization light source from Ocean Optics with optical fiber connectors, a quartz cuvette, and a cuvette holder with inlet and outlet allowing for continuous flow of electrolyte. The cuvette holder was positioned before the inlet of the flow cell, as shown in Figure S23. The cuvette pathlength was 100 μm. All the absorbance spectra are blank corrected.

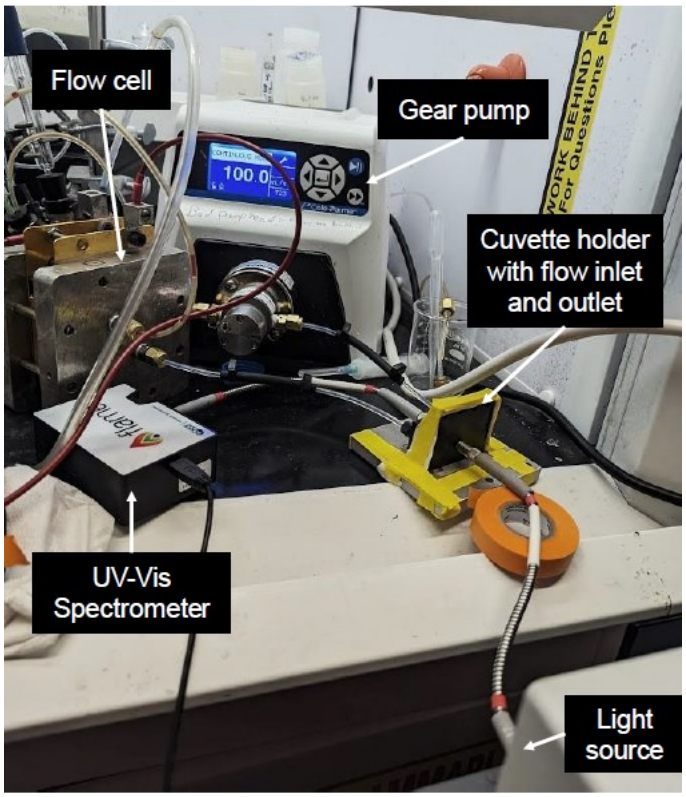

Figure S23 *Experimental setup for obtaining UV-Vis spectra. Optical fiber connectors connect the light source to the cuvette holder, and the cuvette holder to the UV-Vis spectrometer. The gear pump enables electrolyte solution to flow between the cuvette holder, flow cell, and electrolyte reservoir (not shown).*

In addition to the experiment discussion in Figures 4a and 4b (resting the battery under of streams of pure N_2 followed by CO_2 and registering the absorbance spectra), we monitored the absorbance spectra of the BTMAPAQ separately under N_2 and CO_2 environments in separate experiments, as illustrated in Figure S24. These experiments similarly revealed minor changes between the spectra under these conditions.

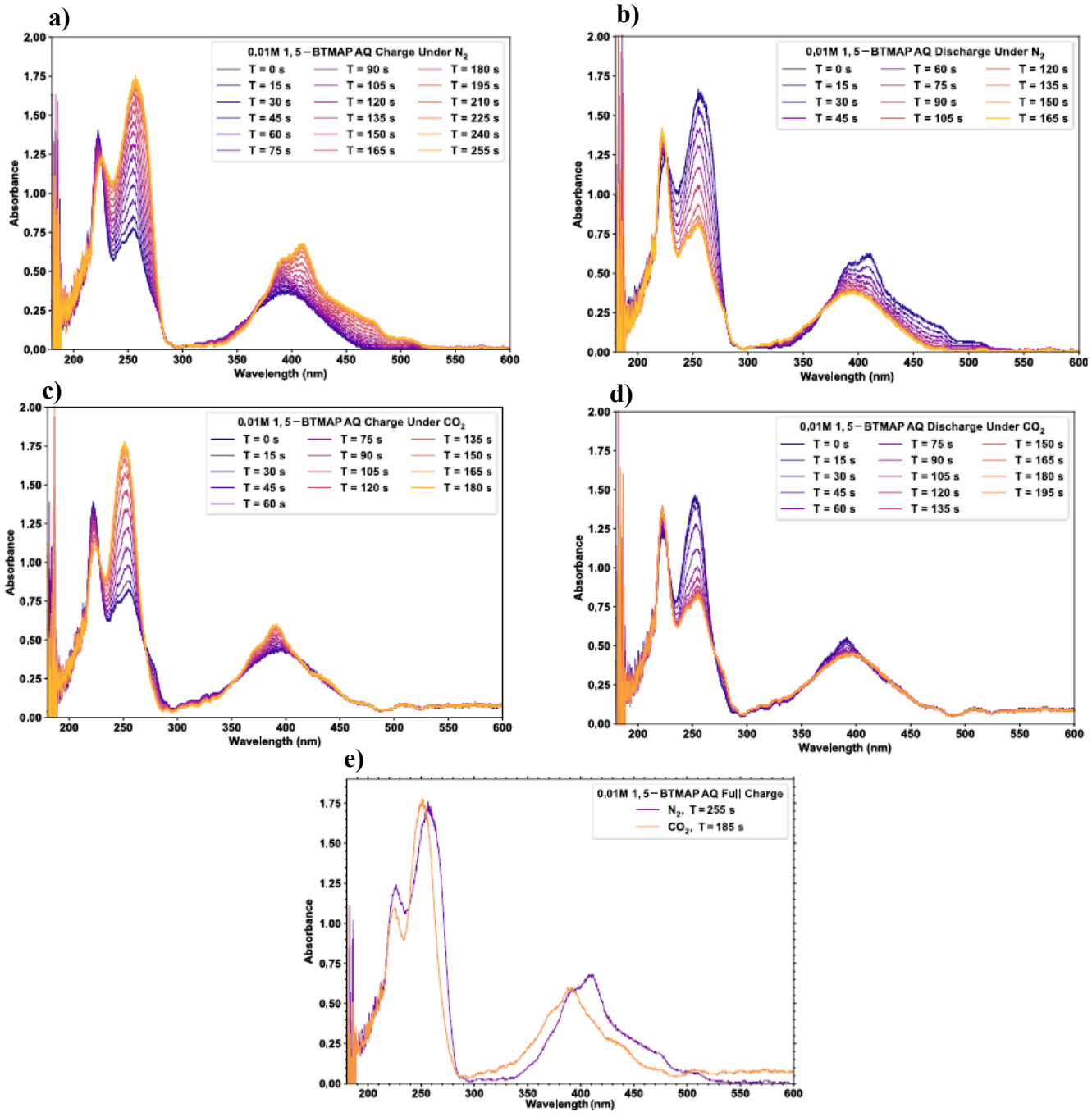

Figure S24 *In Situ UV-Vis absorbance spectra of 0.01M 1,5-BTMAPAQ in a flow cell against BTMAPFC posolyte during (a) charging (b) and discharging under a N_2 headspace gas environment and (c) charging and (d) discharging under a CO_2 headspace gas environment. (e) Spectra comparing fully charged 1,5-BTMAPAQ under N_2 with fully charged 1,5-BTMAPAQ under CO_2.*

6.2 Adapting the In Situ Fluorescence Method for Various System Conditions

The in situ fluorescence technique for parallel monitoring of AQ and AQ-CO_2 molecules relies on the distinct fluorescence characteristics of the quinone species and their complexes with CO_2. Like other detection methods such as voltage signature, IR, NMR, and Raman spectroscopy, the corresponding signatures (in our case, fluorescence) must be distinct to utilize this method effectively. As long as the molecules of interest exhibit a fluorescence signature and have regions where different band-pass filters can distinctly monitor them, this method can be employed. new quinone derivatives, it is reasonable to expect that the AQ-CO_2 adduct would have different fluorescence properties than AQ. The formation of the AQ-CO_2 adduct involves the binding of a CO_2 molecule to the anthraquinone core, introducing an electron-withdrawing group into the molecular structure. This interaction affects the electron distribution in the AQ molecule, particularly by increasing the electron density around the quinone core, resulting in potentially a different fluorescence emission compared to AQ alone. Our studies on other quinone derivatives, such as 22PEAQ and D2PEAQ (Figure S25), show that similar to BMTAPAQ, both the reduced and adduct species exhibit fluorescence, with the adduct form displaying significantly higher intensity. These molecules can be similarly tested under different excitation wavelengths to find regions where they can be detected distinctly using narrow band-pass filters. Like any other detection method, if the compound of interest changes, the signatures might change, but the procedure we followed for our molecule in the present work can serve as a recipe. Additionally, if different supporting electrolytes or additives are used instead of water and KOH, the supporting solution must be checked for fluorescence signatures, as demonstrated in Figure S26. Typically, the supporting electrolyte does not participate in the charge-discharge process, so even if it has fluorescence intensity, it can be subtracted, and the system will be background corrected.

6.3 Experimental details for acquiring the ex situ emission spectra

For ex situ experiments, a 5 ml solution of 0.1 M 1,5-BTMAPAQ (oxidized form) was first completely reduced against 15 ml of 0.2 M BTMAPFc in a flow battery inside the glovebox. Dry ice was then transferred inside the glovebox and added to the fully reduced solution to prepare the adduct form of 1,5-BTMAPAQ. Subsequently, 200 µL of each sample (oxidized, reduced, and adduct) was loaded into separate wells of a Greiner microplate (96 well, polystyrene, flat-bottom, µclear®, black, clear bottom) inside the glovebox. To prevent reoxidation due to the diffusion of atmospheric oxygen into the electrolytes, the microplate lid was sealed before taking the samples outside of the glovebox. The microplate was then transferred outside to a BioTek Synergy HT plate reader for photophysical experiments.

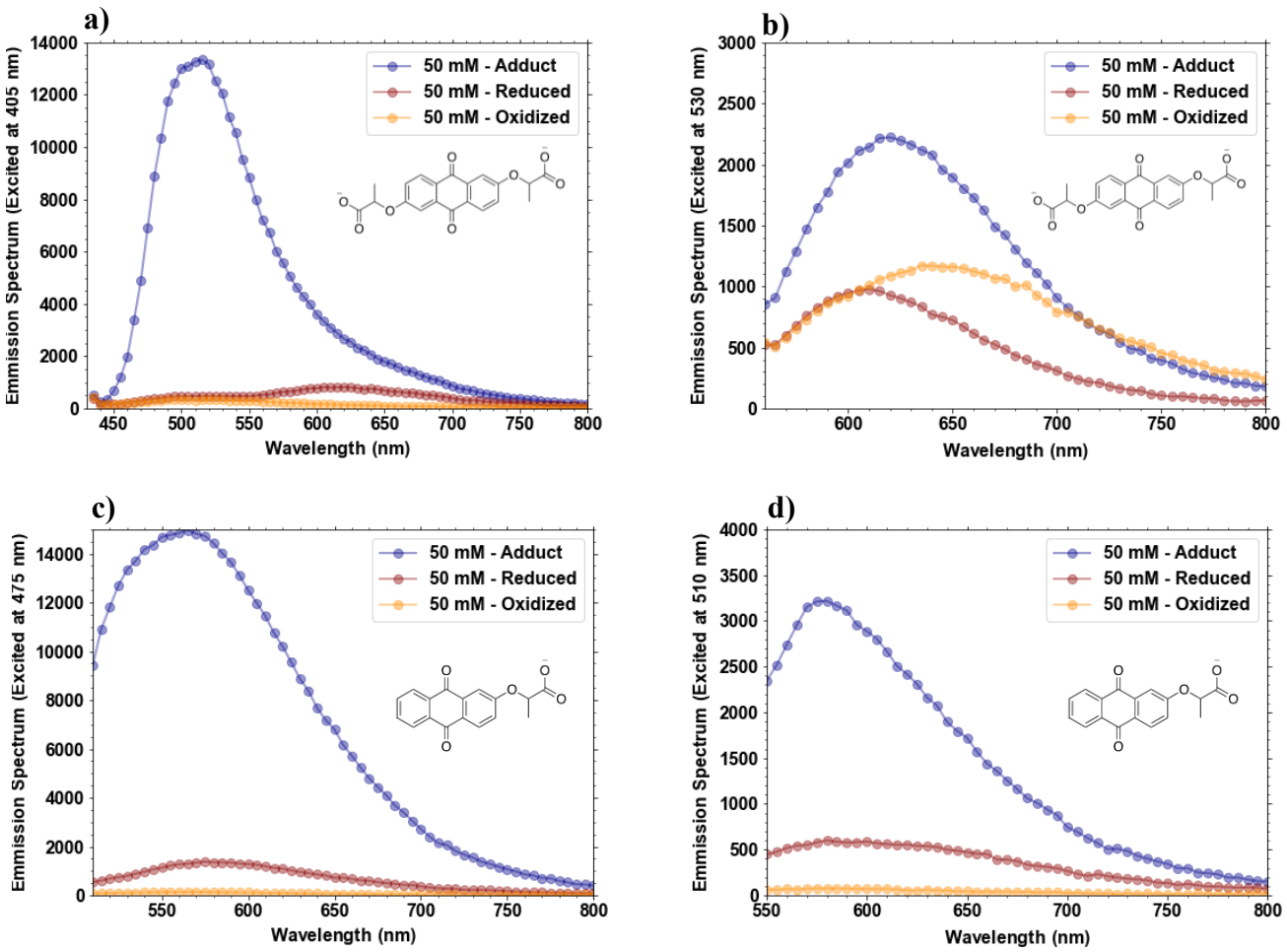

Figure S25 *Ex situ fluorescence spectra of 100 mM of the adduct, reduced and oxidized forms of D2PEAQ excited at a) 405 nm and b) 530 nm. Ex-situ fluorescence spectra of 100 mM of the adduct, reduced and oxidized forms of 22PEAQ excited at c) 475 nm and d) 510 nm. Note that the chemical structure shows the oxidized forms of the molecules mentioned.*

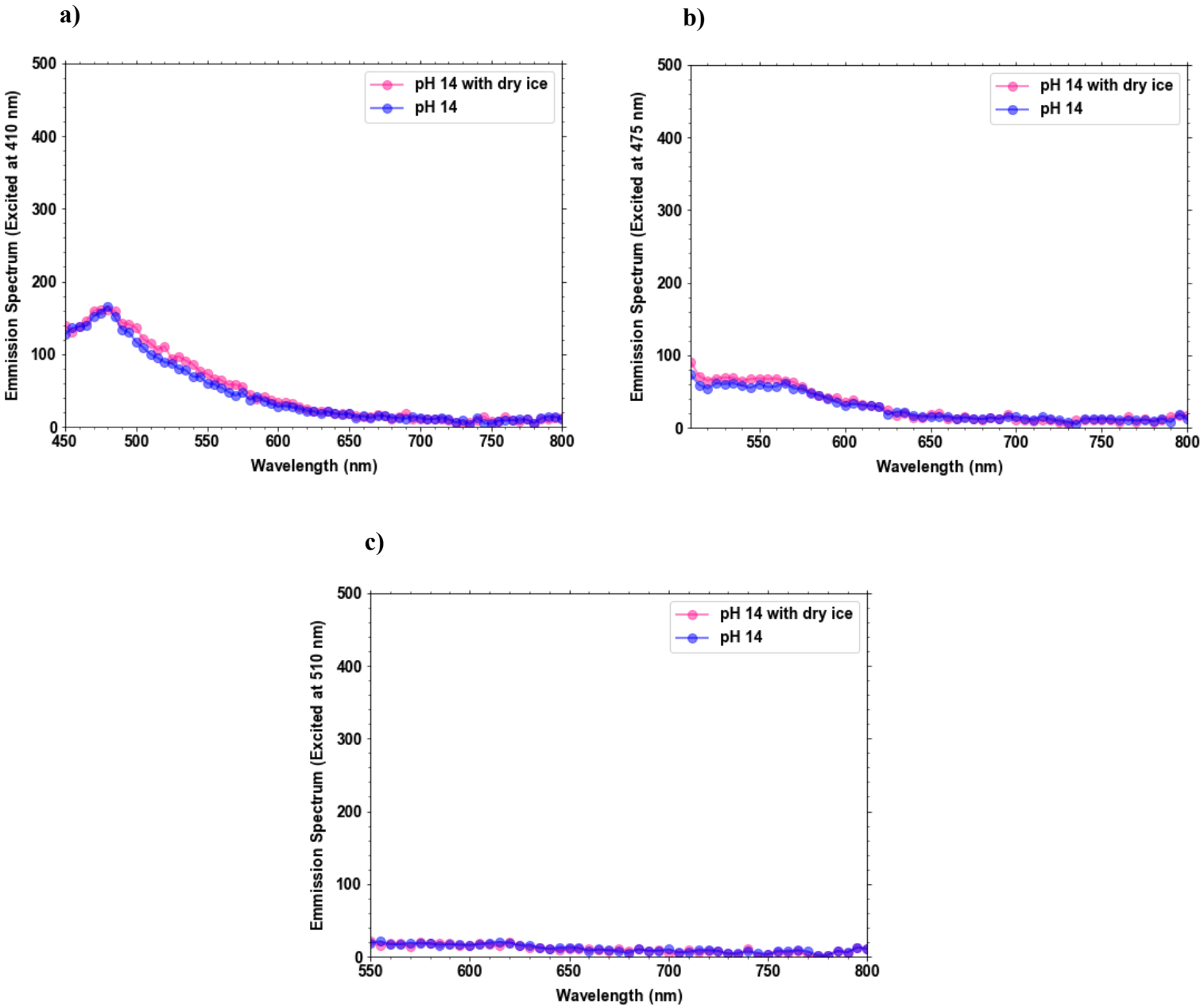

Figure S26 *Ex situ fluorescence spectra of 1 M KOH solution with and without addition of excess dry ice (to form carbonate and bicarbonate) excited at a) 410 nm, b) 475 nm and c) 510 nm.*

6.4 Experimental details for the in situ fluorescence microscopy setup

The electrochemical cell was assembled by combining two acrylic plates that enclosed a DSV-N membrane, sandwiching two Polydimethylsiloxane (PDMS) half-cells. The PDMS components, created through a process involving 3D printing and molding, began with the design and 3D printing of molds using Stereolithography (Form 3, Formlabs). Afterward, PDMS was poured into each mold, and expose to a vacuum in a desiccator to remove the air bubbles generated from the

mixing of the two part PDMS hence, ensuring prefect transparency and proper sealing. Following an overnight cure at 65°C, transparent acrylic endplates and screws were used to compress and assemble the PDMS half-cells, electrodes, and the membrane (See Figure S27). An AvCarb MGL 190 carbon paper of nominal thickness 190 μm was used as an electrode on each side. The electrode was baked for 24 h at 400 °C prior to the experiment. The DSV-N AEM was soaked in 1 M KCl prior to the experiments.

The microfluidic cell was then connected to two external reservoirs containing the positive electrolyte (posolyte) and negative electrolyte (negolyte) solutions. The negolyte consisted of 5 mL of 1,5-BTMAPAQ, either in 0.05 M or 0.1 M concentrations, dissolved in 1 M KCl solutions. In the case of Figure 6, the posolyte solution comprised 15 mL of 0.2 M BTMAPFC, while for Figure 7, it consisted of a mixture of 15 mL of 0.1 M ferricyanide and 0.1 M ferrocyanide in 1 M KCl. BTMAPFC is a better choice for the posolyte as it has negative counter ions and is more suitable for use with an anion exchange membrane. However, migration of hydroxides from the negolyte to the posolyte side can lead to iron hydroxide precipitation and potential tube clogging. Even a very negligible amount of precipitation will cause difficulties in the microfluidic cell. As such, short tests in the microfluidic battery utilized ferrocyanide/ferricyanide as the posolyte. The solutions were delivered to the cell through Grothen® peristaltic pumps, and all electrochemical tests were conducted using a Biologic SP-150e potentiostat.

The posolyte reservoir was continuously purged with a stream of N_2. On the negolyte side, the reservoir was equipped with a valve that allowed for switching between connection to a gas cylinder containing a pure stream of N_2 or CO_2. For tests involving more dilute concentrations of CO_2, the pure CO_2 cylinder was replaced with a 1% or 400 ppm CO_2 cylinder, with the rest of the composition being nitrogen. The inlet pressures of the gas streams were regulated using a Fluigent Flow EZ microfluidic controller. Additionally, the negolyte reservoir was equipped with a Mettler Toledo pH meter, which was connected to an Arduino board for continuous pH monitoring during operation.

Fluorescence microscopy was performed using a Leica DMi8 microscope body with a Dragonfly spinning disk equipped with a Leica 10x/0.3NA HC PL FLUOTAR lens. In all imaging experiments presented in this study, the following parameters were employed, unless specified otherwise: an exposure time of 2 seconds and an acquisition time of 2.5 seconds per frame. Two channels were configured with an excitation wavelength of 488 and an emission wavelength peaking at 594, as well as an excitation wavelength of 405 and an emission wavelength peaking at 521. Figure S28 shows pictures of the experimental setup with labels. Note that based on our fluorescence data achieved using the *ex situ* method (plate reader), an excitation wavelength of 475 nm was shown (in Figure 4d). In the *in situ* fluorescence microscope, the closest available excitation wavelength was 488 nm, which was utilized here and similarly resulted in distinct fluorescence signatures.

872

a)

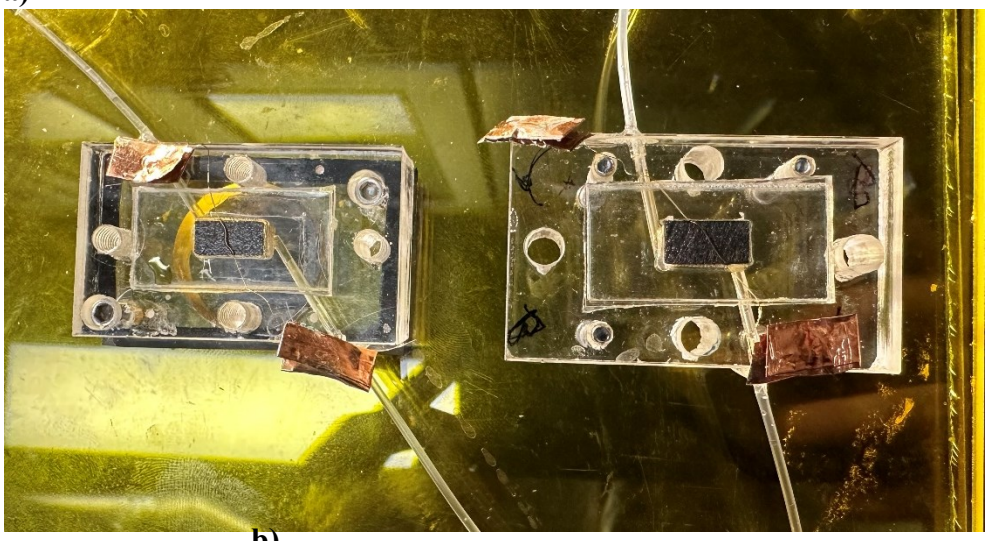

b)

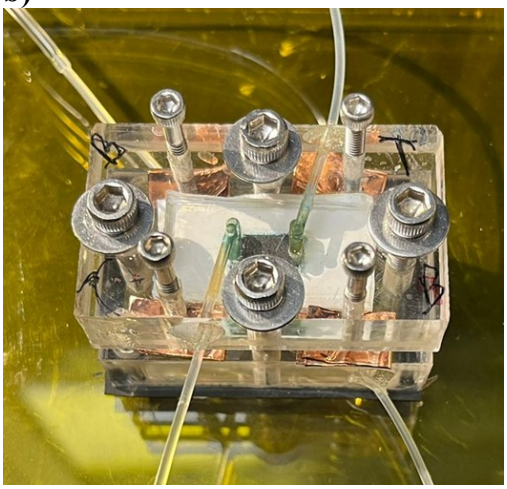

873

874

875 ***Figure S27*** *a) Positive and negative half-cells composed of acrylic end plates, PDMS, carbon*
876 *electrodes, and gold wires serving as current collectors. b) Complete cell.*

877

878

879 ***Figure S28*** *Experimental Setup for In Situ Fluorescence Microscopy Investigation of*
880 *Electrochemical Carbon Capture Flow Cells.*

881

882